

Sandbar behaviour along a man-made curved coast

Zandbankgedrag langs een aangelegde gekromde kust

(met een samenvatting in het Nederlands)

PROEFSCHRIFT

ter verkrijging van de graad van doctor aan de Universiteit Utrecht
op gezag van de rector magnificus, prof. dr. H.R.B.M. Kummeling,
ingevolge het besluit van het college voor promoties in het openbaar te verdedigen
op vrijdag 6 juli 2018 des middags te 2.30 uur

door

Jantine Rutten

geboren op 21 april 1989 te Delft

Promotor:

Prof. dr. B. G. Ruessink

Copromotor:

Dr. T. D. Price

This work was financially supported by the Dutch Technology Foundation STW, which is part of the Netherlands Organisation for Scientific Research (NWO), and is partly funded by the Ministry of Economic affairs (project number 12686).

Sandbar behaviour along a man-made curved coast

Promotor:

Prof. dr. B. G. Ruessink

Copromotor:

Dr. T. D. Price

Examination committee:

Prof. dr. R.A. Holman

Oregon State University, USA

dr. F. Ribas Prats

Universitat Politècnica de Catalunya, Spain

Prof. dr. ir. S.G.J. Aarninkhof

Delft University of Technology, The Netherlands

Prof. dr. ir. J.A. Roelvink

IHE Delft Institute for Water Education, The Netherlands

Prof. dr. H.E. de Swart

Utrecht University, The Netherlands

ISBN 978-90-6266-507-5

Published by Faculty of Geosciences, Universiteit Utrecht, The Netherlands, in:
Utrecht Studies in Earth Sciences (USES), ISSN 2211-4335

Typeset using X_YL^AT_EX

Printed by: ProefschriftMaken || www.proefschriftmaken.nl.

Cover: Aerial picture of the Sand Engine (The Netherlands) on 13 september 2014, looking in northeasterly direction. Courtesy: Rijkswaterstaat, Joop van der Hout.



Except where otherwise noted, this work is licensed under the Creative Commons Attribution 4.0 International Licence, <http://creativecommons.org/licenses/by/4.0/>, © 2018 by J. Rutten.

Chapters 2 and 3 are last-author versions of previously published articles, © by J. Rutten and co-authors. More information and citation suggestions are provided at the beginning of these chapters.

Utrecht Studies in Earth Sciences 156

Sandbar behaviour along a man-made curved coast

J. Rutten

Utrecht 2018

Faculty of Geosciences, Utrecht University

Contents

Samenvatting	ix
Summary	xi
1 Introduction	1
1.1 Context	1
1.2 Morphological monitoring	5
1.3 Sandbar behaviour	7
1.4 Research objectives and outline	8
2 Accuracy of Nearshore Bathymetry Inverted from X-band Radar and Optical Video Data	11
2.1 Introduction	11
2.2 Study area and data collection	14
2.3 Estimation methods	17
2.4 Results	19
2.5 Discussion	21
2.6 Conclusions	27
3 Observations on sandbar behaviour along a man-made curved coast	29
3.1 Introduction	29
3.2 Methodology	32
3.3 Results	37
3.4 Discussion	46
3.5 Conclusions	49
4 Simulating crescentic sandbar behaviour along a curved coast	51
4.1 Introduction	51
4.2 Methodology	53
4.3 Results	58
4.4 Discussion	67
4.5 Conclusions	68
5 Synthesis	71
5.1 Main findings	71
5.2 Discussion and perspectives	73
Appendix A Accuracy of sandbar and shoreline positions	79
References	83
Dankwoord/Acknowledgements	92
About the author	95
	vii

Samenvatting

Zandbanken zijn ruggen van zand die parallel liggen aan de kustlijn in waterdieptes van ~ 10 m en minder. Ze migreren kustdwars door de surfzone met tijdsvariërende golfcondities. Tegelijkertijd ontwikkelen ze intrigerende kustlangsvariërende patronen. Crescentische zandbanken, gekarakteriseerd door landwaartse en zeewaartse uitstulpingen met kustlangse golflengtes van $O(100)$ m en kustdwarse amplitudes van $O(10)$ m, ontstaan tijdens laag tot gematigd energetische golven die recht op de kust invallen. Ze verdwijnen tijdens energetische golven of sterk schuin-invallende golven. Dit algemene begrip van het ontwikkelings – verdwijnings mechanisme berust grotendeels op data- en modelstudies langs rechte kusten. Echter, een gekromde kust kan duidelijk de zandbankdynamiek beïnvloeden, omdat deze zorgt voor een kustlangse variatie in de lokale golfhoek en -hoogte. Verder inzicht in de effecten van een gekromde kust op de kustnabije morfodynamiek is uiterst relevant, omdat een substantieel gedeelte van de kustlijn (op wereldschaal) bestaat uit gekromde kusten (baaien, zandgolven in de kustlijn). Ook wordt verwacht dat hun aantal toeneemt met de stijgende trend om geconcentreerde, km-schaal suppleties aan te leggen als duurzame kustbeschermingsmaatregel.

Het overkoepelende doel van dit proefschrift is het creëren van een ruimer begrip over zandbankgedrag langs de gekromde kust van de dynamische, km-schaal Zandmotorsuppletie in Nederland, op tijdschalen van dagen tot seizoenen. Deze 21 Mm³ suppletie is een kustlijn-perturbatie die initieel (2011) 1 km de zee in stak en zich langs de kust over 2.4 km uitstrekte. Het is de insteek dat de Zandmotor zich langs de kust gaat uitspreiden onder invloed van golven en stromingen gedurende ongeveer 20 jaar. Om zandbankgedrag te onderzoeken zijn data essentieel. Hun inwinning is echter hoogst uitdagend in een dynamisch, km-schaal studiegebied. Kustgestationeerde remote sensing platformen, zoals X-band radar en optische video, zijn hiervoor bruikbaar. Deze verstrekken beelddata met een grote ruimtelijke dekking, een dichte ruimtelijke en temporele resolutie, voor een lange termijn en tegen relatief lage kosten. Hun beelddata van het zeeoppervlak geeft informatie over de morfologie onder water, zoals bodemhoogte en zandbankpositie. In dit proefschrift zijn de nauwkeurigheden bepaald van bodemhoogte en zandbankpositie, waarna zandbankgedrag, inclusief de onderliggende mechanismes, is onderzocht met behulp van een 2.4-jaar lange beelddataset en een numeriek morfodynamisch model.

Bodemhoogtes werden geïnverteerd uit X-band radar data en optische video data met ieder hun eigen inversie-algoritme, welke verschillen in de methode die het golfgetal en de golffrequentie herleidt (Hoofdstuk 2). Radarafgeleide bodemhoogtes volgden uit een methode die beruiste op Fouriertransformaties (FFT), z_{radarFFT} , terwijl videoafgeleide bodemhoogtes volgden uit een cross-spectrale (CS) methode, z_{videoCS} . Validatie met *in situ* metingen laten zien dat zowel z_{radarFFT} als z_{videoCS} een systematische bias hebben, behalve op tussenliggende dieptes. Op grote diepte, zijn z_{radarFFT} en z_{videoCS} beiden te ondiep, respectievelijk 1.0 m (voor $-15 \text{ m} \leq z_b \leq -9 \text{ m}$) en 0.59 m (voor $-10 \text{ m} \leq z_b \leq -5 \text{ m}$). Op kleine diepte zijn z_{radarFFT} en z_{videoCS} beiden te diep (respectievelijk 2.3 m voor $z_b \geq -6 \text{ m}$ en 0.92 m voor $z_b \geq -1 \text{ m}$). De grote bias in z_{radarFFT} op kleine diepte kan gerelateerd

zijn aan een inhomogeen golfveld in de 960 x 960 m analysetegels. Op kleine diepte, waar morfologische schalen kleiner worden en dus de homogeniteit van het golfveld afneemt, bestaat mogelijk voorkeur voor een CS-methode aangezien hiervan de analysetegels gewoonlijk kleiner zijn. Zandbankposities volgden uit brekerlijnen in tijdsgemiddelde beelden met een nauwkeurigheid van $O(10\text{ m})$, consistent met eerdere studies. Berustende op deze nauwkeurigheidsbepalingen ga ik in Hoofdstuk 3 verder met uit beeldafgeleide zandbankposities, omdat ik beeldafgeleide bodemhoogtes nog niet voldoende nauwkeurig acht om zandbankgedrag te bestuderen op tijdschalen van dagen tot seizoenen.

Zandbank- en kustlijnposities werden bepaald uit een 2.4-jaar lange dataset (2013-2015) van dagelijkse laagwater videobeelden, waarna hun kustdwarse posities en de mate van patroonvorming werden berekend in een gebied ten noorden en ten westen van de kop van de Zandmotor (Hoofdstuk 3). Zowel aan de noord- als westzijde worden kustdwarse bankposities gedomineerd door een seizoenssignaal met zeewaartse migratie in de winter en landwaartse migratie in de zomer. De bankgeometrie als ook het moment van patroonvorming en -verdwijning verschillen tussen beide zijden. De bank aan de noordzijde ligt relatief dicht bij het strand op kleine diepte en heeft patronen met kleine kustlangse golflengtes in vergelijking tot de bank aan de westzijde. Patronen ontstaan in de lente- en zomermaanden aan de noordzijde, tijdens langdurige perioden van nagenoeg rechtinvalende, gematigd energetische golven. In de herfst- en wintermaanden brengt een reeks van stormen met tijdsvariërende invalshoek de patroonvorming op gang aan de westzijde, terwijl deze condities patronen aan de noordzijde doen verdwijnen. Kustlangse verschillen in bankgeometrie en het moment van patroonvorming lijken verband te houden met de lokale brekingshoogte en lokale golfhoek.

Hoe een gekromde kust bijdraagt aan de kustlangse variabiliteit in crescentische patroonvorming werd systematisch onderzocht met een morfodynamisch model (Hoofdstuk 4). De bathymetrische opzet en de tijdsvariërende golfforcering zijn losjes gebaseerd op observaties van de Zandmotor. De simulaties laten zien dat de kustlangse positie en de groeisnelheid van crescentische patronen variëren met de lokale golfhoek, die afhangt van de diepwater golfhoek en de lokale oriëntatie van de kustlijn. Met een toenemende hoek van inval van de golven intensiveren de kustlangse stromingen en verlagen de golfhoogtes op de banktop, als gevolg van een toenemende refractie op de gekromde dieptecontouren. Zodoende nemen de groeisnelheden van de patronen af. Variaties op de kromming van de kustlijn tonen dat patronen sneller ontwikkelen langs een sterk gekromde kust, gegeven een beperkte hoek van inval binnen het golfklimaat. Dit impliceert dat muistromen, welke geassocieerd worden met sterk crescentische banken en bekend staan om hun dodelijk bedreiging voor badgasten, mogelijk toenemen in aantal en sterkte langs kusten die sterk gekromd zijn (bijvoorbeeld ten gevolge van de aanleg van een geconcentreerde, km-schaal suppletie).

Summary

Sandbars are submerged ridges of sand parallel to the shoreline in water depths less than ~ 10 m. They migrate across the surf zone in response to time-varying wave conditions, and simultaneously develop intriguing alongshore variable patterns. Crescentic sandbars, characterised by landward and seaward protrusions with alongshore wavelengths of $O(100)$ m and cross-shore amplitudes of $O(10)$ m, arise under low to moderately energetic waves that approach near-normal and are destructed under energetic waves or strongly oblique waves. This general understanding on the formation-destruction mechanism is largely based on data and modelling studies for straight coastlines. A curved coastline, however, may profoundly affect sandbar dynamics, as it imposes an alongshore variation in the local incidence angle and wave height. Better insight in the effects of a curved coastline on nearshore morphodynamics is highly relevant, because curved coasts (embayed beaches, shoreline sand waves) are bordering a substantial part of the world's coastline, and their number is expected to grow with the increasing trend to construct concentrated, km-scale nourishments as sustainable coastal protection measures.

The overall aim of this thesis is to improve the understanding of sandbar behaviour along the curved coast of the dynamic, km-scale Sand Engine nourishment in The Netherlands at daily to seasonal timescales. This 21 Mm^3 nourishment is a coastline perturbation that initially (2011) protruded 1 km into the sea and extended 2.4 km alongshore. It is intended to slowly diffuse via waves and currents that transport the nourished sand to the adjacent coasts within its expected lifetime of 20 years. To investigate sandbar behaviour, data are essential but their collection is highly challenging at such a dynamic, km-scale field site. Shore-based remote sensing platforms, such as X-band radar and optical video, are suitable since they provide image data with typically large spatial coverage, at high spatial and temporal resolutions for the long-term, against relatively low cost. Their image data of the sea surface give information on the underlying morphology, such as bed elevation and sandbar position. In this thesis, accuracies of bed elevation and sandbar position have been determined, whereafter sandbar behaviour including its underlying mechanisms have been investigated with a 2.4-year image data set and a numerical morphodynamic model.

Bed elevations were inverted from X-band radar data and optical video data with their own inversion algorithm, differing in the method of $\Omega - k$ (wave frequency-wave number) retrieval (Chapter 2). Radar-derived bed elevations followed from a method based on Fast Fourier Transforms (FFT), z_{radarFFT} , whereas video-derived bed elevations followed from a cross-spectral (CS) method, z_{videoCS} . Validation with *in situ* measurements reveal that both z_{radarFFT} and z_{videoCS} have a systematic bias, except for intermediate depths. At large depths, z_{radarFFT} and z_{videoCS} are both too shallow, by 1.0 m (for $-15 \text{ m} \leq z_b \leq -9 \text{ m}$) and by 0.59 m (for $-10 \text{ m} \leq z_b \leq -5 \text{ m}$), respectively. At shallow depths, z_{radarFFT} and z_{videoCS} are too deep (2.3 m for $z_b \geq -6 \text{ m}$ versus 0.92 m for $z_b \geq -1 \text{ m}$, respectively). The large bias in z_{radarFFT} at shallow depth may relate to an inhomogeneous wave field in the 960×960 m analysis windows. At shallow depths, where morphological scales become finer and thus homogeneity of the wave field decreases, a CS-method may be preferred instead, because its analysis tiles are

usually smaller. Sandbar positions followed from breaker lines in time-averaged images with an accuracy of $O(10\text{ m})$, consistent with earlier studies. Based on these accuracy assessments, I continue in Chapter 3 with imaged-derived sandbar positions, as I consider image-derived bed elevations not yet sufficiently accurate to study sandbar behaviour at daily to seasonal timescales.

Sandbar and shoreline positions were extracted from a 2.4-year data set (2013-2015) of daily low-tide video images, whereafter their cross-shore positions and degree of patterning were computed within a box north and west of the Sand Engine's tip (Chapter 3). At both the northern and western side, cross-shore bar positions are dominated by a seasonal signal with offshore migration in winter and onshore migration in summer. The bar geometry as well as the timing of pattern formation and destruction differ between both sides. The bar at the northern side is relatively closely located to the beach, at small depth and with small alongshore wavelengths of the patterns, compared to the bar at the western side. Patterns form in the spring and summer months at the northern side under prolonged periods of near-normal, moderately energetic waves. In the autumn and winter months, a series of storms with time-varying wave angle trigger the formation of patterns at the western side, while these conditions destruct patterns at the northern side. Alongshore differences in bar geometry and timing of pattern formation are suggested to relate to the local breaker height and local wave angle, respectively.

How a curved coast contributes to alongshore variability in crescentic pattern formation was systematically explored with a morphodynamic model (Chapter 4). The bathymetric setup and the time-varying wave forcing was loosely based on observations at the Sand Engine. Simulations show that the alongshore positioning and growth rate of crescentic patterns vary with the local angle, which depends on the offshore wave angle and the local coastline orientation. With increasing wave obliquity, alongshore currents intensify and wave heights at the bar crest reduce due to increasing refraction on the curved depth contours. Consequently, pattern growth rates decrease. Variations on the coastline curvature reveal that patterns develop faster along a strongly curved coast, given that the wave climate is low oblique. This implies that rip currents, associated with pronounced crescents and known as a deadly hazard to swimmers, may increase in number and strength at coasts that are strongly curved (for example due to implementation of a concentrated, km-scale nourishment).

Chapter 1

Introduction

1.1 Context

Worldwide, 40% of the coastline is bordered by beaches consisting of sand and/or gravel (Bird, 2000) with dunes or cliffs on their landward side. These beaches accrete when the supply of sediment is larger than its demand, whereas they erode when the sediment supply is smaller than the demand. Erosion may be episodic (days) or take place over longer periods (years-decades). When erosion is not balanced by accretion on the long term, the coastline retreats and the dunes lose their strength to safeguard the hinterland from flooding. Doody et al. (2004) report that a fifth of the beaches in the European Union would erode without taking protection measures. As a result, low-lying hinterland, often densely populated and holding high socioeconomic, cultural and ecologic values, becomes increasingly prone to marine flooding. To illustrate, 70 million inhabitants of the European Union live in flood-prone coastal regions (Doody et al., 2004). In The Netherlands, even more than half of its population (9 million) lives below sealevel, and about 65% of its gross national product is produced in the coastal region (Kabat et al., 2009). These numbers clearly indicate that keeping the coastal defence line effective is of utmost importance.

The underlying causes of erosion are diverse. Severe storms undercut the dunes or create surged water levels that initiate dune overwash, inundation or breaching, all leading to dune erosion (e.g. Sallenger, 2000; Morton and Sallenger, 2003; Thornton et al., 2007; Roelvink et al., 2009). Also, gradients in the alongshore transport may result in a local loss of sediment (e.g. Stewart and Davidson-Arnott, 1988; Aagaard et al., 2004; Silva et al., 2016). Furthermore, man-made structures created to safely navigate into harbours (jetties), to guarantee coastal safety (e.g. groins, seawalls, breakwaters), or to regulate river discharges (e.g. dams, sluices) may interrupt or change natural pathways of sediment transport and locally reduce sediment supply and thus cause erosion (e.g. Pope, 1997; Hsu et al., 2007; Van Rijn, 2011). In addition, climatic change (both natural and human-induced) may lead to coastal erosion due to global sealevel rise, and possible changes in the averaged wave conditions and in the intensity, frequency and duration of storms (e.g. Wong et al., 2014; Ranasinghe, 2016; Bakker et al., 2016). Under an increased sealevel, wave impact on the beach and dune foot will increase if the coastal profile does not accrete vertically (e.g. De Winter and Ruessink, 2017), especially if increased storminess forces waves to attack higher on the coastal profile.

1.1.1 Hard, soft and nature-based coastal protection

To guarantee coastal safety, persistent coastal erosion has traditionally been combatted by locally building hard structures of rocks, concrete or timber. These structures aim to reduce wave impact on the beach and dunes (shore-parallel breakwaters), capture sediment to stabilise or widen the beach (shore-perpendicular groins), or serve as an artificial coastal

defence when dunes are absent (seawalls) (Van Rijn, 2011). The negative side effects associated with such hard structures, e.g. erosion at nearby beaches, led to a shift towards applying 'soft' solutions to combat coastal erosion. These include nourishments, large (1-2 Mm³) volumes of sand, dredged from offshore areas and placed on the beach or in the nearshore zone (Hamm et al., 2002; Figure 1.1). The nourished sediment is transported by wind, waves and currents across the beach and nearshore zone over several years, strengthening the coastal system (e.g. Van der Grinten and Ruessink, 2012; Vermaas et al., 2017). Nourishments placed on the beach are well-perceived at sites with narrow beaches and low or no dunes, where coastal safety is directly at stake or where recreation is important (e.g. Mediterranean coast, Jimenez et al., 2011). However, their substantial initial losses and limited lifetimes of only 1-2 years at the more exposed beaches (Van Rijn, 2011) have been experienced as increasingly negative. In addition, their construction phase, requiring calm weather, may interfere with the recreational season. Nourishments placed at the shoreface, in 5-6 m depth, are considered as the cost-effective alternative at sites where dunes are relatively high and flooding of the hinterland is thus not a direct threat (Van Rijn, 2011). Such nourishments increase or maintain the sand volume across the beach profile by functioning as feeder that provides the onshore shallow waters with sand through transport related to wave asymmetry and horizontal flow patterns (Van Duin et al., 2004; Grunnet and Ruessink, 2005). Besides, they function as natural breakwaters, reducing wave impact at the beach by triggering wave breaking and consequent dissipation of energy on their crest. Lifetimes of both beach and shoreface nourishments are limited up to a few years. Therefore, regular repetition is required to keep up coastal safety levels, but is potentially disadvantageous for the ecologic and recreational value of the nourished site (Temmerman et al., 2013).

Nowadays, site-specific and sustainable protection measures are increasingly demanded that fulfil also environmental and societal needs. Hereto the Building with Nature (BwN) programme was launched in 2008 that aims to improve water safety by use of natural processes, following an interdisciplinary approach (De Vriend and Van Koningsveld, 2012; www.ecoshape.org). Besides sandy shores, the BwN programme also focuses on estuaries, tropical coastal seas, shelf seas and delta lakes. One of the pilot projects of a nature-based and sustainable coastal protection is the km-scale nourishment at the erosive Delfland coast in The Netherlands, known as the Sand Engine (Figures 1.1 and 1.2; Stive et al., 2013). The Sand Engine nourishment, with 21 Mm³ substantially bigger than regular nourishments, is intended to continuously supply the nearby coastline with sand over several kilometers for a 20-year period using the natural forces of waves, tides and wind. The Sand Engine's size and shape are expected to create a more efficient and economic coastal protection than regular protection measures. Simultaneously, environmental impact is expected to be less, because human intervention is concentrated in time and space.

1.1.2 The Sand Engine

The Sand Engine was constructed in 2011 as a hook-shaped peninsula, featuring a lagoon and a small lake, and extending 2.4 km alongshore and protruding 1 km into the sea having a maximum elevation of 7.3 m (Figure 1.3a). The morphology and current patterns changed abruptly after implementation of the mega-nourishment (De Schipper et al., 2016; Radermacher et al., 2017). Flora and fauna (e.g. fish, benthos, dune grasses), as well as recreation (e.g. beach visitors, beach restaurants) are intended to be positively affected now and in the upcoming years. The hook shape of the Sand Engine creates a variety of environments compared to the rest of the wave-dominated North Sea coast, e.g. lagoon sheltered from high waves, and thereby increases potential for new nature (flora and fauna) and recreation. Main

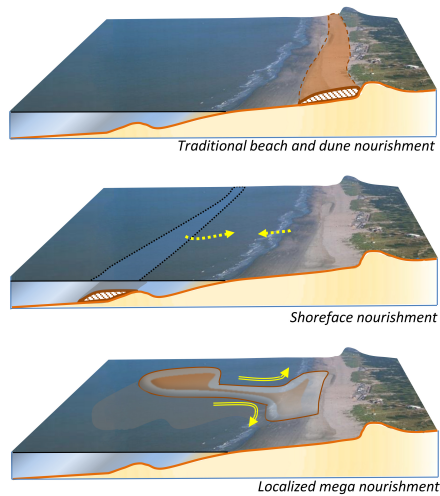


Figure 1.1: Schematic representation of soft coastal protection strategies, including a (top) beach and dune nourishment, (middle) shoreface nourishment, and (bottom) concentrated km-scale nourishment. The yellow arrows in the middle and bottom panel indicate the cross-shore and alongshore spread of the nourishments in time through wave, tide and wind forcing, resulting in a strengthening of the coastal defence (Adapted from Stive et al. (2013), reproduced with permission from the Coastal Education and Research Foundation, Inc.

findings from the evaluation of the Sand Engine's initial five years of development (Brière et al., 2017; Taal et al., 2016) indicate that new flora and fauna is limited so far, whereas recreation has seen an increase in the variety of visitors (e.g. kite and wind surfers). The observed slow rates of dune formation, and dispersal of vegetation, fish and benthos may be inherent to nature development, and therefore conclusive statements cannot yet be drawn. Because the morphology forms the boundary condition for flora, fauna as well as recreation, understanding the morphological behaviour of the Sand Engine in further detail is key to predicting the Sand Engine's short-term (days) to long-term (decades) impacts.

The long-term evolution of the Sand Engine has been predicted by morphodynamic models as a gradual alongshore diffusion of the nourishment over a >20 -year period (Stive et al., 2013; Arriaga et al., 2017). This diffusion implies a gradual, but persistent, erosion at the tip of the Sand Engine, and a deposition of the eroded sand at the adjacent beaches. This feeding behaviour can be observed in aerial pictures of the development during the first years (Figure 1.3). From monthly bathymetric measurements, De Schipper et al. (2016) showed that the shoreline retreated in the first 1.5 years after construction, locally up to 300 m, while the alongshore extent of the Sand Engine increased. In addition, the cross-shore profile was observed to rapidly adjust from a man-made, convex profile with a relatively steep slope to a concave profile with a milder slope and a small subtidal sandbar of ~ 1 m amplitude.

Sandbars are elongated ridges of sand, roughly parallel to the shoreline, which are commonly found in the subtidal and intertidal zones of sandy beaches (King and Williams, 1949; Wright and Short, 1984). Sandbars have been thoroughly studied, as they are one of the most dynamic features in the nearshore zone on daily to inter-annual timescales, continu-

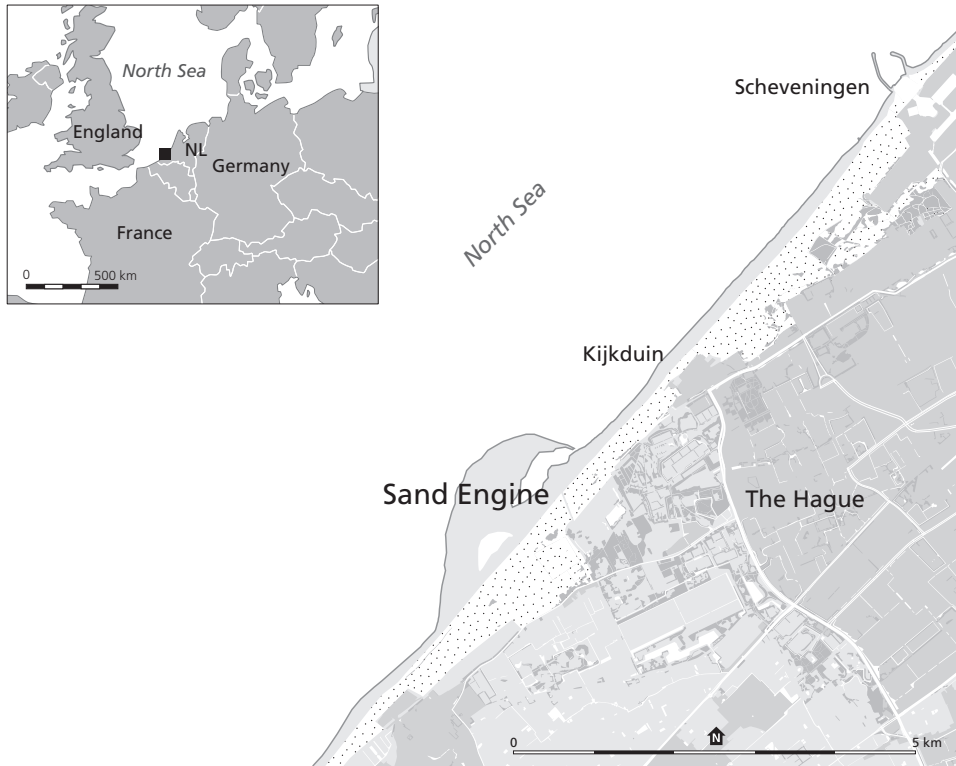


Figure 1.2: Location of the Sand Engine, The Netherlands.

ously migrating across the surf zone and developing intriguing patterns (Sonu, 1973; Wright and Short, 1984; Sallenger et al., 1985; Plant et al., 1999; Van Enckevort et al., 2004; Coco and Murray, 2007). Sandbars function as coastal protection by dissipating wave energy, as waves break on top of them, and thus reduce wave impact at the dunes. If bar geometries become complex, currents may develop that are potentially dangerous to swimmers (Lushine, 1991; Short and Hogan, 1994). Therefore, insight in bar behaviour is crucial. Although bar dynamics and their drivers are nowadays rather well understood, studies mainly examined straight coasts. How bar behaviour is different along a curved coast, such as the Sand Engine, is largely unknown. Given the expected increase in the upcoming years of km-scale nourishments that alter coastline orientation, better understanding is needed on these meso-scale $O(100\text{ m})$ morphodynamics at large-scale coastline perturbations. This thesis addresses the challenges (1) how such a vast and dynamic region can be monitored best and (2) how such a region, including its sandbars, evolves spatially and temporally. Below, these challenges are explained in further detail in Sections 1.2 and 1.3, respectively, whereafter Section 1.4 introduces the research questions and gives an outline of the thesis.



Figure 1.3: Aerial pictures (from the north) of the Sand Engine, The Netherlands, showing its morphological evolution. Pictures were taken in (a) July 2011 (shortly after construction), (b) October 2011, (c) January 2012, (d) October 2012, (e) October 2013, (f) September 2014, (g) May 2015, (h) August 2016, and (i) July 2017. Courtesy: Rijkswaterstaat, Joop van der Hout.

1.2 Morphological monitoring

Studying coastal morphodynamics at dynamic, km-scale field sites, such as the Sand Engine, challenges data collection. Hereto, data sets are needed of long duration with small sampling interval. Traditional techniques, e.g. sonar-equipped jet-skis (MacMahan, 2001; Ruggiero et al., 2005), provide highly accurate measurements of the seabed, but are time-consuming, costly, and limited to calm seas. Shore-based platforms equipped with an optical video or X-band radar station (Figure 1.4) provide data on the sea surface, frequently (hours) with large spatial coverage (km^2) and at relatively low cost. Although such remote imaging techniques seem beneficial to the Sand Engine, their application is not trivial. Several processing steps or even algorithms are needed to infer morphological information from the imagery (e.g. Aarninkhof et al., 2003; Pape et al., 2010; Holman and Haller, 2013). For example, the derivation of seabed elevation has been subject of study since World War II to prepare the allies' boat landings (Williams, 1947), and is still ongoing (Holman et al., 2013; Bergsma et al., 2016; Bell et al., 2016). Whether current techniques provide morphological information of sufficient accuracy to study morphological behaviour of large and highly-dynamic field sites is largely unknown.

Time-averaged optical video and X-band radar imagery of the coastal zone (Holman and Stanley, 2007; Holman and Haller, 2013) have been applied widely to study shoreline and sandbar behaviour. Lippmann and Holman (1989) found that the positions of the shoreline and sandbar are approximated in 10-min exposures by white elongated lines that indicate the preferential location of wave breaking (Figure 1.5), with an $O(10 \text{ m})$ accuracy (Van Enck-



Figure 1.4: The (a) X-band radar station near the Sand Engine, The Netherlands (courtesy: www.dezandmotor.nl) and (b) Argus video station at Noordwijk, The Netherlands, two examples of the numerous X-band radar and Argus video monitoring stations over the world.

evort and Ruessink, 2001; Ruessink et al., 2002; Plant et al., 2007; Ribas et al., 2010; Pape et al., 2010). Multi-year image data sets collected at various sites revealed that the position and pattern of breaker lines changed with time, and thereby contributed to, for example, the understanding of cross-shore migration of sandbars (Plant et al., 2006; Pape et al., 2010), sandbar response to a shoreface nourishment (Ojeda et al., 2008), and the dynamics of the shoreline (Pianca et al., 2015) in perspective of coastal zone management (Kroon et al., 2007). However, acquiring data on actual bed elevation, required in modelling studies and coastal safety assessments, remains challenging.

Bed elevation follows from the water depth, given that tidal elevation is known. Water depth can be derived from image data sets showing the wave pattern (Williams, 1947), as the wave length and period are related to the water depth. Several scientists worked on this technique, known as depth inversion, to improve bed elevation accuracies. Herein, they concentrated on the retrieval of wave characteristics from the image data (Young et al., 1985; Bell, 1999; Stockdon and Holman, 2000; Senet et al., 2008; Plant et al., 2008; Holman et al., 2013) and the theoretical model that relates these wave characteristics to water depth (Grilli, 1998; Holland, 2001; Bell et al., 2004; Catálan and Haller, 2008; Yoo et al., 2011; Tissier et al., 2015). Studies mostly used data from either X-band radar or optical video, and tested their algorithms in the laboratory (Catálan and Haller, 2008), with numerical models (Grilli, 1998) or at various beaches with different environmental and physical boundary conditions (e.g. Bell et al., 2004; Senet et al., 2008; Holman et al., 2013), yielding bed elevations with accuracies that ranged from a root-mean-square error of 0.51 m (Holman et al., 2013) to $O(1)$ m (Bell, 2001). Spatial coverage of bed elevation and, partly, their accuracies depend on the data collection scheme. Typically, X-band radar has a relatively large footprint with a range of a few kilometers compared to the footprint of optical video with a range of ~ 1 km, but its spatial and temporal resolutions are relatively coarse. Consequently, shore-based X-band radar can collect data up to far from the station where the depth is generally large and the morphology homogeneous, whereas optical video can collect data of high resolution near the station where depths are generally shallow and spatial variability of the morphology is high.

Overall, considerable effort in ongoing algorithm-development has resulted in improved bed elevation accuracies. However, no attention has been paid yet to the range of applicability of different algorithms and sensors at a single site, which would reveal when and where they



Figure 1.5: Examples of a 10-min time-averaged image that show two white elongated lines, indicating the outer and inner sandbar. The outer bar patterning varies from (a) straight to (b) crescentic. Images are recorded by the Argus video station at the Gold Coast, Australia, which is part of the world-wide network of Argus stations.

may complement each other. At the Sand Engine, an X-band radar and Argus video station are nearly co-located, providing a relevant data set for such a study.

1.3 Sandbar behaviour

Sandbar behaviour and its underlying drivers have been intensively studied over the last two decades, through analysing field data sets and simulating morphological changes with numerical models. Sandbars have been found to migrate gradually onshore under calm wave conditions and rapidly offshore over $O(10\text{ m})$ under higher energetic conditions (e.g. Thornton and Humiston, 1996; Gallagher et al., 1998). Depending on the wave climate, such cross-shore migration may be storm-driven, or be dominated by a seasonal or inter-annual cyclicity (e.g. Van Enkevort and Ruessink, 2003a; Ruessink et al., 2009; Ojeda et al., 2011). While migrating onshore, sandbars tend to develop an alongshore variability in depth and position (Wright and Short, 1984), with lengthscales of $O(100\text{ m})$ and amplitudes of $O(10\text{ m})$ (Van Enkevort et al., 2004; Figure 1.5b). Wright and Short (1984) related the occurrence of such crescentic patterns to low-energetic conditions. In addition, wave direction was observed to play a role in the formation and decay of crescentic patterns (Thornton et al., 2007; Price and Ruessink, 2011; Contardo and Symonds, 2015). Simulations with numerical morphodynamic models additionally show that patterns tend to arise under small wave angles (e.g. Hino, 1974; Calvete et al., 2005; Drønen and Deigaard, 2007; Splinter et al., 2011) and straighten under large wave angles (Price and Ruessink, 2013; Garnier et al., 2013). Moreover, they revealed the underlying mechanism of positive feedback between the wave-generated flow, sand transport and the bathymetry itself (Falqués et al., 2000; Coco and Murray, 2007).

So far, most studies focused on temporal variability in bar behaviour along straight coasts, and concave curved coasts of embayed beaches. Curved coasts, however, may possess an additionally important spatial variability in nearshore sandbar behaviour, as their variation in coastline orientation imposes an alongshore varying wave forcing (Castelle and Coco, 2012). An important part of the barred beaches have a curved coastline, e.g. embayed beaches, self-organised shoreline sandwaves, cusped deltas but also km-scale nourishments. Along embayed beaches, the direction and rate of shoreline migration has often been observed to

vary at km-scale, known as beach rotation (e.g. Harley et al., 2015). Observations of embayed beaches in Spain (Ojeda et al., 2011) and New Zealand (Van de Lageweg et al., 2013; Blossier et al., 2016) showed that the sandbar rotated too. Also, the occurrence of crescentic patterns was observed to vary at km-scale, at an embayed beach (Short, 1978; Wright and Short, 1984) and at a cusped delta (Backstrom et al., 2008). How crescentic patterning varied in time at these sites was not reported.

Overall, spatiotemporal variability in bar behaviour is expected at convex curved coasts, but has not yet been demonstrated and the underlying mechanisms are not understood so far. The Sand Engine is an excellent site to test whether a man-made convex coast triggers spatial variability in both cross-shore migration and crescentic patterning, and if so, why.

1.4 Research objectives and outline

The main aim of this thesis is to increase the understanding of sandbar behaviour along the curved coast of the dynamic, km-scale Sand Engine nourishment at daily to seasonal timescales. Hereto, three research questions were defined. The first question focuses on monitoring morphology at the dynamic, km-scale Sand Engine site. The second and third questions focus on the actual sandbar behaviour at the same site:

1. *How can morphologic behaviour accurately be monitored in a dynamic, km-scale nearshore setting?*

Since many years, seabed elevation has been estimated from image data, which typically cover a large spatial extent (km) with a small sampling interval (hours). So far, studies mostly focused on algorithm development to improve bed elevation accuracies (e.g. Bell, 1999; Stockdon and Holman, 2000; Senet et al., 2008; Plant et al., 2008; Holman et al., 2013). Herein, different algorithms and sensors were used and tested under various environmental and physical boundary conditions, yielding bed elevations with different accuracies. It remains unclear when and where different approaches can complement each other. Chapter 2 assesses the accuracy of bed elevation derived from data collected at the Sand Engine using two approaches. More specifically, data from (1) X-band radar and (2) Argus video are each processed with an algorithm that is typically used on such data. In addition, a guideline is proposed for the applicability of the two approaches, and volumetric computations are shown of the seabed around the Sand Engine to illustrate whether both approaches can be confidently used in coastal safety studies to determine trends in the sand budget.

Besides, nearshore morphologic behaviour, e.g. sandbar migration, have been widely described with aggregated parameters extracted from X-band radar and optical video data (e.g. Lippmann and Holman, 1989; Ruessink et al., 2002). Earlier studies found that elongated lines of preferential wave breaking approximate the position of sandbars in time-averaged imagery with an $O(10\text{ m})$ accuracy (Van Enckevort and Ruessink, 2001; Ruessink et al., 2002; Plant et al., 2007; Ribas et al., 2010; Pape et al., 2010). Appendix A presents the accuracy of video-derived sandbar position at the Sand Engine. Accordingly, research question 1 is addressed in Chapter 2 and Appendix A.

2. *What is the spatiotemporal variability in sandbar behaviour along the convex curved coast of the Sand Engine at daily to seasonal scales?*

Curved coasts impose alongshore differences in the wave field (Castelle and Coco, 2012),

and thereby potentially provoke an alongshore variability in the nearshore morphodynamics. At concave coasts, a spatial variability in sandbar and shoreline behaviour has been found (Harley et al., 2015; Ojeda et al., 2011; Blossier et al., 2016), but whether similar behaviour is induced by a man-made, convex curved coast is unknown. Chapter 3 quantifies sandbar and shoreline behaviour at both sides of the curved coast of the Sand Engine, using a 2.4-year data set of daily low-tide, time-averaged video images. Subsequently, the observed behaviour is related to local wave characteristics, and hypotheses are formulated on the underlying drivers. Chapter 3 covers research question 2.

3. *What are the underlying mechanisms behind alongshore variability in the formation of crescentic sandbar patterns along a convex curved coast under time-varying wave forcing?*
Crescentic pattern formation has been found to relate to the local wave angle at straight coasts (e.g. Falqués et al., 2000; Calvete et al., 2005; Thiébot et al., 2012; Castelle and Ruessink, 2011; Price and Ruessink, 2011; Garnier et al., 2013; Contardo and Symonds, 2015). Based on the observations at the curved coast of the Sand Engine in Chapter 3, Chapter 4 systematically explores the effect of spatiotemporal variations in local wave angle on alongshore differences in bar behaviour using a non-linear morphodynamic model (Dubarbier et al., 2017). Subsequently, the underlying mechanisms behind pattern formation along a convex curved coast are explained. The effect of a curved coast on pattern formation is further investigated by varying the coastline curvature. Research question 3 is covered in Chapter 4.

The methodology adopted in this thesis is a combination of data analysis from field observations and numerical modelling. The text in Chapter 2, 3 and 4 is based on journal articles and thus partly overlap in terms of the site description. Chapter 5 synthesises the findings of these and provides an outlook to future research.

Chapter 2

Accuracy of Nearshore Bathymetry Inverted from X-band Radar and Optical Video Data

Based on: Rutten, J., S.M. De Jong, and B.G. Ruessink (2017), Accuracy of nearshore bathymetry inverted from X-band radar and optical video data. *IEEE Transactions on Geoscience and Remote Sensing* 55, 2, 1106-1116.

Abstract

Shore-based remote sensing platforms are increasingly used to frequently (\sim daily) obtain bathymetric information of large (\sim km²) nearshore regions over many years. With recorded wave frequency Ω and wave number k (and hence wave phase speed $c = \Omega/k$), bed elevation z_b can be derived using a model that relates Ω and k to water depth. However, the accuracy of z_b as a function of the sensor and the method of Ω - k retrieval is not well known, especially not under low-period waves. Here, we assess the accuracy of z_b , based on two sensors with their own method of phase speed retrieval, in a dynamic, km-scale environment (Sand Engine, The Netherlands). Bias in z_b is systematic. An FFT method on X-band radar imagery produced z_b too shallow by 1.0 m for $-15 \text{ m} \leq z_b \leq -9 \text{ m}$, and too deep by 2.3 m for $z_b \geq -6 \text{ m}$. A cross-spectral method on optical video imagery produced z_b too shallow by 0.59 m for $-10 \text{ m} \leq z_b \leq -5 \text{ m}$, and too deep by 0.92 m for $z_b \geq -1 \text{ m}$. Intermediate depths had negligible bias, -0.02 m for the radar-FFT approach and -0.01 m for the video-CS approach. The collapse of the FFT method in shallow water may be explained by the inhomogeneity of the wave field in the 960 m by 960 m analysis windows. A shoreward limit of the FFT method is proposed that depends on z_b in the analysis windows.

2.1 Introduction

The morphology of the nearshore zone, defined as the region between the shoreline and roughly 10 m water depth, changes on a variety of spatial and temporal scales (Holman, 2001). For example, kilometer-wide shoreline undulations can migrate hundreds of meters in several years, whereas decimeter-scale wave ripples form and move within minutes (Coco and Murray, 2007). The scales involved are site-specific due to environmental boundary conditions such as geology and wave climate. Numerous measurements have been taken to study morphology and its change, for practical applications in coastal zone management, but also purely out of scientific interest in the dynamics of the nearshore zone. Morphological monitoring is becoming increasingly important in perspective of sea level rise, with potentially stronger erosion and higher flooding risks (Wong et al., 2014). Traditionally, *in situ* field data sets are used to study morphology. However, these measurements, gathered with boats (Wijnberg and Terwindt, 1995), jet-skis (MacMahan, 2001; Ruggiero et al., 2005) and amphibious vehicles (Birkemeier and Mason, 1984; Ruessink et al., 2000), are time-consuming

and costly for spatially extensive areas, especially when high spatial and temporal resolutions are required to follow morphological change at the scales of interest. Also, *in situ* surveys are limited to low-energetic conditions, implying that the role of individual high-energetic storms cannot be assessed adequately. Therefore, shore-based remote sensing platforms are increasingly used, allowing large ($\sim\text{km}^2$) nearshore regions to be monitored for a long-term (years) and with short intervals (hourly to daily).

Microwave X-band radar and optical Argus video cameras (Holman and Haller, 2013) are examples of common shore-based platforms in nearshore research. An X-band radar system transmits pulses within the X-band (wavelengths of ~ 3 cm) from an antenna rotating around a vertical axis. A wavy pattern, known as sea clutter, can be recognised in the resulting circular recordings and serves as proxy for the pattern of wind-generated gravity waves. Sea clutter arises by the interaction of the emitted radar pulse with capillary waves on the sea surface and the subsequent accumulation of capillary waves on the wind-wave fronts (for details on the imaging mechanism, see Valenzuela (1978) and Nieto Borge et al. (2004)). X-band radar systems have typically an imaging range of a few kilometers, a temporal resolution of 1 to 3 s, and a spatial resolution of 5 to 10 m. The second example, the Argus video-system, was developed at the Coastal Imaging Laboratory of Oregon State University in the 1990s (Holman and Stanley, 2007). It consists of multiple optical cameras mounted together on top of a high building or tower, looking downwards in different directions along the beach. A host computer stores the collected imagery and sends the data to an archive. In contrast to shore-based X-band sensors, optical sensors are passive, using solar visible radiation, which limits their data availability to day-light conditions. Ocean waves can be recognised in optical imagery from variations in reflection due to the variations in the sea surface slope or from differences in intensity depending on whether waves break or not. Optical systems have typically a smaller range of about 1 km, but a higher sampling frequency $O(1$ Hz) and a denser sampling grid of $O(1$ m) than X-band systems.

Morphological information has been derived from radar and video imagery as morphometric parameters, e.g. sandbar position (Lippmann and Holman, 1989; Ruessink et al., 2002), and as bed elevation (Bell, 1999; Trizna, 2001; Holman et al., 2013). Morphometric parameters are well suited to describe nearshore morphologic behaviour (Ribas and Kroon, 2007; Wijnberg and Holman, 2007; Almar et al., 2010) and have the advantage that they are easy to extract from imagery, although they provide no actual bed elevation. In contrast, the derivation of bed elevation, requiring data-model assimilation (e.g. Bell, 1999; Van Dongeren et al., 2008; Holman et al., 2013), demands considerable computation time in the order of minutes to hours. Yet, estimates of bed elevation are desired by, for example, coastal engineers to evaluate the performance of construction works, by modellers to drive and validate morphodynamic models, and by managers for decision making on coastal safety.

Bed elevation, z_b , follows from water depth h and tidal elevation z_t as $z_b = z_t - h$. Water depth can be inverted from frequency and wave number of wind-generated gravity waves (1-30 s) through a model that relates the three. This technique, explored initially by Williams (1947) and known as depth-inversion, is therefore limited to the nearshore region where the wave frequency and wave number depend on water depth. A simple and widely used model (Bell, 1999; Stockdon and Holman, 2000; Trizna, 2001; Senet et al., 2008) is the linear dispersion relation:

$$\Omega = \sqrt{gk \tanh(kh)} + \vec{k} \cdot \vec{U}. \quad (2.1)$$

Here, Ω is radian frequency, g is gravitational acceleration, $k=|\vec{k}|$ is wave number, h is water depth, $U=|\vec{U}|$ is velocity of the near-surface current, and $c = \Omega/k$ is wave phase speed. The linear dispersion equation assumes that the wave amplitude is a very small fraction of the water depth. Clearly, this assumption is violated in the innermost part of the nearshore. The neglect of amplitude effects in Eq. (2.1) causes c to be underestimated (Tissier et al., 2011) and h to be overestimated (Holland, 2001). Even though several models have been proposed that account for wave non-linearity, e.g. amplitude effects (Grilli, 1998; Bell et al., 2004; Catálan and Haller, 2008; Yoo et al., 2011; Tissier et al., 2011), these are not considered in operational monitoring of large coastal environments because of excessive run times (Holman et al., 2013). For example, Yoo et al. (2011) used a computational-intensive numerical model to obtain information on local wave height and derive z_b with higher accuracy in a single cross-shore profile. In addition, some of the models that account for wave non-linearity are limited to shallow water and therefore require from a certain depth onward a coupling with a model that does function in deeper water (Kirby and Dalrymple, 1986).

Prior to depth-inversion, wave frequency and wave number need to be retrieved, hereafter referred to as Ω - k retrieval. Usually Ω and k follow from an image sequence of the wave pattern recorded with a time interval of seconds. Young et al. (1985) used three-dimensional Fourier Transforms (3D FFT) to derive information about the wave field. Spatial patterns were revealed by performing 3D FFT analysis over spatial subsets (windows) of the imaged area (Trizna, 2001). The spatial and temporal coverage of the window sequences determine the spectral resolutions of the Fourier Transformed image data, and thereby the accuracy of Ω and k (Dugan and Piotrowski, 2003). Specifically, larger coverage results in a finer spectral resolution and thus potentially in a higher accuracy of Ω , k , and h . Window size and sequence length, however, are limited to the spatial and temporal length scales on which the wave field and the morphology is homogenous. For example, Dugan et al. (2001) estimated z_b between -4 m MSL (Mean Sea Level) and -10 m MSL with a root-mean-square error ε_{RMS} up to 1.1 m, using subsets of 256 pixels \times 256 pixels \times 256 images (500 m \times 500 m \times 128 s). In other words, FFT methods seem basically adequate to map large regions of $O(100 \text{ km}^2)$, inherent to X-band radar, with bathymetry homogenous at the scale of the large image subsets $O(1 \text{ km})$. An alternative approach is required as soon as morphological spatial scales become finer, e.g. in tidal inlets and near the shoreline (Trizna, 2001). Senet et al. (2008) developed an algorithm which required analysis windows of only $110 \text{ m} \times 110 \text{ m}$ to estimate z_b , by using a spectral decomposition technique on the 3D image spectra to separate the signal of an inhomogeneous wave field. A few studies refined the spatial resolution of bathymetric maps through estimating wave number and/or phase speed using cross-correlation analysis (time-domain; Bell, 1999) or cross-spectral analysis (frequency-domain; Stockdon and Holman, 2000; Plant et al., 2008) over pixel pairs, techniques that demand image subsets of less spatial coverage, $O(100 \text{ m})$, compared to an FFT method on the same image data set. Stockdon and Holman (2000) estimated z_b up to -5 m MSL, on average too deep by 0.35 m and with an ε_{RMS} of 0.91 m. Most of the bias was found in the breaking zone and during increasing wave heights. Holman et al. (2013) introduced a two-dimensional depth-inversion algorithm, based on the one-dimensional algorithm of Plant et al. (2008) and known by the name cBathy, which computes the cross-spectral matrix and uses the phase ramp of the dominant frequency modes to find the wave number. Tested at Duck, Holman et al. (2013) estimated z_b , on average too shallow by 0.19 m and with an ε_{RMS} of 0.51 m.

To summarise, during the last decade, considerable technique improvement has resulted in higher accuracies of z_b (Bell et al., 2004; Senet et al., 2008; Holman et al., 2013), sometimes at the expense of computational time. Accuracies mentioned in the literature vary from a root-

mean-square error ε_{RMS} of 0.51 m (Holman et al., 2013) to $O(1\text{ m})$ (Bell, 2001), and depend on the imposed algorithm, the model, certain sensor properties and the local environmental and physical boundary conditions. Where, when and how different algorithms or sensors can actually complement each other, highly relevant for data fusion and data assimilation studies (Van Dongeren et al., 2008; Garcia et al., 2013; Wilson et al., 2014), is still poorly studied and documented. Our objective is to assess the accuracy of bed elevation, based on microwave X-band radar and optical Argus video data with their own depth-inversion algorithm based on linear wave theory, in a dynamic, km-scale nearshore setting, with the Dutch Sand Engine site as case study. The two algorithms we use differ in Ω - k retrieval, that is through 3D FFTs (radar) (Young et al., 1985; Dugan et al., 2001; Trizna, 2001), and through cross-spectral analysis (video) (Stockdon and Holman, 2000; Plant et al., 2008; Holman et al., 2013). As explained further in Section 2.3, the FFT method is included in the commercially available radar software package SeaDarQ (see www.seadarq.com or Mosterdijk and Miller (2008)), in combination with X-band imagery, hereafter referred to as radar-FFT approach. The cross-spectral method, known as cBathy (Holman et al., 2013), is here applied to Argus video data, and hereafter referred to as video-CS approach. Both the X-band and video system were positioned at the large ($\sim 3\text{ km}^2$) Sand Engine nourishment in the Netherlands (Stive et al., 2013) as described in Section 2.2. Estimated z_b with the radar-FFT approach and the video-CS approach are compared to *in situ* observations available for a one-year period. This study includes a validation of the video-CS approach at a site exposed to a wind wave climate with short-crested waves (yearly-averaged peak period of 6 s, increasing up to 9 s under storms), extending previous validation at the U.S. ocean-exposed beaches dominated by long-period swells (Holman et al., 2013). Section 2.4 shows the accuracies of z_b derived with the radar-FFT approach and the video-CS approach. Section 2.5 discusses the sources of bias in z_b , introduces a guideline on the applicability of the radar-FFT and video-CS approach to derive z_b in a large and dynamic environment, and presents an application of z_b in the form of volumetric computations. The chapter ends with the main conclusions of our work (Section 2.6).

2.2 Study area and data collection

2.2.1 Study area

The 21.5 Mm³ Sand Engine nourishment is located in front of The Hague in The Netherlands (Figure 2.1). It extended 2.5 km along the beach and protruded 1 km into the sea at the moment of construction in July 2011. The morphology is highly dynamic, both considering the overall shape of the nourishment as well as smaller-scale features such as sandbars. Therefore, with expected change at scales of interest from meters to kilometers and from days to years, the site is especially suitable to be monitored by remote sensing platforms. An account of its evolution after implementation is provided in De Schipper et al. (2016). In brief, the tip of the Sand Engine eroded by 240 m in three years and sand was transported in the northeastern and southwestern direction along the coast. Additionally, sand accumulated in a pronounced 1 to 1.5 m high subtidal sandbar. The bar crest was located at about -1.5 m MSL at the tip and at -2.5 m MSL at the southern side of the Sand Engine. Occasionally, sandbars were also found in the intertidal zone (-1 m to 1 m +MSL).

The Sand Engine is exposed to a wind-wave climate with an annual mean significant wave height H_s of 1.3 m and a peak wave period T_p of 6 s (Wijnberg, 2002). The tide is semi-diurnal with Mean Low Water at -0.4 m MSL and Mean High Water at 1 m MSL , and generates an alongshore current with velocities up to 0.5 m/s (Wijnberg, 2002). Tidal water levels at the

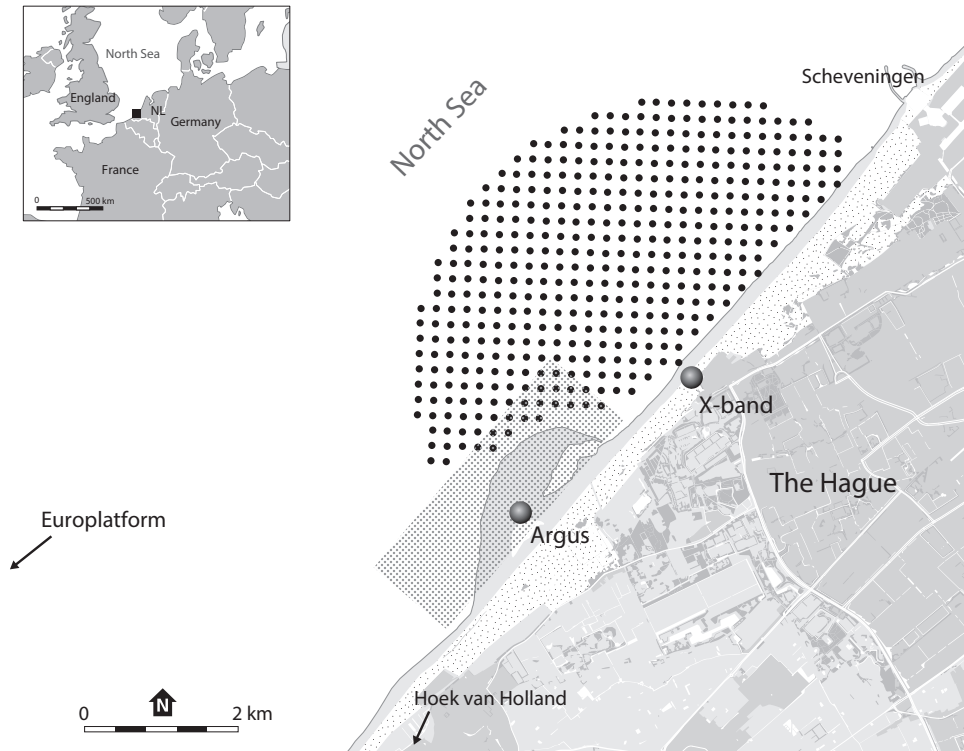


Figure 2.1: Location of the study site with the X-band radar sampling region (black dots), the Argus video sampling region (grey dots), the tidal stations at Hoek van Holland and Scheveningen, and the wave buoy of the Europlatform.

Sand Engine, required to convert water depth to z_b , are available as a weighted average of data collected by measuring stations south (Hoek van Holland) and north (Scheveningen) of the Sand Engine (Figure 2.1). Wave characteristics, needed to weigh estimated z_b in a running average filter (see Section 2.3), are available as observations from the Europlatform wave buoy (Figure 2.1).

A one-year data set (March 2013 to March 2014) was considered for analysis, collected by an X-band radar and an Argus video platform. For reasons beyond our control, the two available platforms were not co-located (Figure 2.1); to some degree, this will hamper the comparison of z_b derived with the radar-FFT and video-CS approach.

2.2.2 X-band radar

A low-grazing X-band radar system was located north of the Sand Engine ($N 52.0669^\circ E 4.2169^\circ$) in the dunes at 12.9 m +MSL, with the antenna at 17.45 m +MSL (Figure 2.1). The antenna rotated in ~ 2.85 s around a vertical axis, while sending pulses of 50 ns with a wavelength of 3.2 cm in VV polarisation. The temporal resolution of the image is constrained to the rotation time (Table 2.1), whereas range resolution and azimuth resolution are determined by pulse length, beam width and range. No tuning of the sampling scheme or algorithm was possible, since the large data files needed to be processed on-site. Instantaneous images

Table 2.1: Spatial and temporal resolution of the used video and radar systems with respect to depth-inversion.

Technique	Δt	t	Analysis window	Δx	Δy
Argus video	2 Hz	1024 s	40 m x 80 m to 80 m x 160 m	10 m	20 m
X-band radar	0.35 Hz	180 s	960 m x 960 m	200 m	200 m

have been collected 24 hours a day with a maximum range of 3800 m and a range resolution of 7.5 m. The azimuth resolution increased linearly from 3 m at 500 m distance from the radar station up to ~ 20 m at 3800 m distance.

2.2.3 Argus video

The Argus station was located in the centre of the Sand Engine (N 52.05083° E 4.18447°), at the highest point (7.3 m +MSL) (Figure 2.1). Eight 5.0 Mega Pixel cameras, mounted on the top of a tower, 42.7 m above MSL, covered 245 degrees of the horizontal plane. Pixel time series have been collected since June 2013, whereas the acquisition started in March 2013 for the ten-minute time-exposure (timex) images. Every four hours during daylight, a grid of pixels was sampled at 2 Hz for a 17 min duration, which covered 3000 m alongshore and 800 m cross-shore with an alongshore and cross-shore resolution of 20 m and 3 m, respectively (Figure 2.1; Table 2.1). Pixels without any wave motion should not be included in the depth-inversion, therefore we excluded all pixels shoreward of the low-tide breaker line of the closest time instant. Breaker lines were found by automated alongshore tracking of the image intensity maximum (Pape et al., 2010). Then, the grid of pixels was projected on a local coordinate system with the origin at the Argus station, a positive x -axis pointing offshore and a positive y -axis pointing to the southwest (220°) along the beach (Figure 2.2). The coordinate transformation from image coordinates into local coordinates by means of standard photogrammetric equations needs information on camera position, camera orientation (tilt, pitch and roll) and focal length. Distant temporary Ground Control Points (GCPs), clearly visible in the image and known in the local coordinate system, were used to accurately derive the camera orientation. Minute changes in camera orientation cause a substantial shift in image coordinates. Therefore, a new image geometry needs to be determined regularly, bearing in mind camera shifting due to strong winds or thermal expansion. Unfortunately, no permanent GCPs were available for cameras that looked seaward and geometries could not be updated. Focal length and field of view were determined for each camera in the laboratory, where each camera was also calibrated for radial lens distortion. With known image geometry and focal length, image coordinates were transformed into local coordinates via two inverted photogrammetric equations (Holland et al., 1997), assuming that the vertical coordinate is constant at the tidal level. An extended overview of the Argus system and image processing can be found in Holman and Stanley (2007).

2.2.4 In situ measurements

In situ bed elevation, $z_{in\ situ}$, are available between -15 m and $+1$ m MSL from surveys by quad, jet-ski and ship. Every two months, the intertidal topography ($-1\text{ m} < z_b < 1\text{ m}$) was measured by quad with an estimated vertical accuracy of 0.05 m and a horizontal accuracy of 0.02 m. At the same time, the subtidal bathymetry ($-10\text{ m} < z_b < 0\text{ m}$) was measured by jet-ski equipped with a single beam echo-sounder and a Leica GPS receiver in RTK-mode. Water depth followed from the return time of the emitted sound wave reflecting on the sea floor and the speed of sound within the water column. The latter was corrected for water temperature and salinity measured with a Conductivity-Temperature-Depth sensor. Surveys were carried

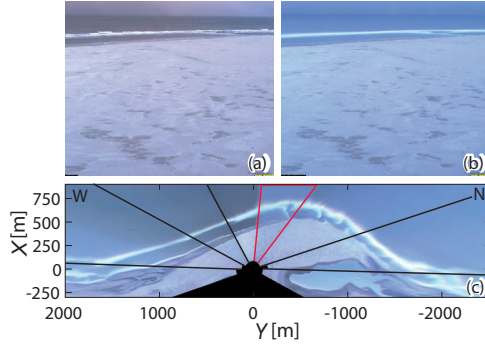


Figure 2.2: Example of (a) a snap shot, (b) a time-exposure and (c) a merged plan view time-exposure image of the Sand Engine Argus video station. The camera seams are indicated by the black lines. The red delineated part corresponds to the time-exposure image shown in (b). The image was projected on a local coordinate system, with the origin at the Argus station, a positive y -axis pointing to the southwest along the beach and a positive x -axis pointing offshore.

out during calm seas ($H_s < 1.65$ m) to reduce errors in water depth due to wave-induced pitch and roll of the jet-ski (Van Son et al., 2010). Vertical and horizontal accuracies are estimated at 0.1 m and 0.5 m, respectively. Quad and jet-ski measurements were collected along cross-shore transects with a cross-shore resolution of ~ 3 m and an alongshore resolution of ~ 40 m. Seaward of the -7.5 m contour, cross-shore transects were separated by 80 m. Beyond the -10 m contour z_b was measured by ship with a single beam echo-sounder along transects separated by 125 to 250 m and a spacing of 3 to 5 m. For -12 m $< z_b < -10$ m, data are available on a grid with a 10 m spacing every year, whereas beyond the -12 m contour data are available on a 20 m grid every three years. The vertical accuracy of the ship measurements is estimated at about 0.25 m (Wijnberg and Terwindt, 1995).

All $z_{in situ}$ were translated and rotated from the national Dutch cartographic system (RD2008) to a local coordinate system and smoothed to a regular 25 m x 2 m grid, covering 5000 m in the alongshore ($y = -3000$ to 2000 m) and 1700 m in the cross-shore ($x = -500$ to 1200 m) direction. The quadratic loess filter (Plant et al., 2002) was used to remove small-scale bathymetric features. Features with length scales of 50 m in the cross-shore and 200 m in the alongshore direction were smoothed by 10%. This smoothing rate increased for smaller features. Smoothing lengths were doubled seaward from the -6 m contour, where survey spacing was about double. Values of $z_{in situ}$ were removed where interpolation errors were above 0.1 m shoreward of -6 m MSL, and above 0.4 m seaward of -6 m MSL. Finally, small gaps were interpolated linearly.

2.3 Estimation methods

2.3.1 Radar-FFT

The X-band radar data were processed with the SeaDarQ software (Mosterdijk and Miller, 2008), including an FFT, some filtering routines, and a non-linear fit with the dispersion relation that iteratively estimated h and \vec{U} . The FFT transformed the wave signals captured in the images to the frequency domain. The large temporal resolution (~ 2.85 s) required a filter to remove aliased frequencies, such aliases are especially present in our wind wave

climate with wave periods below 6 s. In this chapter, we used z_b derived by SeaDarQ with default settings which processes every ~ 15 min a pixel time series of 180 s duration on a grid with 200 m resolution over analysis windows of 960 m by 960 m (Table 2.1). Depth estimates were tide-corrected to z_b , using the weighted average of the measured water level at Scheveningen and Hoek van Holland.

Analysis revealed that z_b was temporally noisy. Therefore, several filter steps were imposed, partially based on Swinkels et al. (2012). Given a time series of z_b at a grid point, a global filter removed estimates exceeding 1.5 standard deviation from the median. Subsequently, a local filter removed each z_b that deviated more than 2 standard deviations from its previous estimate. Then, a 24-hour moving average was applied. Finally, domain-covering bathymetric maps were obtained by filling empty grid points with the most recent 24-hour-averaged z_b . Hereafter, bed elevation derived with the radar-FFT approach is referred to as Z_{radarFFT} .

2.3.2 Video-CS

The Argus video data were processed with the cBathy algorithm (Holman et al., 2013), hereafter explained briefly. Each individual pixel time series was converted to frequency space by a one-dimensional FFT. Then, the cross-spectral matrix was computed over several pre-defined frequency bands, here $f = 0.067$ to 0.25 Hz with $\Delta f = 1/50$ Hz, using data within windows of 80 m by 40 m in the alongshore and cross-shore direction respectively. The analysis was repeated every 20 m in the alongshore and every 10 m in the cross-shore direction. Analysis windows gradually increased towards 160 m by 80 m with distance from the shoreline. After cross-spectral analysis, the wave signature (wave number k , wave angle α) was estimated from the best, weighted non-linear fit of observed and modeled wave phase for the four most coherent frequency bands. Herein, observed wave phase was represented by the dominant eigenvalue of the cross-spectral matrix, whereas modeled wave phase followed from wave frequency and wave number (as phase ramp; Merrifield and Guza, 1990). Subsequently, water depth and the corresponding 95% confidence interval were estimated. Water depth followed from a weighted non-linear fit of the four f - k (frequency – wave number) pairs with the dispersion relation Eq. (2.1), in which currents were neglected.

We used default settings in the cBathy algorithm (Holman et al., 2013), except for certain quality control settings to suppress noise in z_b (minimum dominant eigenvalue of 15, minimum depth of 0.5 m and maximum depth of 10 m). Finally, we used a standard Kalman procedure in the time domain (Kalman, 1960), implemented by Holman et al. (2013) to smooth absent depth estimates and part of the noisy estimates due to sun glare, wave breaking or slowly propagating objects. Thus, a slowly updating bathymetry was created from the individual tide-corrected bathymetric maps, wherein each Kalman depth \bar{h}_{k-1} of the prior time instant $k - 1$ was updated \bar{h}_k as

$$\bar{h}_k = \bar{h}_{k-1} + K(\hat{h}_k - \bar{h}_{k-1}) \quad (2.2)$$

with each new individual depth estimate \hat{h}_k weighted by Kalman gain K . The Kalman gain depended on the individual depth error estimate and a spatially and time-varying process-error, Q , that accounted for natural changes in depth since the prior time instant $k - 1$. Here, Q was Gaussian-shaped, centred around the surveyed yearly-averaged bar crest, and scaled with the root-mean-square wave height H_{RMS}^2 from the Europlatform wave buoy, following Holman et al. (2013) and Van Dongeren et al. (2008). The width of the Gaussian, σ_x of 50 m,

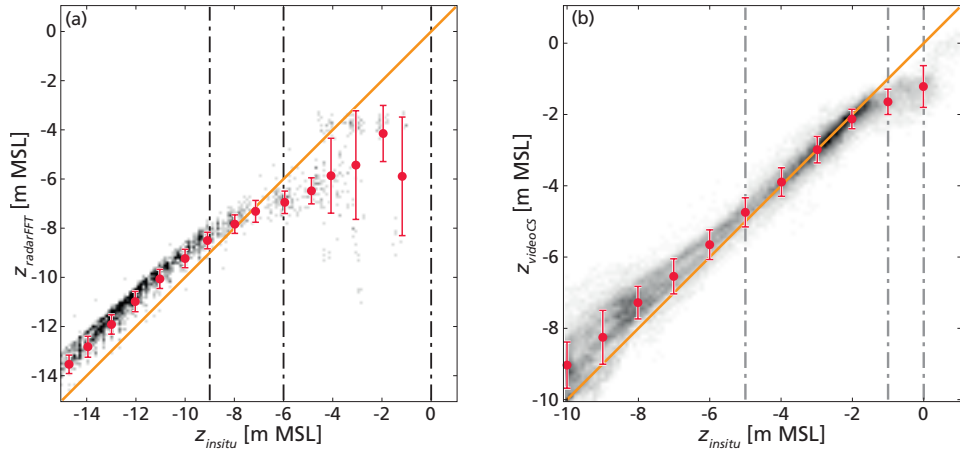


Figure 2.3: Bed elevation (a) derived from X-band radar data with an FFT method, z_{radarFFT} and (b) derived from Argus video data with a cross-spectral method, z_{videoCS} , with the grey level indicating the number of data points. Average z_{radarFFT} and z_{videoCS} over 1 m bins are indicated by the red dots. The error bars indicate \pm the root-mean-square error in the 1 m bins. The vertical dash-dotted lines indicate the ranges in z_b as summarised in Table 2.2.

was determined from the bathymetric surveys wherein substantial change in z_b was observed within 50 m of the yearly-averaged bar crest.

Well seaward of the surf zone, where the imaged wave signal is weak, analysis showed that the Kalman filter was contaminated with obviously incorrect \hat{h}_k of high confidence. Objects that propagate with speeds similar to wave phase speed (e.g. ships and kite surfers) and that have a relatively strong reflection (i.e. high coherence) were found to be the source of error. \bar{h}_k substantially improved when the Kalman filter was seeded initially with a surveyed bathymetry and when updates of \bar{h}_{k-1} were constrained to be different by 2 m at most. Depth estimates were tide-corrected to z_b , using the weighted average of the measured water level at Scheveningen and Hoek van Holland. Hereafter, bed elevation derived with the video-CS approach is referred to as z_{videoCS} .

2.3.3 Validation

Estimates of z_{radarFFT} and z_{videoCS} were compared with *in situ* measurements of bed elevation, $z_{\text{in situ}}$. The latter were interpolated linearly on either the radar or video analysis grid. A domain-wide comparison was performed to reveal potential trends in deviations of z_{radarFFT} and z_{videoCS} . A comparison for each grid point was made to detect spatial patterns in deviations of z_{radarFFT} and z_{videoCS} . Six surveys were used for the comparisons, conducted within the one-year time frame. Maps of z_{radarFFT} and z_{videoCS} with the closest time instant were used, produced within a day of the survey, with one exception produced within seven days.

2.4 Results

Figure 2.3 shows that z_{radarFFT} (a) and z_{videoCS} (b) are similar to $z_{\text{in situ}}$ at intermediate depths, but are systematically too shallow at larger depths and too deep at small depths. The bias, here defined as $z_{\text{estimated}} - z_{\text{in situ}}$, and the ε_{RMS} were accordingly computed over three zones:

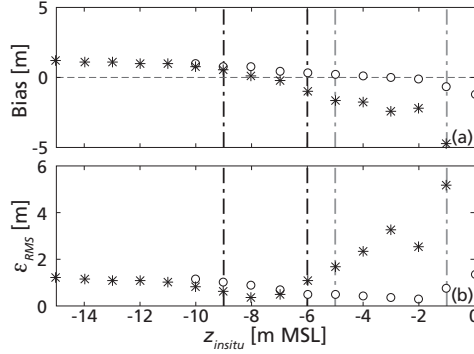


Figure 2.4: (a) Bias and (b) root-mean-square error of radar-derived bed elevation using an FFT method (*) and video-derived bed elevation using a cross-spectral method (o) over 1 m bins. The vertical dash-dotted lines indicate the ranges in z_b as summarised in Table 2.2 for bed elevation derived with the radar-FFT (black) and video-CS approach (grey).

i.e. large depths, intermediate depths, and shallow depths (Table 2.2). At larger depths ($z_{in situ} \leq -9$ m), $z_{radarFFT}$ is too shallow, with an average bias of 1.0 m and an ϵ_{RMS} of 1.0 m. At intermediate depths (-9 m $< z_{in situ} < -6$ m), bias is negligible, -0.02 m, and the ϵ_{RMS} is small, 0.40 m. At shallower depths ($z_{in situ} \geq -6$ m), there is a sharp decrease in the accuracy of $z_{radarFFT}$, being too deep, with a bias of -2.3 m on average and an ϵ_{RMS} of 2.7 m. Figure 2.3(b) shows that $z_{videoCS}$ is slightly too shallow in deeper water ($z_{in situ} \leq -5$ m), with an average bias of 0.59 m and an ϵ_{RMS} of 0.79 m. At intermediate depths (-5 m $< z_{in situ} < -1$ m), $z_{videoCS}$ is accurately estimated, with a bias of only -0.01 m and an ϵ_{RMS} of 0.34 m. At shallower depths ($z_{in situ} \geq -1$ m), $z_{videoCS}$ is too deep, by -0.92 m on average and with an ϵ_{RMS} of 1.0 m. Figure 2.4 shows in more detail how the bias and ϵ_{RMS} vary with $z_{in situ}$. The X-band radar has a larger footprint than the Argus video cameras; as a result $z_{radarFFT}$ extended up to -15 m whilst $z_{videoCS}$ only extended up to -10 m.

Both the bias (Figure 2.5) and ϵ_{RMS} (Figure 2.6) in $z_{videoCS}$ possess a distinct alongshore variability that is nearly absent for $z_{radarFFT}$. High bias and ϵ_{RMS} are found along the seams of the video cameras (grey lines in Figure 2.5b and Figure 2.6b), especially at a large distance from the video station. The alongshore variability in bias and ϵ_{RMS} may be due to either a poor synchronisation of the cameras or the lack of an up-to-date geometry solution for some of the cameras. Although the highest deviations in $z_{videoCS}$ can be found along the seams of the cameras, inaccurate geometry solutions also undermine the estimation of $z_{videoCS}$ within

Table 2.2: Accuracy assessment on bed elevation z_b derived from X-band radar with an FFT method and Argus video with a cross-spectral method, and compared to *in situ* measurements at the Sand Engine

Technique	Depth range	Bias z_b	$\epsilon_{RMS} z_b$
<i>In situ</i>	-15 m $\leq z_b \leq 1$ m	0 m	0.1 m
Radar	-15 m $\leq z_b \leq -9$	1.0 m	1.0 m
	-9 m $< z_b < -6$ m	-0.02 m	0.40 m
	-6 m $\leq z_b \leq 0$ m	-2.3 m	2.7 m
Video	-10 m $\leq z_b \leq -5$	0.59 m	0.79 m
	-5 m $< z_b < -1$ m	-0.01 m	0.34 m
	-1 m $\leq z_b \leq 0$ m	-0.92 m	1.0 m

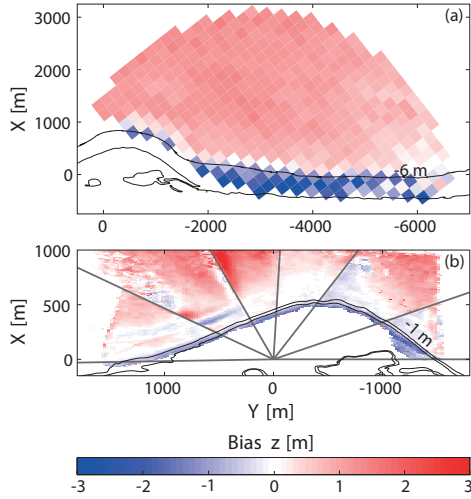


Figure 2.5: Spatial variability in bias of (a) radar-derived bed elevation with an FFT method, z_{radarFFT} , and (b) video-derived bed elevation with a cross-spectral method, z_{videoCS} . Red (blue) colours imply z_{radarFFT} and z_{videoCS} to be shallower (deeper) than *in situ* bed elevation. The thin black lines indicate the contour at 0 m, -1 m, and -6 m MSL, whereas the thicker grey lines in (b) indicate the camera seams

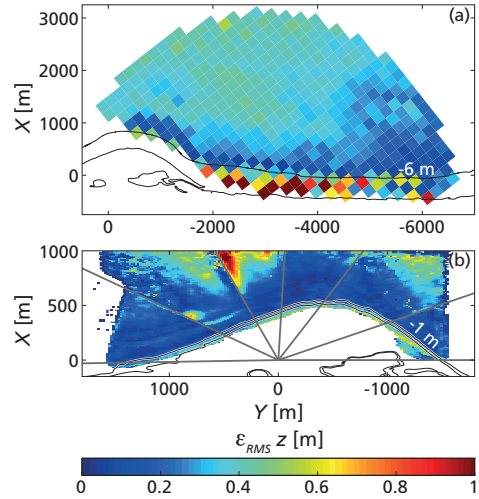


Figure 2.6: Spatial variability in root-mean-square error of (a) radar-derived bed elevation with an FFT method and (b) video-derived bed elevation with a cross-spectral method. The black line indicates the contour at 0 m, -1 m and -6 m MSL. The thicker grey lines in (b) indicate the camera seams.

the field of view. Also, some alongshore variability in the ε_{RMS} of z_{radarFFT} arises shoreward of the -6 m contour, but to a rather small amount compared to z_{videoCS} .

Overall, the bias and ε_{RMS} are generally larger than the error in jet-ski and ship measurements, which have a vertical accuracy of 0.1 m during calm seas (Van Son et al., 2010). This justifies the use of the jet-ski measurements as ground truth for the validation in this study and confirms that the determined deviations of z_{radarFFT} and z_{videoCS} from $z_{\text{in situ}}$ are significant. Given that the jet-ski measurements could only be conducted during calm weather conditions, the potential negative effect of high energetic conditions on the accuracy of z_{radarFFT} and z_{videoCS} (as pointed out by Holman et al., 2013) could not be tested.

2.5 Discussion

2.5.1 Bias in bed elevation estimates

The results of the bathymetric comparison (Section 2.4) reveal a systematic positive bias in z_{radarFFT} and z_{videoCS} (Table 2.2). A positive bias at relative water depths similar to our site ($h > 6$ m, under a wind wave climate) can be seen in the data presented by Bell (2001, his Figure 10) for Teignmouth, United Kingdom, and by Bell (2002, his Figure 10) for Egmond aan Zee, The Netherlands. Also, Holman et al. (2013) found a positive bias in bed elevation of approximately 1 m in depths larger than 7 m at Agate Beach, United States, but only under waves with a relatively short period of 7 s. In these studies, the system set-up of the radar (Bell, 2001; Bell, 2002) and video (Holman et al., 2013), in terms of far range (~ 1 km) and sampling scheme, was similar to the setup at the Sand Engine.

At shallower depths, $z_b \geq -6$ m, Figure 2.3 shows that the performance of the radar-FFT approach starts to degrade substantially. Although the magnitude of the bias differs here for z_{radarFFT} and z_{videoCS} , the direction of the bias is systematically negative. Previous studies using an FFT method produced larger values for the bias and ε_{RMS} than those that were using a cross-spectral method. For example, Bell et al. (2004) found an even higher bias in shallow water up to -2.5 m, compared to -2.3 m at the Sand Engine, when using a radar-FFT approach wherein window lengths were 240 m. Trizna (2001), using a radar-FFT approach, found a bias of -0.5 m in shallow water ($z_b = -3.6$ m), which increased with offshore wave height up to -4 m under a root-mean-square wave height H_{rms} of 3 m. We found a higher accuracy with a cross-spectral method, providing bed elevation with only a -0.92 m bias in shallow water. Holman et al. (2013) found a similar (-0.2 m) bias for Duck, United States. Bell (2001), who obtained wave number maps with image analysis techniques for several frequency maps, estimated depth at Egmond aan Zee, The Netherlands and Teignmouth, United Kingdom and found a $O(1$ m) bias.

The bias in inverted depth found at the Sand Engine and in earlier studies depends on the method of Ω - k retrieval, certain sensor properties, the model, and the local environmental and physical boundary conditions. In this study, the method of Ω - k retrieval and the sensor properties explain differences in accuracy of z_{radarFFT} and z_{videoCS} . The model may explain the systematic bias in z_{radarFFT} and z_{videoCS} . Environmental and physical boundary conditions may have been slightly different around the video station and radar station, which are separated by approximately 4 km. However, this offset does not explain either the systematic bias or the shallow water collapse of the FFT method. Below, we discuss potential sources of bias in z_b , introduce a guideline on the applicability of a radar-FFT and a video-CS approach to derive z_b in a large nearshore region, and as a practical application of z_{radarFFT} and z_{videoCS} we present a volumetric analysis.

2.5.2 Sources of bias

Ω - k retrieval

Cross-spectral methods are expected to outperform FFT methods where the wave field is inhomogeneous within an analysis window. An inhomogeneous wave field arises by cross-shore transformation of the waves, e.g. shoaling and breaking, and is dependent on z_b , but also wave length and wave height. A homogeneous wave field is crucial for our radar-FFT approach and other FFT methods. At the same time, FFT methods demand analysis windows with substantial spatial coverage; as a result, the requirement of homogeneity is fulfilled over a limited range of the nearshore zone only. Based on our findings, we determined an onshore limit up to where the FFT method can be applied confidently, by relating the bias in bed elevation to a proxy for wave inhomogeneity. The proxy we used is the dimensionless local bed elevation change $\Delta z_b / \bar{z}_b$, wherein Δz_b is the maximum bed elevation change and \bar{z}_b is the mean bed elevation, both computed for each analysis window. To reduce the sensitivity of Δz_b to single extreme values in z_b we defined Δz_b as the difference between the 5th and 95th percentiles in z_b . Figure 2.7 illustrates that the bias in bed elevation derived with the FFT method decreases rapidly below 0 m for $\Delta z_b / \bar{z}_b > 1.2$, whereas the bias for the cross-spectral method changes gradually from positive to negative with increasing $\Delta z_b / \bar{z}_b$. The sensitivity of the onshore FFT-limit, $\Delta z_b / \bar{z}_b > 1.2$, would be worthwhile to test for different wave conditions, a smaller size of the analysis windows, and at sites with a complex bathymetry (e.g. tidal inlets). However, large windows are required for depth-inversion with an FFT method in order to have a sufficient resolution in the spectral domain, i.e. the size of the window W and length of the time series S is related to the spectral resolution as W^{-1} and S^{-1} (Piotrowski

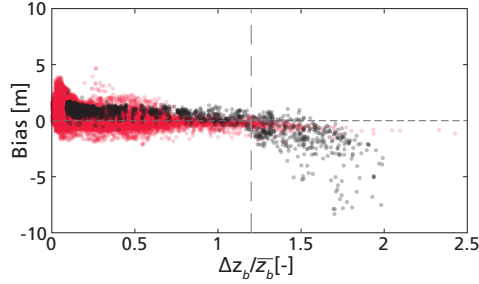


Figure 2.7: Bias of radar-derived bed elevation using an FFT method (black dots) and video-derived bed elevation using a cross-spectral method (red dots), as a function of the local dimensionless change in bed elevation, $\Delta z_b/\bar{z}_b$. The vertical dashed line represents the suggested onshore limit on the FFT method.

and Dugan, 2002). Piotrowski and Dugan (2002) found that a reduction in size of the window (from 512 m to 128 m) or length of the time series (from 120 s to 16 s) yielded a lower accuracy of z_b . The large analysis windows in FFT methods inhibit to estimate bathymetry with high detail. Therefore, a cross-spectral method is preferred where morphological spatial scales become finer (e.g. surf zone). Note that in long-term monitoring programs a smart sampling scheme is required to minimise data size, to enable continuous data collection and data storage, and to limit computation time. At our site, such a sampling scheme existed for the video system, but not for the radar. Note that in the radar-FFT approach, the accuracy of estimated Ω and k also decreased when currents were poorly estimated.

Experimental set-up

A bias in $z_{videoCS}$, up to 3 m, along the seven seams of the Argus cameras may have resulted from inaccurate camera synchronisation or poor image geometry. Both problems cause a mismatch of the wave pattern at the camera seams. The X-band radar had a single seam and therefore hardly produces such errors. Potentially, seam-induced deviations can be solved by estimating $z_{videoCS}$ per camera and merging the estimates subsequently, instead of merging pixel time series first and estimating $z_{videoCS}$ subsequently (Bergsma et al., 2016). Moreover, in long-term morphologic monitoring programs, permanent GCPs or periodically surveyed GCPs are essential.

Near the sea-land interface, analysis windows cover the beach partly. Pixel time series do not contain a wave signal where the windows cover the beach. Consequently, the window contains more wet pixels seaward, usually covering deeper water, than landward of the analysis point. As a result bed elevation will be too deep. We recommend to limit analysis to analysis windows with wet pixels only.

The settings of the radar are suboptimal for our site with small period waves. For example, both the rotation time and the range resolution are relatively large (~ 2.84 s and ~ 7 m) with respect to the typical wave conditions. Potentially, small amplitude waves at far range were shadowed to the radar by larger amplitude waves in front. As a result, wave periods may be overestimated, and, given Eq. (2.1), z_b becomes too shallow. Wave shadowing becomes increasingly important for a low grazing angle of the radar, but whether wave shadowing is important at our site is unknown. The positive bias found by Bell (2001) and Bell (2002) and by Holman et al. (2013) (Agate Beach) may have had the same nature, since all these studies used sensors that looked at far range (>1 km) and collected data under small period waves.

Model

At the Sand Engine, z_{radarFFT} and z_{videoCS} have a positive bias in deeper water. Such bias was not recognised at the test site of cBathy, Duck, with the exception of a single camera (Holman et al., 2013; see their Figure 3). Aside from their comment that the camera had the lowest resolution and lens quality of the site, no explanation on the bias was given. The Sand Engine is different from Duck regarding the wave climate, short period wind waves compared to long period swells, and the cross-shore range of the cameras, 1 km compared to 500 m. Shorter period waves reach deep water conditions, where the wave speed is not affected by the bed anymore, at smaller depth than long period waves. Within the depth-inversion algorithms quality control steps are needed to limit depth-inversion to the nearshore zone where waves are affected by the bed. Within cBathy the quality control is one potential explanation for the positive bias. cBathy fits the dispersion relation to depths smaller than a fixed, user-defined depth threshold. Near the user-defined threshold, z_{videoCS} has a positive bias because slightly larger depths are removed and the fit is based on wave speed corresponding to slightly shallower depths only. How SeaDarQ handles quality control and how that potentially affects the accuracy of z_{radarFFT} is unknown to us. Positive bias observed by Bell (2001) and Holman et al. (2013) also arose under short period waves. The positive bias in z_{radarFFT} and z_{videoCS} in large depths may be reduced by defining a seaward boundary, dynamic in time and space, for applying depth-inversion. Here, further work is required for software implementation and testing.

A bias in bed elevation may arise when neglecting currents in the dispersion relation, as in cBathy. Currents opposing the wave direction shorten the wavelength, whereas currents following the wave direction lengthen the waves. However, bed elevation derived with SeaDarQ, which accounts for currents, shows similar deviations as those derived with cBathy. Moreover, the deviations are systematically negative in shallow water and positive in deeper water, while a current-induced bias changes with the direction of the current. Therefore, neglecting currents seems no important source of error at our site. In environments where currents are strong and not perpendicularly directed to the waves, e.g. tidal inlets, depth estimates need to be interpreted carefully for inversion algorithms that neglect current effects.

Too deep estimates of z_{radarFFT} and z_{videoCS} in shallow water may be caused by infragravity waves, i.e. long period (30-100 s) waves, which become of increasing importance when approaching the coast. Using laboratory data, Tissier et al. (2015) illustrated that infragravity waves can affect the propagation of individual short waves, such that they merge (bore-bore capture). Surprisingly, they found that this had no effect on the bulk wave celerity, suggesting that the effect of the infragravity waves on depth-inversion is probably small. To sum up, accounting for infragravity waves in the model seems not necessary.

Although bed elevation is known to be estimated too deep in shallow water by a model based on linear wave theory (Holland, 2001; Tissier et al., 2011), the model functions properly throughout a large part of our domain. Potentially, shallow water estimates can be improved by including wave height in the empirical relationship Eq. (2.1), as shown by Grilli (1998) for a series of synthetic cases, by Catálan and Haller (2008) for a laboratory data set, and by Yoo et al. (2011) for a field data set. Their approaches cannot be applied directly at the Sand Engine, because computational costs become excessive for the extent of our study site. Furthermore, Grilli (1998) considered shoaling waves only and Yoo et al. (2011) used a computational model to invert water depth in the surf zone that is infeasible for the size of our study area and the \sim hourly sample intervals of the radar and video system. Therefore, a simple approach is required to account for wave non-linearity at the Sand Engine. Bell et al. (2004), for example, used a modified version of linear wave theory (Booij, 1981), given by

$$\Omega = \sqrt{gk \tanh(k(h + Z))} \quad (2.3)$$

with Z depending on local wave height. Because waves in the field are not monochromatic, Holland (2001) suggested Z to depend on a wave statistic as $Z = 0.42H_s$ to $0.48H_s$. Bell et al. (2004) choose $Z = 0.4H_s$ with H_s obtained from an offshore buoy and found the shallow water bias to reduce from approximately -2.5 m to -0.1 m, using analysis windows with a length of 32 m. This small window size was possible because a different type of radar (mm wave (MMW) radar) was used with spatial resolutions < 1 m, recording the sea surface within 200 m from the shoreline ($z_b > -3$ m). Alternatively, depth estimates in shallow water can be improved by a model not including wave height. For example, linear wave speed multiplied by a factor, 1.3 following Stive (1984) or 1.14 following Tissier et al. (2011), improved wave speed estimates for a laboratory experiment and for a field study, respectively. Further work is needed to see how these modifications affect the present z_b estimates in shallow water ($-3 \text{ m} < z_b < 0 \text{ m}$).

Besides improvement of depth-inversion techniques, alternative techniques may be able to estimate z_b accurately near the shoreline. For example, z_b can be computed across the beach profile by tracking the location of the shoreline and estimating the elevation of the water run-up (Aarninkhof et al., 2003; Bell et al., 2016). A combination of techniques based on depth-inversion and wave dissipation were tested by Morris (2013) and Chatzistratis (2014). Morris (2013) showed that ε_{RMS} of about 0.7 m in the inner surf zone improved by 20% when combining $z_{videoCS}$ with z_b based on dissipation patterns, using BeachWizard (Van Dongeren et al., 2008) at Duck, North Carolina. Chatzistratis (2014) improved z_b for $-3 \text{ m} < z_b < 0.5 \text{ m}$ at Egmond aan Zee, The Netherlands, by combining $z_{videoCS}$ with z_b based on mapping of the shoreline, reducing the bias and ε_{RMS} by 50% to -0.27 m and 0.42 m, respectively. None of these combinations are yet fully operational.

2.5.3 Sand budgets and data fusion

Aiming for a practical application (Grunnet and Hoekstra, 2004; Van Duin et al., 2004) of depth-inversion, the sand volume V was computed from $z_{radarFFT}$, referred to as $V_{radarFFT}$, and from $z_{videoCS}$, referred to as $V_{videoCS}$. Predefined boxes were used that were restricted in the vertical by a lower and upper level (Figure 2.8). The lower and upper boundary were marked by the -8 m and -1 m MSL contour in the *in situ* measurements of March 2013. The -8 m contour is used by coastal managers in the Netherlands as lower boundary when computing V as indicator for coastal safety. Our boxes have a deeper upper boundary at -1 m MSL, compared to $+3$ m in coastal zone management, and thus do not contain the intertidal and

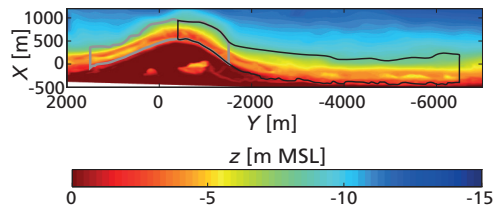


Figure 2.8: Areas used to compute the volume of radar-derived bed elevation with an FFT method, $z_{radarFFT}$ (black lines) and video-derived bed elevation with a cross-spectral method $z_{videoCS}$ (grey lines), defined between the -8 m MSL and the -1 m MSL contour lines.

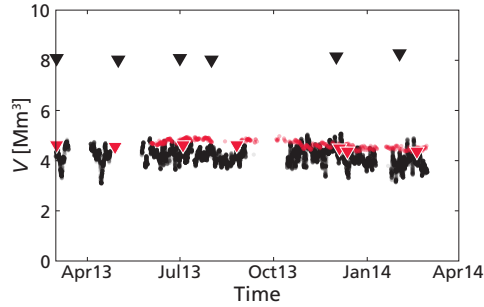


Figure 2.9: Sand volume V computed over the radar-derived bathymetry with an FFT method (black dots) and over the video-derived bathymetry with a cross-spectral method (red dots), see Figure 2.8. The triangles indicate volumes derived from *in situ* measurements.

supratidal zone. For reference, V was also computed from $z_{in situ}$, referred to as $V_{in situ}$, using the same boxes that were used to estimate $V_{radarFFT}$ and $V_{videoCS}$.

$V_{radarFFT}$ is an underestimate of $V_{in situ}$, of approximately 3.9 Mm^3 , whereas $V_{videoCS}$ is an overestimate of $V_{in situ}$, of approximately 0.1 Mm^3 (Figure 2.9). Although $V_{videoCS}$ compare reasonably well with those computed from measured bathymetry, this is because of cancelling of the errors over the spatial extent of the volume computations. Negative bias at shallow depths and positive bias at larger depths average out at our study site for the domains we have defined. However, a differently defined domain would rather imbalance the offsets and thereby the computed volumes could be completely wrong, as can be seen for $V_{radarFFT}$ (Figure 2.9). Therefore, a potential subdivision of the domain in several boxes, revealing net spreading of sediment from the centre of the Sand Engine to the adjacent coast (De Schipper et al., 2016), will yield a signal similar to the domain-wide V and thus will be dominated by errors. Daily variability in $V_{radarFFT}$, up to 1.3 Mm^3 , and in $V_{videoCS}$, up to 0.15 Mm^3 , is unlikely to be caused by wave and current action; instead we believe it reflects noise in estimated bed elevation and accordingly volume. A certain weekly to monthly variability in volume might exist, but whether variability in $V_{radarFFT}$ and $V_{videoCS}$ is realistic cannot be assessed by the lack of *in situ* surveys at such timescales. Given the steady signal of $V_{in situ}$ (Figure 2.9), its potential seasonal variability seems limited.

In principle, data products from multiple sensors can be fused to a single product, presuming that a fused product contains more information than the individual products. Accuracies of the individual data sets, as determined here for $z_{radarFFT}$ and $z_{videoCS}$, are required to weigh each data point when fusing individual data sets. Potentially, fused bathymetric maps will help to better understand large and highly dynamic coastal environments, such as the Sand Engine. For data-fusion purposes, the different sensors are preferably co-located to have sufficiently overlapping footprints with a dense spatial resolution of the acquired data in the region of interest. At the Sand Engine, unfortunately, the radar and video station are too far apart (4 km) to test data fusion properly. In addition, substantial improvements are required for both the FFT method and the cross-spectral method before the fused data are of practical use in sand budget studies. This is illustrated by the volumetric calculations, which should be used carefully with both depth-inversion algorithms (as shown above).

2.6 Conclusions

Bed elevation z_b was derived through depth-inversion using two shore-based sensors, two methods that retrieved wave frequency Ω and wave number k and a single, simple model over a large ($\sim 3 \text{ km}^2$) nearshore region around the Sand Engine. Its accuracy was assessed by comparison with *in situ* measurements. We found that z_{radarFFT} , bed elevation derived from X-band radar with an FFT method for Ω - k retrieval, and z_{videoCS} , bed elevation derived from Argus video data with a cross-spectral method for Ω - k retrieval, can complement each other: radar covers up to deeper water but the video-CS approach is more accurate in shallow water. Nevertheless, they both have a systematic bias, with bed elevation estimated as too shallow in deeper water and too deep in shallow water. Estimates of z_{radarFFT} were too shallow by 1.0 m deeper than -9 m MSL , similarly z_{videoCS} was too shallow by 0.59 m deeper than -5 m MSL . In shallow water, z_{videoCS} was too deep with -0.92 m for $z_{\text{in situ}} \geq -1 \text{ m MSL}$, whereas z_{radarFFT} was too deep by 2.3 m for $z_{\text{in situ}} \geq -6 \text{ m MSL}$. At intermediate depths, bias in z_{radarFFT} and z_{videoCS} was negligible, -0.02 m and -0.01 m respectively. The magnitude of the determined biases apply to calm weather conditions. A potential negative effect of high-energetic conditions on z_{radarFFT} and z_{videoCS} could not be tested by the lack of *in situ* surveys during such conditions. The large bias of z_{radarFFT} arises by the collapse of the FFT method in shallow water where the wave field was inhomogeneous in the 960 m by 960 m analysis windows. Other bias at shallow depths is partially explained by the model which is known to neglect the important effect of the wave amplitude on the phase speed in shallow water. The bias in deeper water may be due to inverting depth where waves are insensitive to the bed. In addition, certain sensor properties contributed to the bias in z_{radarFFT} and z_{videoCS} . That is, video has the disadvantage of seams between the cameras and the necessity of accurate time synchronisation of the cameras. Also, depth estimated over analysis windows that contained partly dry pixels at the sea-land interface may have contributed to the bias at shallow depths. Currently, the radar-FFT approach and video-CS approach are not sufficiently accurate for volumetric computations with the same accuracy as possible with *in situ* surveys. The bias in $z_{\text{estimated}}$ translates in a bias in volume that depends on the domain considered for volume computation. Temporal variability in estimated volumes at daily to monthly timescales seems unrealistic, but cannot be tested due to the lack of *in situ* surveys at these time scales.

Acknowledgement

J.R. and B.G.R. were supported by the Dutch Technology Foundation STW that is part of the Dutch Organisation for Scientific Research (NWO), and which is partly funded by the Ministry of Economic Affairs, under contract 12686 (Nature Coast: S1 Coastal Safety). We thank Prof. dr. R.A. Holman for providing the cBathy code, the stimulating discussions and his review. We would also like to thank three anonymous reviewers for their extensive feedback.

Chapter 3

Observations on sandbar behaviour along a man-made curved coast

Based on: Rutten, J., B.G. Ruessink, and T.D. Price (2018), Observations on sandbar behaviour along a man-made curved coast. *Earth Surface Processes and Landforms* 43, 134-149.

Abstract

Sandbars, submerged ridges of sand parallel to the shoreline, affect surf zone circulation, beach topography and beach width. Under time-varying wave forcing, sandbars may migrate onshore and offshore, referred to as two-dimensional (2D) behaviour, and vary in planshape from alongshore-uniform ridges to alongshore non-uniform ridges through the growth and decay of three-dimensional (3D) patterns, referred to as 3D behaviour. Although 2D and 3D sandbar behaviour is reasonably well understood along straight coasts, this is not the case for curved coasts, where the curvature can invoke spatial variability in wave forcing. Here, we analyse sandbar behaviour along the ~ 3000 m man-made curved coastline of the Sand Engine, The Netherlands, and determine the wave conditions governing this behaviour. Two- and three-dimensional behaviour were quantified within a box north and west of the Sand Engine's tip, respectively, using a 2.4-year dataset of daily low-tide video images and a sparser bathymetric data set. The northern and western sides behaved similarly in terms of 2D behaviour, with seasonal onshore and offshore migration, resulting in a steady position on inter-annual timescales. However, both sandbar geometry and 3D behaviour differed substantially between both sides. The geometric differences (bar shape, bar crest depth and wavelength of 3D patterns) are consistent with computed alongshore differences in breaker height due to refraction. The differences in the timing in growth, decay and morphological coupling of 3D patterns in the sandbar and shoreline are likely related to differences in the local wave angle, imposed by the curved coast. Similar dependency of bar behaviour on local wave height and angle may be expected elsewhere along curved coasts, e.g. shoreline sandwaves, cusped forelands or embayed beaches.

3.1 Introduction

Sandbars are shallow submerged ridges parallel to the shoreline that characterise many wave-dominated beaches throughout the world. These features, forming the first line of natural coastal defence against storm waves, have a dynamic character that has intrigued the nearshore scientific community for decades. Nowadays, we have a reasonable understanding why sandbars migrate slowly onshore under calm wave conditions and rapidly offshore under more energetic conditions (e.g. Thornton and Humiston, 1996; Gallagher et al., 1998; Elgar et al., 2001; Hoefel and Elgar, 2003). Additionally, many studies (Sonu, 1973; Wright and Short, 1984; Lippmann and Holman, 1990; Van Enckevort and Ruessink, 2003b) have investigated the growth and decay of seaward and shoreward protrusions in cross-shore sand-

bar position, resulting in a three-dimensional (3D) geometry with alongshore variability in depth and cross-shore position and in a two-dimensional (2D), alongshore-uniform sandbar geometry, respectively. The protrusions generally tend to form under calm conditions after storms or in the summer season, and tend to disappear under high waves (Wright and Short, 1984) or under obliquely incident waves driving a strong alongshore current (Price and Ruessink, 2013; Contardo and Symonds, 2015). Although numerous studies examined sandbar behaviour along straight coasts, both in natural systems (Lippmann and Holman, 1990; Van Enckevort and Ruessink, 2003b) and human-disturbed systems (Grunnet and Ruessink, 2005; Ojeda et al., 2008), sandbar behaviour along strongly curved coasts has received less attention and is thus not well understood. Nowadays, insight into the effect of a curved coast on system behaviour is demanded with the recent shift in nourishment policy towards large-scale and long-term measures that serve on decadal timescales over kilometers of coast; see Stive et al. (2013). Kilometer-scale perturbations in the coastline, intended to feed the adjacent beach or to reinforce the coastal strip, have recently been constructed to keep up the current coastal safety levels in view of rising sea levels due to climate change and continuing coastal erosion (Stive et al., 2013; Wong et al., 2014). An example of such a perturbation is the Sand Engine, a concentrated feeder nourishment in The Netherlands (De Schipper et al., 2016). Initially, the nourishment protruded 1 km into the sea and extended 3 km alongshore, resulting in a strongly curved coast with varying coastline orientation with respect to the offshore wave conditions. Observations suggest that this curvature affected the behaviour of the newly-developed sandbars along the perturbation (e.g. Chong, 2014). The sandbar planshapes varied from alongshore-variable (3D) along the entire perturbation (Figure 3.1b) to dissimilar configurations at both sides of the perturbation (Figures 3.1a,c).

Analogues of barred curved coasts can be found in natural systems. Convex analogues comprise shoreline sandwaves and cusped forelands, whereas embayed beaches form concave analogues. Few studies concern sandbar behaviour along convex coasts. Stewart and Davidson-Arnott (1988) and Davidson-Arnott and Van Heyningen (2003) found that the welding of sandbars to the beach resulted in the generation, growth and alongshore migration of longshore sandwaves (wavelength of 500-2500 m, lifetime of 5-10 yr) along Long Point spit (Lake Erie), Canada. On the downdrift side of these sandwaves, they observed rhythmic inner bars to migrate onshore and eventually weld to the beach. No observations were reported on sandbar behaviour at the updrift side. The observed bar behaviour was attributed to both sediment abundance in the inner nearshore zone and to low, obliquely incident waves in spring and summer. Aagaard and Kroon (2007) found opposite long-term bar behaviour along the two flanks of a cusped foreland, Blåvands Huk, Denmark. Net offshore migration was observed where the profile had a relatively steep shoreface (1:210, between -7 and 0 m with respect to Mean Sea Level (MSL)) with pronounced (up to 3 m) sandbars, whereas net onshore migration was observed where the shoreface profile was more gentle (1:370). Model simulations suggested that seaward transport due to strong undertow currents dominated over the steep profile with a pronounced bar morphology, whereas shoreward transport due to wave skewness dominated over the gentle profile with less voluminous sandbars. Opposite fluxes in littoral drift may also have contributed to inter-site differences in either shoreface profile or bar behaviour itself. Backstrom et al. (2008) found alongshore differences in morphological response across the shoreface of a cusped delta, southern Spain, from a pre-storm and post-storm bathymetric survey. Minor change in sandbar morphology was observed along the eastern side where waves arrived shore-normally, whereas substantial change was recorded within the double bar system along the southern side where waves arrived obliquely. They were inconclusive whether alongshore currents or rip currents drove the morphological change of the double bar system at the southern side.

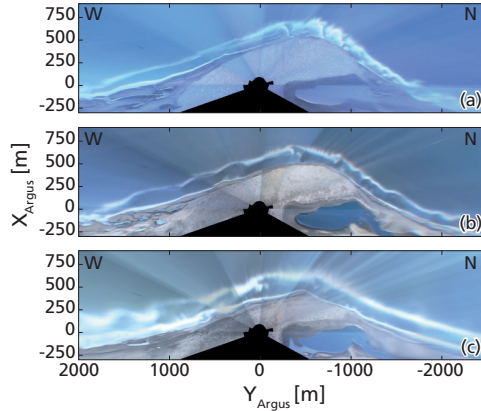


Figure 3.1: Examples of plan view images on (a) 4 June 2013 (b) 23 November 2013 and (c) 24 January 2015, illustrating the dynamics of the sandbar and shoreline morphology along the convex coastline of the Sand Engine.

Although concave beaches are more abundant and have received more attention than convex beaches, the alongshore differences in sandbar behaviour have not often been subject of study. However, some observations have been made along the concave coast of embayed beaches, enclosed by one or two headlands, bluffs or man-made structures. Short (1978) and Wright and Short (1984) observed an alongshore gradient in modal beach state along the embayment of Fisherman's-Collaroy-Narrabeen, Australia, from reflective at Fisherman's, associated with low energetic conditions, through low-tide-terrace and transverse-bar-rip at Collaroy, to rhythmic-bar-beach at Narrabeen, associated with moderate energetic conditions (Short, 1978, his Figure 7; Wright and Short, 1984, their Figure 8). Along Monterey Bay, USA, a similar energy-gradient in modal beach state was reported by Thornton et al. (2007), from reflective states in the southern end of the embayment to intermediate states halfway of the embayment. Such energy-gradients can be explained by the geometry of the embayment and the wave conditions. An alongshore gradient in breaker wave height arises under obliquely incident waves due to shadowing effects by one of the headlands. As a result, embayments that are exposed to a wave climate with predominantly oblique waves tend to have an alongshore gradient in wave energy, and thus, in modal beach state. Besides an alongshore gradient in breaker wave height, the embayment geometry may also induce alongshore differences in wave refraction, diffraction and reflection. Such alongshore differences lead to an alongshore gradient in wave angle that may further contribute to an alongshore variation in modal beach state. To illustrate, model simulations of Tairua Beach (Gallop et al., 2011) and Bondi Beach (McCarroll et al., 2016), two embayments with a longshore variation in bar morphology, revealed an alongshore gradient in wave energy, arising from asymmetric geologic boundary conditions at both sites. At Tairua Beach a nearby island resulted in wave shadowing and at Bondi Beach one of the headlands and a subaqueous reef locally reduced wave heights. Besides a modal state, alongshore variability in 2D and 3D sandbar morphology may change with time-varying wave conditions, depending on the responsiveness of the system. For shoreline datasets, for example interannual (Ranasinghe et al., 2004b; Ojeda et al., 2011), seasonal (Harley et al., 2015) and event (Van de Lageweg et al., 2013) signals in alongshore variable 2D and 3D behaviour were found. Similarly, sandbar behaviour may vary alongshore, as found by Gallop et al. (2011) and McCarroll et al. (2016), showing that a sandbar migrated offshore under storm conditions at the exposed side of the beach only. In

addition, Ojeda et al. (2011) and Blossier et al. (2016) reported on the rotation of a sandbar due to longshore differences in 2D behaviour, similar to beach rotation (e.g. Harley et al., 2015). Different to the convex examples, embayed beaches have physical lateral boundaries that potentially limit alongshore exchange of sand outside the system, promote trapping of sand within the system (i.e. beach rotation) and control headland rip formation. Moreover, the concave shape creates a gradual alongshore change in local wave forcing, whereas the local wave forcing along a convex coastline changes rather abruptly across its most seaward protruding point.

On kilometer-scale, the behaviour of convex coasts (e.g., evolution of shoreline sand-waves) or concave coasts (e.g., beach rotation) themselves have been studied extensively. The superimposed morphologic meso-scale features ($O(10-100\text{ m})$), such as sandbars, may importantly affect the underlying, large-scale morphodynamics (e.g. Stewart and Davidson-Arnott, 1988; Harley et al., 2015). However, the meso-scale behaviour along curved coasts remains relatively unknown. Studies on sandbar behaviour at concave coasts mainly examined temporal variability in beach states (Wright and Short, 1984; Ranasinghe et al., 2004a), morphologic coupling (Van de Lageweg et al., 2013), and rip channels or 3D bar morphology (Holman et al., 2006; Splinter et al., 2011; Ojeda et al., 2011). The spatial variability herein received minor attention, especially bar behaviour at daily to seasonal timescales. Moreover, the few studies addressing sandbar behaviour along convex coasts were based on data sets with low temporal resolution or of short duration. Herein, we use a 2.4-year data set of daily low-tide, ten-minute averaged Argus video images (Holman and Stanley, 2007), collected from the convex, curved coast of the Sand Engine, which offers the unique opportunity for studying bar behaviour along a convex coastline. The aim of this chapter is (1) to describe the spatiotemporal variability in sandbar behaviour along the convex curved coast of the Sand Engine at daily to seasonal timescales and (2) to determine the wave conditions governing this behaviour. First, we describe the study site, data set and analysis methods in Section 3.2. Then, we present our results on sandbar behaviour, preceded by a subsection on large-scale evolution of the Sand Engine since its construction (Section 3.3). This is followed by a discussion on the wave field and resulting wave-induced currents governing the observed sandbar behaviour, particularly focusing on the breaker wave height and the wave angle (Section 3.4). Finally, we provide the main conclusions of our work in Section 3.5.

3.2 Methodology

3.2.1 Study site

The study is performed at the 21.5 Mm^3 Sand Engine, a concentrated sand nourishment along the southwest-northeast (42° with respect to the North) oriented Delfland coast, The Netherlands (Figure 3.2). The Sand Engine was constructed in summer 2011 with the aim of feeding the beaches of the erosive Delfland coast under predicted sea level rise, in a more efficient and environmentally-friendly form than traditional nourishments placed locally at the beach or at the shoreface (Stive et al., 2013). The peninsula consists of sediments with an average D_{50} of $\sim 280\ \mu\text{m}$ (De Schipper et al., 2016), slightly coarser than the median grain size $\sim 250\ \mu\text{m}$ (Wijnberg and Terwindt, 1995) before construction of the Sand Engine.

The study site is exposed to a bimodal wave climate, with waves predominantly from the southwest (222° N) or north-northwest (347° N ; Figure 3.2). The yearly-averaged offshore significant wave height H_s is 1.3 m, with a yearly-averaged peak period T_p of 5.7 s. Typically, T_p increases with H_s , and is largest for waves from the northwest which have the largest fetch. Summer (April-September) is characterised by low waves ($H_s = 1.1\text{ m}$), whereas storms (H_s ,

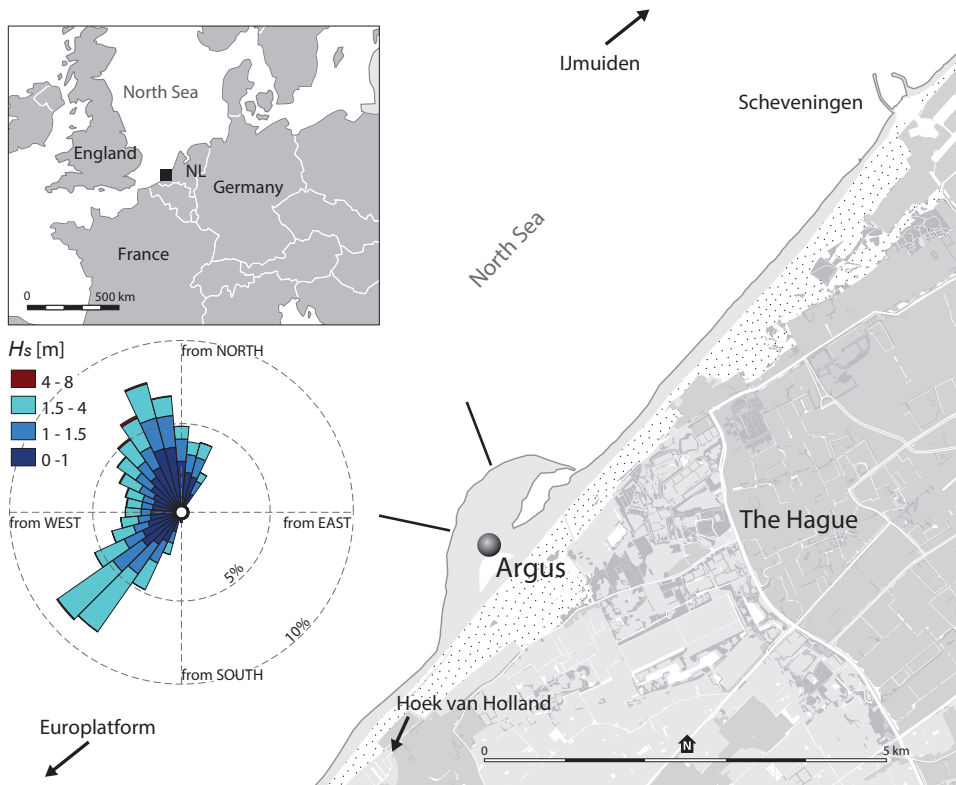


Figure 3.2: Study site. Depth contours are roughly parallel to the coast, and contract (until 10 m depth) at the perturbation. The black lines at the Sand Engine show the transects of the profiles shown in Figure 3.6. The wave rose shows offshore wave measurements for the period 2005-2015. The dots depict the dunes, whereas the greyish colours inland represent built-up area.

up to 5 m) dominate the autumn and winter season (September-April). The semi-diurnal tide imposes a tidal range of 1.7 m and drives a tidal current parallel to the shore with peak velocities of about 0.5 m/s. The wave climate, in particular in relation to the observations on sandbar and shoreline behaviour, is further analysed in Section 3.4.

3.2.2 Image and field data

A 2.4-year data set of daily video images was collected by an Argus video station, between March 2013 and July 2015. Eight 5.0 Mega Pixel cameras, 42.7 m above mean sea level (MSL) mounted atop a tower, recorded 245 degrees of the horizontal plane. The images of the eight cameras were rectified and merged to a single plan view image (Figure 3.3) using two inverted photogrammetric equations (Holland et al., 1997) with input on the camera position, camera orientation (tilt, pitch, roll) and focal length. The orientation of each camera was calculated using Ground Control Points (GCPs) on the beach that were within the field of view and of which the coordinates were known. After an initial set of camera orientations based on temporary GCPs, camera orientations changed slightly due to strong wind or thermal expansion, and thus the orientations were updated regularly when GCPs were within the view of the camera (cameras 1, 2, 3, 4, 7, 8). Focal length, field of view and the correction for

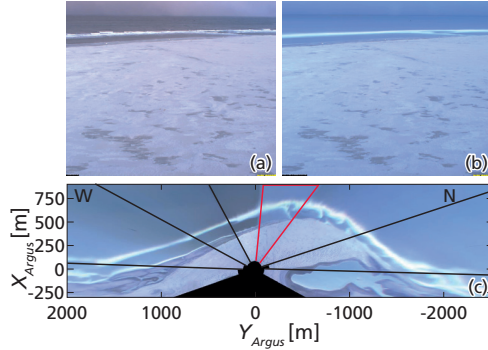


Figure 3.3: Example of (a) a snap shot, (b) a 10-min time-exposure image and (c) a merged planview. The black lines in (c) represent the camera seams, where the red delineated part corresponds to the time-exposure image shown in (b).

radial lens distortion were determined in the laboratory. The eight images were projected on the local Argus coordinate system, with the x -axis directed offshore, the y -axis directed to the southwest (220°) along the beach and z constant at the tidal level. The images covered 1200 m in the cross-shore and 4500 m in the alongshore direction, and had a grid resolution of 2×2 m. Pixel footprints increased from 0.03×0.2 m at 200 m to 0.2×1.2 m at 1000 m from the Argus station. For this study, we used 778 ten-minute time-exposure (timex) images. In these images the individual waves are averaged out, instead white, alongshore coherent lines can be distinguished as a result of time-averaged wave breaking over the shallow sandbars (Lippmann and Holman, 1989; Van Enckevort and Ruessink, 2001; Figure 3.3). Figure 3.1 shows examples of such breaker lines at our study site; varying in both space and time, from straight at either the northern and/or western side to undulating lines, with seaward and shoreward protrusions, at any of the sides. The images show two breaker lines, where the seaward (outer) line serves as proxy for the sandbar and the shoreward (inner) line represents the shoreline. In *Appendix A* we show that the video-derived position resembles the *in situ* measured bar crest or shoreline with an accuracy of $O(10$ m), consistent with Van Enckevort and Ruessink (2001), Plant et al. (2007), and Ribas et al. (2010). Both breaker lines, hereafter referred to as barline and shoreline, were extracted with a semi-automatic algorithm that finds the cross-shore pixel intensity maximum for each alongshore position in the images (Pape et al., 2010). Some days no barline and/or shoreline could be detected due to camera failure, fog, or the lack of breaking waves during low-energetic conditions. Breaker lines shift onshore under an increased water level. Therefore, only low-tide images were considered, to reduce the tide-induced shifting of both breaker lines (Van Enckevort and Ruessink, 2001). In addition, the shoreline was translated to -0.68 m MSL, i.e. Mean Low Water (MLW), to remove wave- and tide-induced shifting (see *Appendix A*).

The sets of barlines $x_b(y, t)$ and shorelines $x_s(y, t)$ were filtered for lengths smaller than 750 m using a scale-controlled quadratic loess filter (Plant et al., 2002). The resulting two sets, $X_b(y, t)$ and $X_s(y, t)$, contain large length scales (the shape of the Sand Engine) and lack small length scales (perturbations in the sandbar and shoreline). Both $X_b(y, t)$ and $X_s(y, t)$ were subtracted from $x_b(y, t)$ and $x_s(y, t)$ and filtered for lengths smaller than those of our interest (i.e. <75 m), resulting in two sets that contain only the perturbations in the barline and shoreline $X'_b(y, t)$ and $X'_s(y, t)$.

Figure 3.4 shows that $X'_b(y, t)$ and $X'_s(y, t)$ varied in time from 2D (e.g. July 2013 between $y = 0$ m and $y = 2000$ m) to strongly 3D (e.g. December 2013 between $y = 0$ m and $y = 2000$ m), but they also varied alongshore. Perturbations at the western side did not necessarily arise or occur simultaneously at the northern side, see for example January 2015. Moreover, the length scale of the perturbations was different, note the alongshore differences in June 2013. To analyse the differences in sandbar and shoreline behaviour along the curved coastline of the Sand Engine, we divided the coast into two sides (north and west) that have an approximately straight coastline, and exhibit a similar development of patterns in Figure 3.4. Since the 3D patterns hardly migrated along the tip from the northern to the western side or vice versa (Figure 3.4), we treat the two sides as mutually independent in the analyses and interpretation of our results.

Hourly measurements of significant wave height H_s , peak wave period T_p and mean wave direction with respect to the north θ_N were obtained from two offshore stations: the Euro-platform (EUR) wave buoy, located in 32 m water depth at 63 km west of the field site, and the wave buoy at IJmuiden Munitiestortplaats (IJM), located in 21 m water depth 56 km north of the field site. Wave information was used from EUR for W-S waves ($\theta_N \leq 280^\circ$), 47% of the time, and from IJM for W-N waves ($\theta_N > 280^\circ$), 38% of the time. When no measurements were available for the preferred station (3%, 10% and 4% of the time for H_s , θ_N , and T_p respectively), wave information was used from the other station. No wave measurements were available at either of the stations for 15% of the time. For this study, offshore wave characteristics were transferred to wave characteristics at 10 m water depth, using a wave lookup table (<https://publicwiki.deltares.nl/display/BWN1/Tool+-+Wave+Transformation+Table>, accessed most recently in April 2018). Accordingly, for our 2.4-year study period the mean H_s reduced from 1.3 m to 0.97 m and the two directional modes changed from 222° to 258° and from 347° to 338° due to wave refraction.

3.2.3 Morphometric parameters

To quantify the sandbar and shoreline behaviour, three morphometric parameters were computed: alongshore-averaged position μ of $X(y, t)$, standard deviation σ of $X'(y, t)$ as a measure of three-dimensionality, and cross-correlation between $X'_b(y, t)$ and $X'_s(y, t)$ to quantify a potential morphological coupling (Van Enckevort and Wijnberg, 1999; Ruessink et al., 2007; Price and Ruessink, 2013; Van de Lageweg et al., 2013). Here, we computed the lagged cross-correlation r between two signals $x(n, t)$ and $y(n, t)$ as

$$r(m, t) = \frac{Cov_{xy}(m, t)}{\sqrt{Cov_{xx}(0, t)Cov_{yy}(0, t)}} \quad (3.1)$$

wherein $Cov_{xy}(m, t)$ is the covariance function of $x(n, t)$ shifted over spatial lag m and $y(n, t)$ at time t

$$Cov_{xy}(m, t) = \frac{1}{N - |m|} \sum_{n=0}^{N-m} (x_{n+m}(t) - \bar{x}(t))(y_n(t) - \bar{y}(t)) \quad (3.2)$$

with $n = 0 \dots N$, $m = -N+1 \dots N-1$, and $N+1$ the total number of points. r can vary between -1 or maximum negatively correlated, through 0 or uncorrelated to 1 or maximum positively correlated. In this study, an r towards 1 implies that $X'_b(y, t)$ and $X'_s(y, t)$ show exactly the same pattern, referred to as coupled in-phase, whereas an r towards -1 implies that patterns are exactly opposite, referred to as out-of-phase (Castelle et al., 2010). A maximum in r at positive lag m indicates that the correlated patterns in $X'_s(y, t)$ have an offset to the south (left

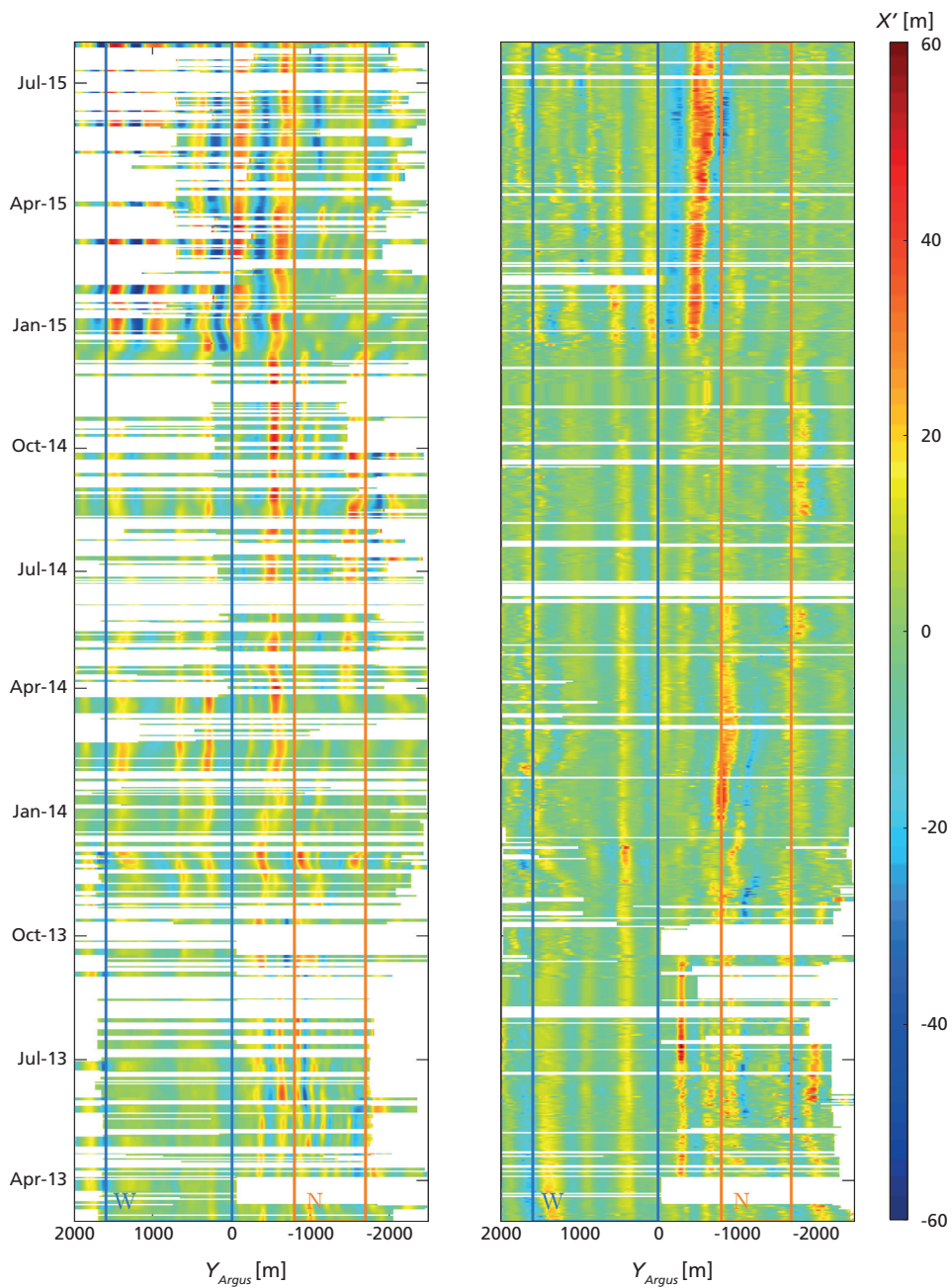


Figure 3.4: Timestack of perturbations in the barline X'_b (left) and Mean Low Water line X'_s (right). The boxes indicate how the study area was divided into a north (N) and west (W) side that were used for morphometric computations. Red (warm) and blue (cold) colours correspond to seaward and shoreward perturbations, respectively. White parts represent no data.

in the image) with respect to $X'_b(y, t)$, whereas a negative lag m denotes an offset to the north. The 98% confidence interval of significant cross-correlation was computed using the method of Garrett and Toulany (1981), following Price and Ruessink (2013).

For further analysis of morphological coupling, only barlines and shorelines were included that had a certain alongshore variability, $\sigma(X'_s) > 7$ m and $\sigma(X'_b) > 7$ m, following Price and Ruessink (2013).

3.2.4 Forcing parameters

To determine the wave conditions that govern the observed sandbar behaviour, three forcing parameters were computed: wave power, alongshore wave power and breaker wave height.

Wave power P was computed as

$$P = \frac{\rho g^2}{32\pi} H_{rms,10}^2 T_{p,10}, \quad (3.3)$$

with sea water density ρ of 1025 kg/m³, gravitational acceleration g of 9.81 m/s², root-mean-square wave height $H_{rms,10}$ and peak period $T_{p,10}$, both at 10 m water depth. Here, P , similar to the wave energy density flux Ec_g (with wave energy E and group velocity c_g), is a measure for the offshore wave energy imposed on the sandbar system. The alongshore wave power P_y , following Komar (1976) and Price and Ruessink (2011), was computed as

$$P_y = P \sin \theta_{10} \cos \theta_{10}, \quad (3.4)$$

with the wave angle at 10 m water depth θ_{10} . P_y , proportional to the radiation stress component S_{xy} , serves as measure for the intensity of the alongshore current. Breaker wave height H_b , following Komar (1976) and Splinter et al. (2011), was computed as

$$H_b = \left(\frac{0.42}{g} \right)^{1/5} \left(H_{rms,10}^2 c_{g,10} \frac{\cos \theta_{10}}{\cos \theta_b} \right)^{2/5}, \quad (3.5)$$

with group velocity at 10 m depth $c_{g,10}$, and wave angle at breaking θ_b .

Here, P_y and H_b were estimated for both the northern and western side, by taking θ_{10} with respect to the shore-normal at either side, where θ_b was assumed to be 0° for both sides. To account for the typical slow and delayed response of the morphology to changes in the wave forcing, smoothed time series were created of both P and P_y by averaging over the eight preceding days, following Quartel et al. (2008). Furthermore, for H_b the 2.4-year data set averages were computed to evaluate the averaged imposed wave energy at the northern and western side throughout the study period.

3.3 Results

3.3.1 Large-scale evolution

To illustrate how the large-scale morphology of the Sand Engine has evolved since the Sand Engine's construction in 2011, we first describe the development of the planshapes (Figure 3.5) and the cross-shore profiles (Figure 3.6), based on bed elevations measured *in situ* by jet-ski. Every 2-3 months data were collected along cross-shore transects separated by 80 m (refined to 40 m, shoreward of the -7 m contour). We refer to De Schipper et al. (2016),

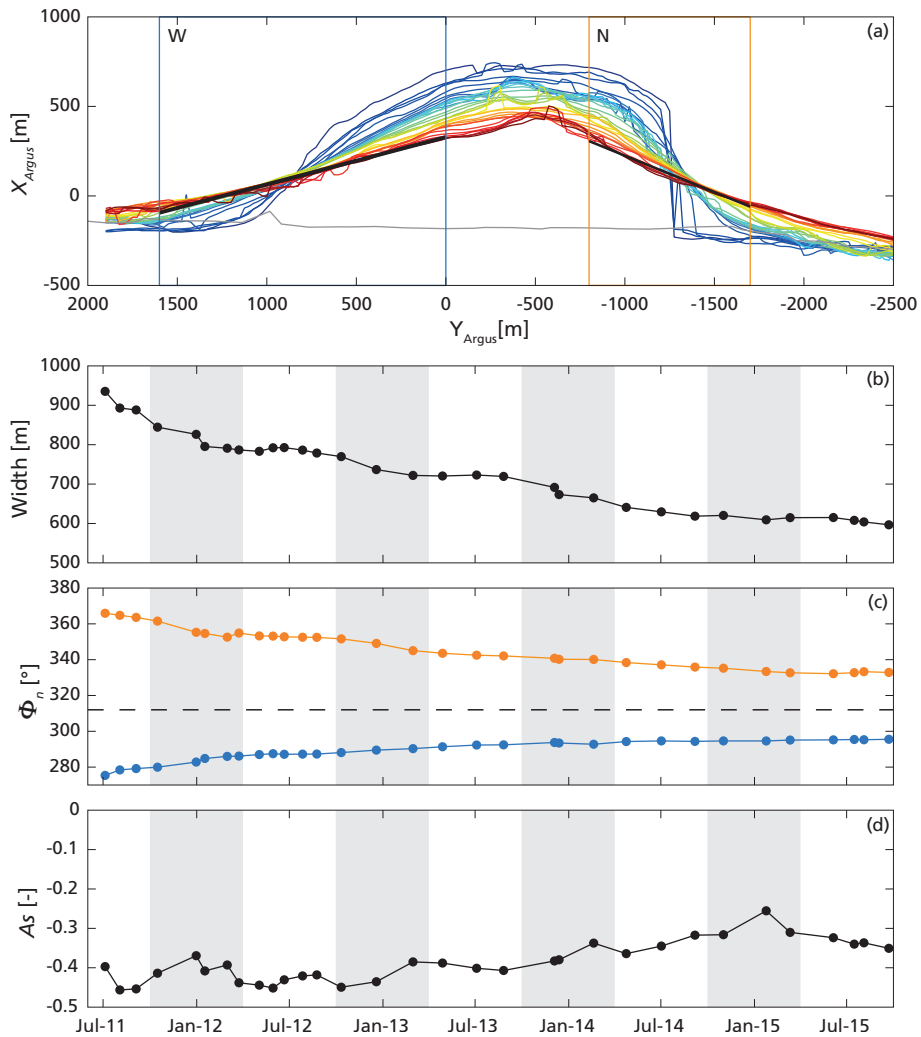


Figure 3.5: The gradual diffusion of the Sand Engine is illustrated by the (a) -1 m contours from August 2011 (blue) until July 2015 (red), (b) the maximum cross-shore extension of the -1 m contour with respect to the pre-nourishment situation, and (c) the orientation of the shore-normal Φ_n at the northern (orange) and western (blue) side. The black lines in (a) depict the linear fit performed on every contour at the northern and western side to estimate Φ_n . The jump in the first (i.e. blue) contour lines at $Y_{Argus} = -1300$ m is caused by the initially wide lagoon entrance of the Sand Engine. The black dashed line in (c) denotes an orientation of 312° similar to the pre-nourishment situation. The temporal evolution of the asymmetry A_s of the -1 m contour is shown in (d), where negative values reflect a contour that pitches northward and zero asymmetry reflects a symmetric plan shape. The grey shadings in (b), (c), and (d) indicate the winter months.

who focused only on the first year of the Sand Engine’s large-scale evolution, for details on the data collection.

The Sand Engine was constructed as a strongly curved protrusion of the natural coastline to stimulate the erosion and diffusion of the nourished sand to the adjacent beaches through

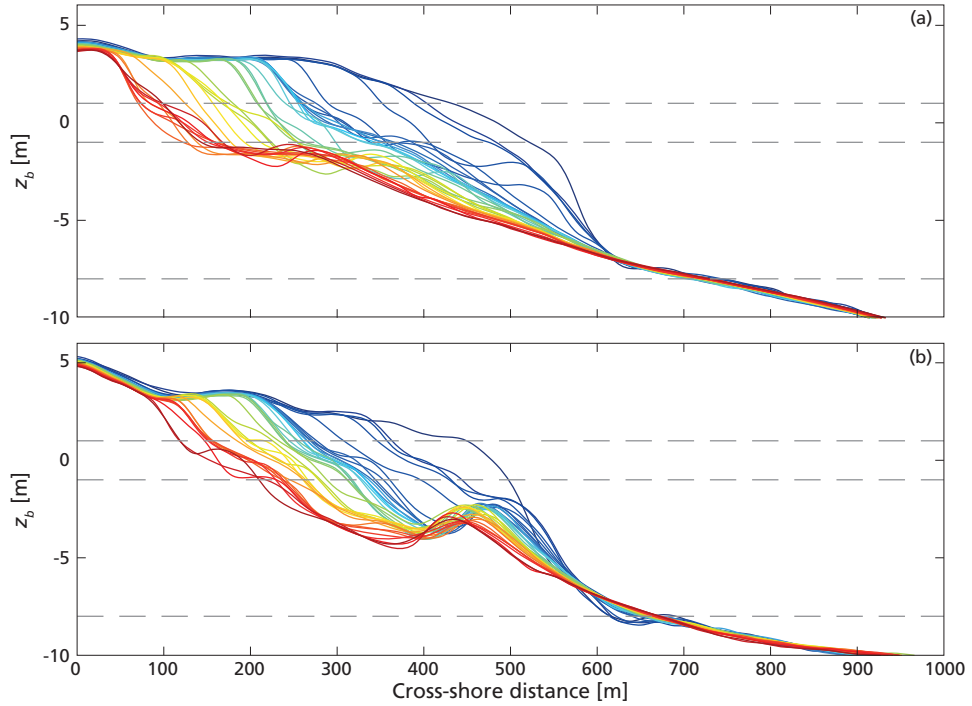


Figure 3.6: Cross-shore profiles of bed elevation z_b from July 2011 (blue) till June 2015 (red) at a location representative for the northern side (a) and the western side (b). The grey dashed lines indicate +1 m MSL, -1 m MSL, and -8 m MSL, used to estimate the cross-shore slope (see Figure 3.7). Profiles were extracted from *in situ* measurements, collected every 1-3 months (collection moments can be interpreted from the dots in Figure 3.5b-d).

wave, tidal and wind forces. Indeed, the nourishment itself lost 1.5 Mm^3 of sand within one year after completion, while the northeastern and southwestern adjacent coasts gained 0.7 Mm^3 and 0.5 Mm^3 , respectively (De Schipper et al., 2016). This diffusion (ongoing; for long-term predictions see Arriaga et al., 2017) can be explained by the gradients in net along-shore sand transport induced by the curved coast. Given the high longshore transport rates, a spit developed at the northern end of the nourishment where the coast was initially strongly curved, and it continued to grow towards the northward located beach (Figure 3.1). The diffusion of the Sand Engine is reflected in the decreasing curvature of the -1 m contour (Figure 3.5a), in the decreasing maximum cross-shore width of the nourishment (Figure 3.5b), as well as in the orientation of the -1 m contour, Φ , at the northern and western side. The two orientations, computed as the gradient of a linear fit through the -1 m contour over the northern and western side, respectively, seem to converge towards the pre-nourishment value of 42° from the North. The linear fit has a coefficient of determination R^2 of 0.82 at the northern side and 0.95 at the western side initially (July 2011); R^2 at the northern side increased rapidly beyond 0.95 in six months (July-December 2011). Figure 3.5c shows that the shore-normal, Φ_n , changed from 366° to 332° over the northern side and from 275° to 295° over the western side, converging towards the pre-nourishment orientation of 312° . Note that the increase in Φ_n reduced at the western side from winter 2013-2014 onwards, while it continued to decrease at the northern side. The different rates of change of the -1 m

contour at the northern and western side were also observed in the asymmetry of the plan shape, visualised in Figure 3.5d. Asymmetry was computed as $x^3/(x^2)^{1.5}$, where x was the imaginary part of the Hilbert transform on the -1 m contour. Here, a negative asymmetry denotes a northward-pitching -1 m contour, whereas a positive asymmetry indicates that the -1 m contour pitches to the south. Thus, the increase in asymmetry magnitude from -0.454 towards -0.3 from summer 2011 to summer 2014 reflects a change in plan-shape from northward pitching towards symmetrical. The largest changes were observed in autumn and winter (October-March), while the asymmetry hardly changed in spring and summer (March-October).

The Sand Engine was constructed with a convex, steep cross-shore profile, as shown in Figure 3.6. At both sides of the Sand Engine, the profile became concave within six months, due to fast erosion in the upper part of the profile ($z_b > -1$ m MSL). As a result, the subaqueous profile slope decreased. Figure 3.7 shows the temporal variation in profile slope, computed as the gradient of a linear fit through the alongshore-averaged cross-shore profile, at the northern and western side. In the first six months, the overall, subaqueous profile slope (between -1 m MSL and -8 m MSL) rapidly decreased, from 1:36 (0.028) to 1:50 (0.020) (Figure 3.7a) with fast erosion in the upper part of the profile (Figure 3.6). Thereafter, the slope continued to decrease, and started to converge to a cross-shore slope of 1:75 (0.013), which is slightly steeper than the pre-nourishment slope of 1:100 (0.010). The error bars, showing the standard deviation of the profile slope over both sides, indicate that the slope tended to become alongshore uniform with time. No significant difference was found between the profile response at the northern and western side. Similar to the slope of the overall profile, the intertidal slope showed an initial, rapid decrease to 1:49 (0.020) at the northern side and 1:56 (0.018) at the western side (Figure 3.7b). Thereafter, the slope became on average (January 2012-September 2015) steeper, 1:32 (0.034) at the northern side, but milder, 1:62 (0.016) at the western side. The intertidal profile, probably influenced by the subtidal sandbars, showed substantial alongshore variations in slope. Moreover, the northern side showed a seasonal fluctuation with a steeper profile of up to 1:19 (0.053) in early spring (April) and a milder profile of up to 1:58 (0.017) in late autumn (December). The profile became milder with the build-up of a low-tide terrace (Figure 3.6a) during calm conditions, but also with erosion of the upper part of the beach due to overwash of the spit during storms. With ongoing storm conditions the low-tide terrace moved slightly offshore to larger depths, resulting in a steepening of the intertidal profile. In more detail, the temporal evolution of the low-tide-terrace at the northern side and the classically Gaussian-shaped sandbar at the western side can be seen in Figure 3.6. Besides the difference in bar shape, note the differences in bar crest depth, 1.5 m versus 3 m, and cross-shore bar position, $x = 300$ m versus $x = 450$ m, between the northern and western side, respectively.

3.3.2 Sandbar and shoreline behaviour

Alongshore-uniform (2D) behaviour

Figure 3.8a shows that the sandbar was consistently located 125 m and 155 m from the initial MLW line at the northern and western side, respectively. Within 2.4 years, no net onshore or offshore migration can be observed, but $\mu(X_b)$ varied seasonally with offshore migration in winter and onshore migration in summer. In more detail, the sandbar started to migrate offshore with the first storm in autumn (September 2013 and October 2014; Figure 3.8f,h) and continued to do so until December/January, by up to 60 m at the northern side, and 35 m at the western side. Thereafter, $\mu(X_b)$ was either steady or decreased slowly during the summer months with low wave power. The observed offshore bar migration with winter storm waves

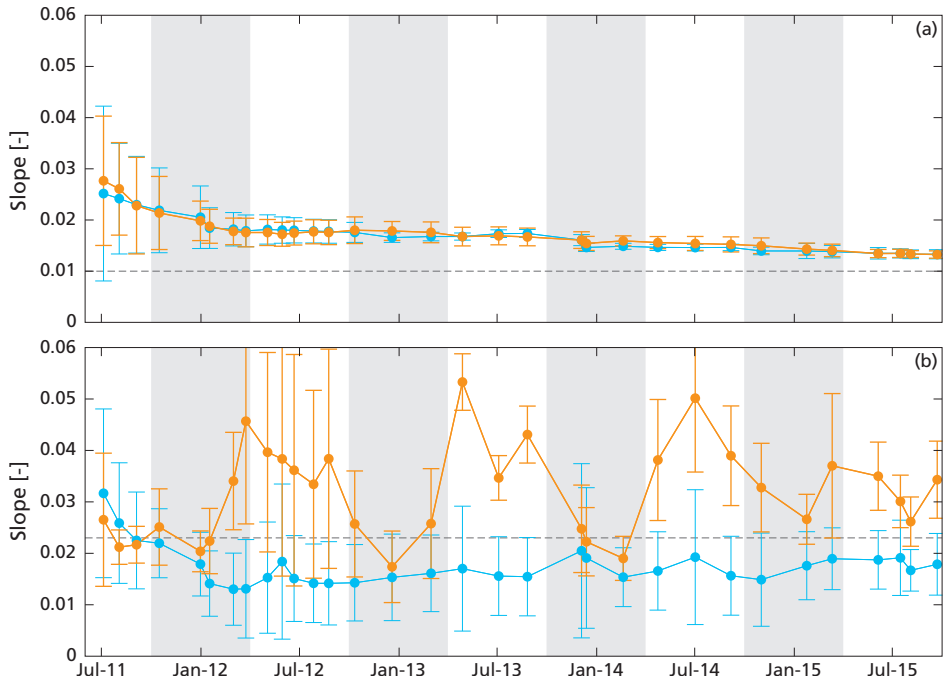


Figure 3.7: The cross-shore slope between (a) -1 MSL and -8 MSL, and (b) -1 MSL and $+1$ MSL, averaged alongshore at the northern (orange) and the western (blue) side. Error bars indicate the standard deviation in cross-shore slope at the northern and western side. The grey dashed line indicates the slope before construction of the Sand Engine. The grey shadings indicate the winter months.

and onshore bar migration with less-energetic summer waves is consistent with 2D bar migration elsewhere along the Dutch coast (Van Rijn et al., 2003; Ruessink et al., 2009; Pape et al., 2010). Minor fluctuations in $\mu(X_b)$ can be observed throughout the year, especially at the northern side, but a clear response to every individual storm (e.g., Figure 3.8f) is not discernible, possibly because of a rather large volume of sand constituting the bar compared to sites where a clear storm response was observed (Gallagher et al., 1998; Ruessink et al., 2009).

The seasonal migrational behaviour of the sandbars on both sides is also reflected in the water depth above the bar, d_c , computed from the *in situ* surveys (Figure 3.8e). Although the bar was located, on average, in shallower water at the northern side than at the western side, d_c of 2 m versus 2.5 m, both sides had larger d_c in winter, smaller d_c in summer and up to 1 m inter-seasonal variability.

Figure 3.8b shows that the distance between the sandbar and MLW line, $\Delta\mu(X)$, increased from 130 m at the northern side and 160 m at the western side in March 2013 to 190 m and 180 m in March 2015, respectively. The increase can be attributed to the net retreat in $\mu(X_s)$ during the study period (Figure 3.8a). In more detail, the retreat in $\mu(X_s)$ slowed down at the northern side and even halted at the western side, under low wave power between March and November 2014 (Figure 3.8h). During the following low-energetic spring and summer (from March 2015 onwards), $\mu(X_s)$ was again rather steady. A rapid retreat was

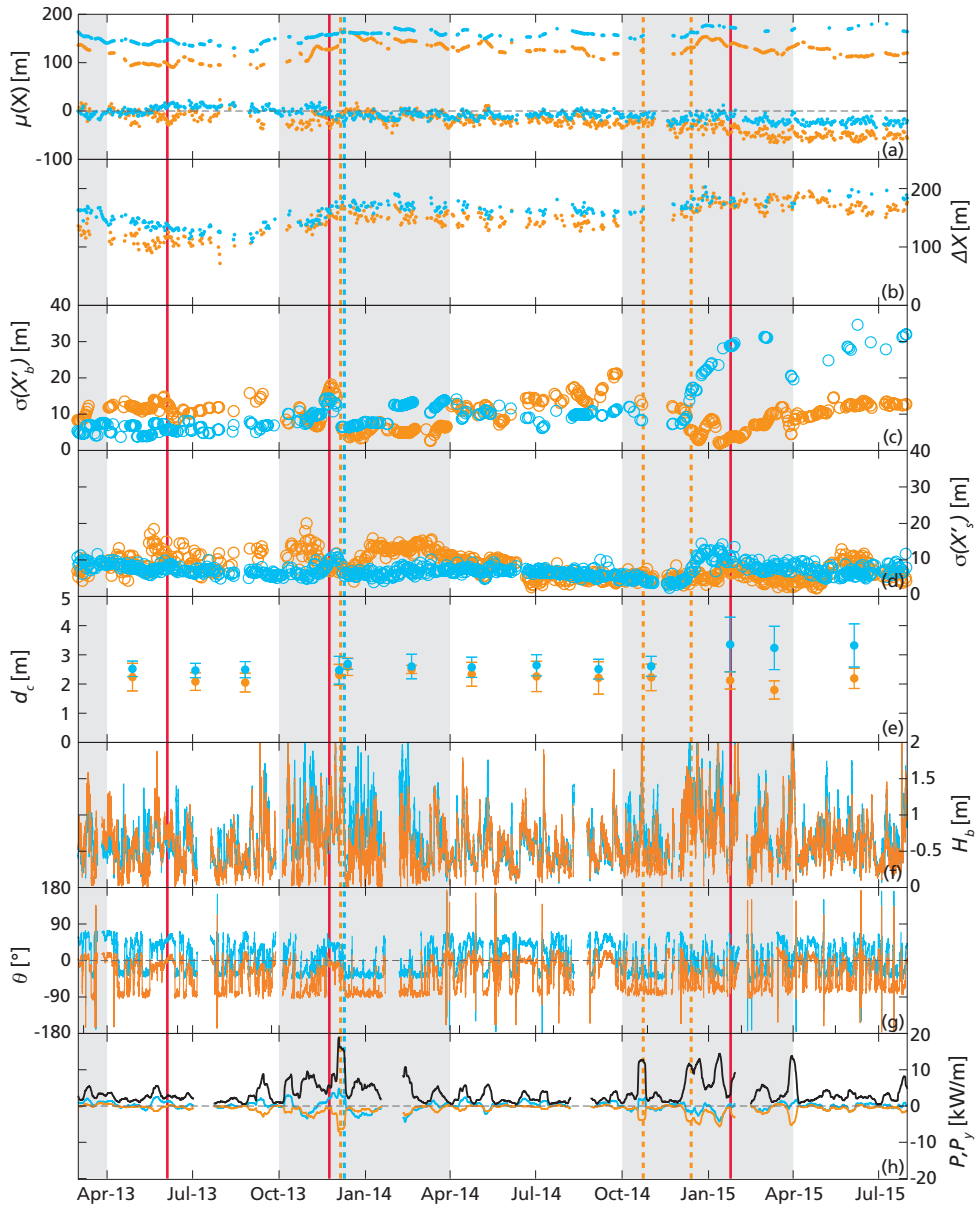


Figure 3.8: Time series of (a) alongshore-averaged position $\mu(X)$ of the sandbar and Mean Low Water line (-0.68 MSL) with zero $\mu(X)$ as the position of the MLW line in March 2013, (b) distance $\Delta\mu(X)$ between the sandbar and MLW (-0.68 m MSL), standard deviation in detrended (c) sandbar position $\sigma(X'_b)$ and (d) MLW position $\sigma(X'_s)$, (e) water depth above the sandbar crest d_c , (f) breaker height H_b , (g) wave angle θ and (h) the eight-day averaged wave power P (black) and alongshore wave power P_y at the northern (orange) and the western (blue) side. High values of $\sigma(X'_b)$ and $\sigma(X'_s)$ represent pronounced 3D patterning, whereas low values indicate a 2D barline and shoreline. The error bars in (e) indicate the standard deviation in d_c within each box; large error bars reflect a high alongshore variability in d_c . The grey shadings indicate the winter months, the vertical dashed lines the dates corresponding to sandbar straightening and the vertical red lines the dates of the example plan view images of Figure 3.1.

observed in November 2013 and February 2015. Before April 2013, no clear trends in $\mu(X_s)$ and accordingly $\Delta\mu(X)$ were observed (in *in situ* data, not shown), because the dynamics of the MLW line were dominated by spit formation at the northern side and accumulation in the intertidal and subtidal zone at the western end, as described in 3.3.1 (Figures 3.5 and 3.6).

Alongshore-variable (3D) behaviour

During the study period, three-dimensional (3D) patterns developed regularly in the sandbar at both the northern and the western side, as represented by the increase in $\sigma(X'_b)$ (measure for the horizontal amplitude of 3D patterns; Figure 3.8c) and the increase in the standard deviation of bar crest depth, $\sigma(d_c)$, (measure for the vertical amplitude of 3D patterns; error bars in Figure 3.8e). Typically, $\sigma(X'_b)$ increased up to ~ 20 m (with the exception of $\sigma(X'_b) = 30$ m at the western side). The temporal variability in $\sigma(X'_b)$ and $\sigma(d_c)$ indicates that 3D behaviour at the northern and western sides differed substantially. For example, $\sigma(X'_b)$ was up to 15 m at the northern side between April and October 2013 and decreased halfway November 2013, while at the western side $\sigma(X'_b)$ was only 9 m and increased to 12 m in the second half of November 2013. Figure 3.8 shows that $\sigma(d_c)$ varied with $\sigma(X'_b)$, i.e. the sandbars possessed an alongshore variability in both position and water depth. Note that the sandbar at the western side was highly 3D ($\sigma(X'_b)$ of 30 m and $\sigma(d_c)$ of 1 m) in January 2015. Generally, 3D patterns formed gradually at the northern side within several months in spring and summer when wave power was low (Figure 3.8h), and were partially or fully smoothed out (known as bar straightening) within a few days with high wave power in autumn (e.g. December 2013, October 2014, December 2014). Contrastingly, 3D patterns developed within days-weeks at the western side under a series of moderate storms in autumn, were hardly affected by the low-energetic spring and summer months, and were erased only once (synchronously timed with the northern side, under high wave power in December 2013). Similar to the 2D behaviour, the 3D behaviour also seems to be driven by a series of storms rather than every single storm event.

Video images further illustrate how the 3D patterns developed differently at each side. Figure 3.9a-f shows that the typical gradual increase in $\sigma(X'_b)$ at the northern side can be explained by the merging of small-scale (~ 200 m) patterns that formed under calm conditions into larger-scale (~ 400 m) undulations under moderate conditions, as observed earlier by Van Enckevort et al. (2004). Figure 3.9g-l shows the formation of large-scale (400-500 m) undulations in several days of moderate wave power, typical for the western side. Wavelengths at both sides were smaller than observed further to the north along the Holland coast (~ 1000 m, Van Enckevort and Ruessink, 2003b). Wavelengths were estimated through auto-correlation of the barlines. Although correlations were mostly not statistically significant for our data set, they gave an indication of the dominant wavelength, as found by Ruessink et al. (2007) who showed that wavelengths from auto-correlation, insignificant due to varying length scales along the barline, resembled the dominant lengths found with wavelet analysis. Figure 3.4 further illustrates that the wavelengths of 3D patterns were generally larger at the western side than at the northern side.

Three-dimensional patterns in MLW position were generally less pronounced and fluctuated less in time than 3D patterns in sandbar position (Figure 3.8c-d). Despite this, a few rapid increases in $\sigma(X'_s)$ were observed of 6 m to 11 m in typically 20 days. At the western side, a growth in $\sigma(X'_s)$ was accompanied by a growth in $\sigma(X'_b)$ (December 2013, December 2014). This correspondence was less clear at the northern side. Here, undulations could persist for months, reflected by the high, steady signal in $\sigma(X'_s)$ (e.g. January-March 2014). Decay of alongshore variability in the MLW line was either abrupt (December 2013) or grad-

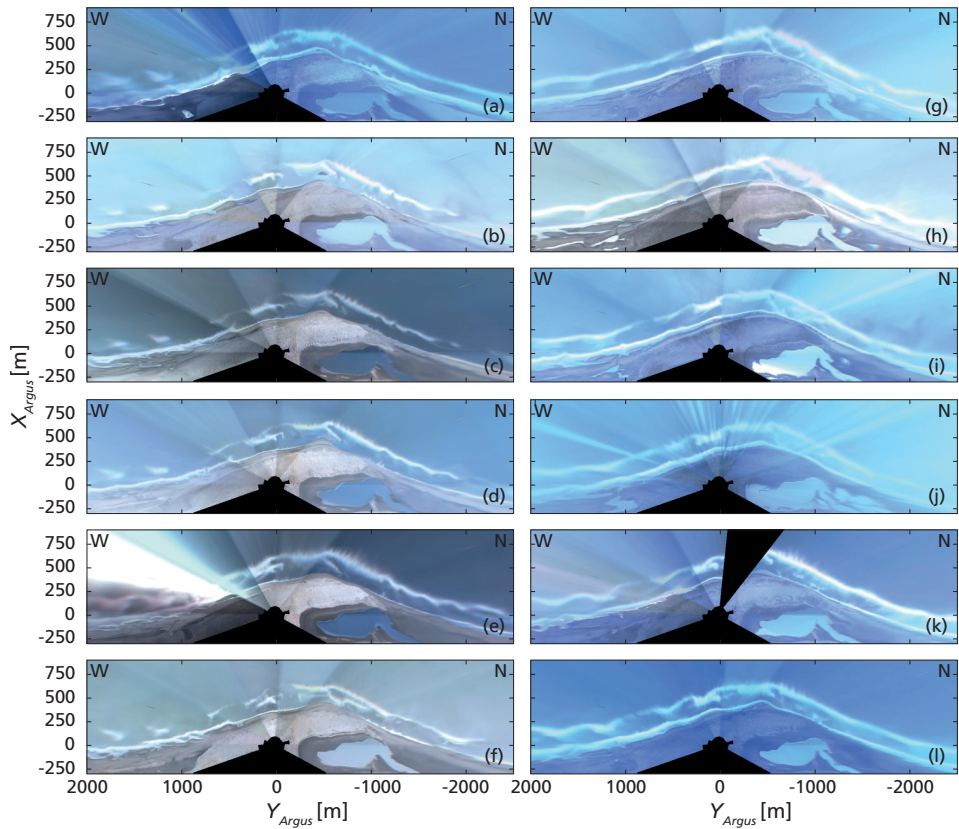


Figure 3.9: Argus ten-minute averaged planviews from (a) 14 January 2015, (b) 10 February 2015, (c) 22 February 2015, (d) 5 March 2015, (e) 27 March 2015, (f) 3 April 2015, (g) 3 December 2014, (h) 9 December 2014, (i) 13 December 2014, (j) 19 December 2014, (k) 29 December 2014, and (l) 2 January 2015, showing how 3D patterns developed in the sandbar at the (left column) northern side and (right column) western side.

ual (March-June 2014, January-May 2015). Similar to the sandbar, the timing of growth and decay of 3D patterns in the MLW line differed between the northern and western side (e.g. December 2014, January 2015).

Coupling

Figure 3.10 shows that morphological coupling between sandbar and shoreline was, at times, significant: 6.7% of all observations at the northern side and 7.8% at the western side, with a mean correlation coefficient R^2 of 0.57 and 0.48, respectively. For 49% of the observations at the northern side and 56% at the western side no cross-correlation could be computed, because at least one of the breaker lines was missing. Generally, sandbar and shoreline were uncorrelated at zero lag. However, a significant, positive correlation (in-phase coupling) was found at the northern side for 6.0% of the observations with a bimodal distributed lag, centred at $m = -30$ m and $m = 210$ m. At the western side, 4.6% of the observations had a positive correlation (in-phase coupling) with a bimodal lag centred at $m = -270$ m and $m = 90$ m, and 3.2% had a significant, negative correlation (out-of-phase coupling) with a

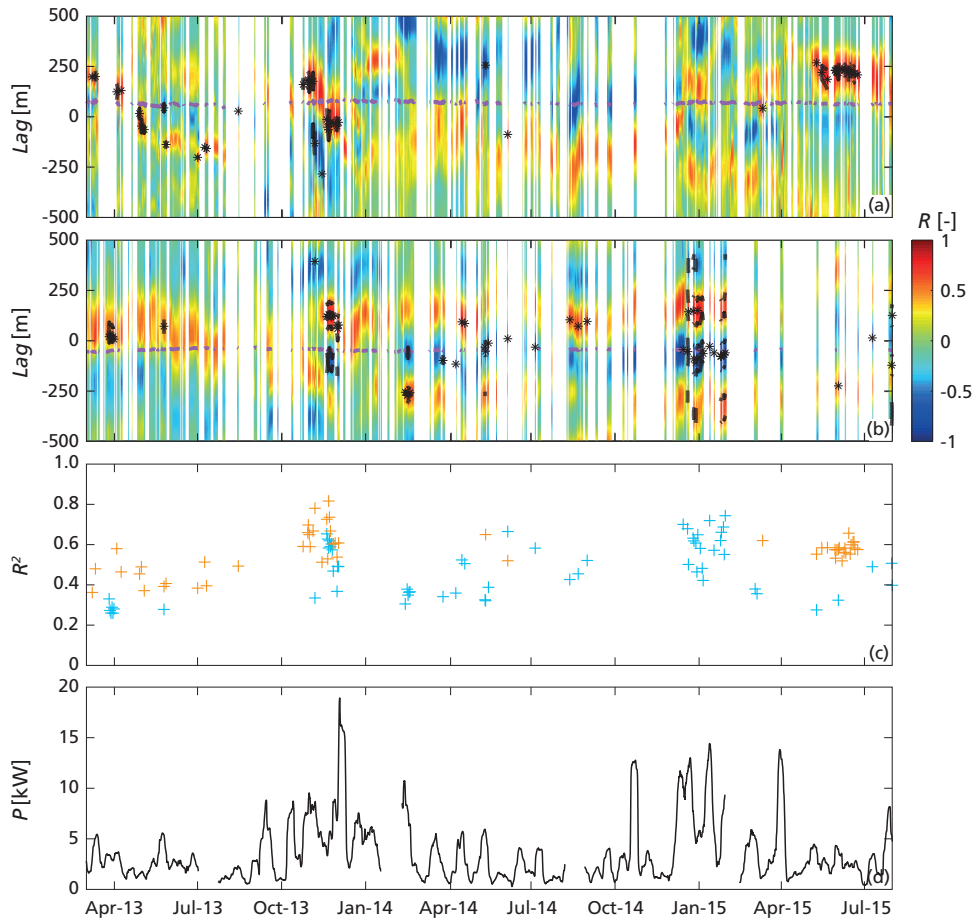


Figure 3.10: Lagged cross-correlation between the perturbations in the sandbar X_b^i and the Mean Low Water line X_w^i at the (a) northern side and at the (b) western side. Warm values indicate positive cross-correlation implying in-phase coupling, whereas cold colours represent negative coupling that can be interpreted as out-of-phase coupling. The black contours indicate the 98% significance level. The purple lines in (a) and (b) show the zero-lag that is corrected for the coastline orientation and the distance between the barline and shoreline at both sides. The squared correlation coefficient R^2 is plotted in (c) when significant at the 98% confidence level. For reference, the eight-day averaged wave power P is shown in (d).

lag of $m = -90$ m. Given that the coordinate system was not aligned with the coastline, a positive correlation with either a small negative lag (or large positive lag) at the northern side or a small positive lag (or large negative) at the western side represents an unshifted out-of-phase coupling for the local coastline orientation. Similarly, negative correlations can be interpreted as a locally unshifted out-of-phase coupling, for small positive lag at the northern side and small negative lag at the western side. Note that the lag of significant correlation decreased with a smaller distance between sandbar and shoreline and with smaller plan shape curvature. To summarise, the modal lags computed here seem to apply to an unshifted out-of-phase coupled sandbar and shoreline, considering the local coastline orien-

tation. The 'zero-lag' for the local coastline orientation (purple line in Figure 3.10), estimated from $\Delta\mu(X)$ and Φ , confirms that the sandbar and shoreline were generally coupled out-of-phase (e.g. see western side in Figure 3.1c) as observed elsewhere (Thornton et al., 2007; Van de Lageweg et al., 2013; Castelle et al., 2015). A minor temporal variation exists in the lag of significant coupling, of up to ~ 80 m (Figure 3.10a-b, e.g. January 2015), but is small compared to the wavelength of the 3D patterns (200-500 m). Coupling patterns were strongest at the western side from December 2014 till July 2015, when also 3D patterns were most pronounced. Sandbar and shoreline did not couple and decouple synchronously at the two sides (e.g. December 2014, see Figure 3.10a-c).

3.4 Discussion

In this section, we analyse the wave conditions to determine what forcing parameters governed the observed sandbar behaviour and drove to the distinct differences in morphology at the northern and western side of the curved coast. In particular, we focus on breaker height and wave angle.

3.4.1 Breaker height

The northern and western sides differed in their typical surf zone morphology, apparent from the bar shape, the distance between sandbar and shoreline, and the wavelength of 3D patterns. These morphologic characteristics are probably related to each other (e.g. Calvete et al., 2005) and are thus not statistically independent. The low-tide terrace at the northern side, typically closely located to or connected to the beach with relatively small (~ 200 m) length scales of 3D patterns, suggests an exposure to moderate energetic wave conditions only (Wright and Short, 1984). In contrast, the pronounced Gaussian-shaped sandbar at the western side, which was typically positioned ~ 200 m offshore in ~ 2.7 m water depth, having 3D patterns with length scales of 400-500 m, is indicative of more energetic conditions.

During our 2.4-year study period, waves came predominantly from the north-north-west and the west (bimodal climate; Figure 3.11), consistent with the above-mentioned long-term wave climate characteristics. Figure 3.11 shows that wave heights were of equal magnitude for both directional modes, given that wave refraction effects were neglected. Wave height, however, decreases with refraction, which at the Sand Engine is especially important for highly oblique westerly waves approaching the northern side. To illustrate that the northern side was exposed to less energetic conditions than the western side, including refraction effects, the breaker wave height H_b was computed over the 2.4-year study period. Both the 50th percentile (median) as well as the 90th percentile of H_b were lower at the northern side compared to the western side: 0.53 m versus 0.59 m and 1.0 m versus 1.2 m, respectively. Figure 3.8f shows as well that H_b , varying with the local wave angle (Figure 3.8g), was generally higher at the western side. On the whole, our results indicate that alongshore variability in sandbar characteristics were related to alongshore variability in wave height imposed by the curved shape of the Sand Engine.

3.4.2 Wave angle

The sandbars at the northern and western sides responded differently to the same offshore time-varying wave forcing (Figure 3.8). Differences in 2D behaviour concerned the cross-shore migration rates of the sandbars (e.g. December 2014, Figure 3.8) and the shortest timescales over which the bars migrated (seasonal versus intra-seasonal). Differences in 3D behaviour mainly concerned the wavelength of the 3D patterns, and timing in their develop-

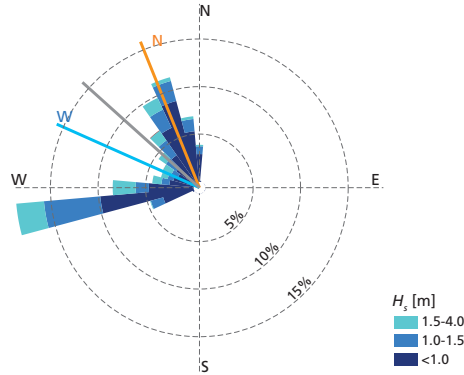


Figure 3.11: Wave conditions at 10 m water depth during the study period (March 2013-July 2015). The radial lines indicate the shore-normal before construction of the Sand Engine (grey), and time-averaged over the study period for the northern side (orange) and the western side (blue).

ment, even resulting in opposite behaviour at the northern and western side (e.g. December 2014: growth versus decay of 3D patterns, Figure 3.8). Similarly, a timing difference in morphological coupling was observed between both sides. The timing differences in 3D sandbar response and morphological coupling between both sides may be explained by the local wave angle. Figure 3.11 shows that most waves, as a result of the coastline curvature, approached either shore-normally or very obliquely ($\sim 80^\circ$) at the northern side, while predominantly obliquely (~ 36 and $\sim 44^\circ$) at the western side. For reference, waves entered predominantly obliquely (~ 54 and $\sim 26^\circ$) before construction of the Sand Engine. At the northern side, the growth of 3D patterns in the sandbar (Figure 3.8c) coincided with prolonged periods of near-zero wave incidence and moderate wave height ($H_b = 1.0$ - 1.5 m, e.g. March 2013, April-October 2014, Figure 3.8f-g), consistent with Wright and Short (1984), Calvete et al. (2005), Drønen and Deigaard (2007) and Splinter et al. (2011), all of whom showed that 3D patterns in sandbars form preferably under low-energetic, shore-normal waves. At the western side, contrastingly, 3D patterns formed rapidly with the passage of several storms, characterised by a shifting wave angle $\theta_W = -30$ to 40° and peaks in H_b of 1.5 - 2 m. Such behaviour, with increasing 3D patterning in the storm season, is similar to the 3D behaviour observed at Vlugtenburg, a few kilometers south of our study site (De Schipper et al., 2013). We find that sandbar straightening events at both the northern (December 2013, October 2014 and December 2014) and western side (December 2013) coincided with peaks of 4 - 6 kW/m in the eight-day averaged longshore wave power P_y (Figure 3.8h), suggesting that oblique waves of substantial height over 1 - 2 days, presumably driving a strong longshore current, were needed to erase the 3D patterns. The infrequent bar straightening at the western side may be explained by the generally small peaks in P_y . Similarly, we expect that the highly 3D bar in January 2015 would require higher P_y to straighten. The asynchronous response for the northern and western side, e.g. in December 2014 with bar straightening at the northern side versus a growth of 3D patterns at the western side, may be related to local differences in P_y , which, accordingly, is the consequence of the coastline orientation. Similarly, timing differences in coupling between sandbar and shoreline patterns, related to timing differences in 3D patterning, may also depend on the wave angle. Although, generally, cross-correlations were significant when the 3D patterns in the sandbar were pronounced (Figure 3.10; April-August 2013, November 2013 and May-June 2015 for the northern side; November 2013 and

December 2014-July 2015 for the western side), no significant cross-correlation was found at the northern side in summer 2014, when the bar was 3D. Possibly, the absence of a distinct bar trough or the limited distance between sandbar and shoreline (Figure 3.6; Wright and Short, 1984) may explain the lack of coupling due to a presumably weakened cell circulation. Castelle et al. (2010) showed for a double sandbar system how alongshore differences in wave breaking over a 3D outer bar generate such horizontal circulation cells that drive bed level changes shoreward of the bar, creating a coupled patterning in the inner bar.

Our observation that the wave angle determines to a large extent the 3D behaviour at the curved Sand Engine is in line with previous studies on straight coasts. For example, Thornton et al. (2007) and Price and Ruessink (2011) found that 3D patterns developed under near-normal waves, and Price and Ruessink (2011), Price and Ruessink (2013), Garnier et al. (2013) and Contardo and Symonds (2015) found that bar straightening and decoupling related to oblique waves. According to model predictions (Ashton et al., 2001; Thiébot et al., 2012) patterns in the shoreline and adjacent depth contours can also be related to highly oblique angles. Thiébot et al. (2012) showed that down-current oblique bars developed with an alongshore spacing of ~ 100 m along the inner bar of a double bar system for $21 < \theta < 31^\circ$ at the outer bar crest (~ 3.5 m depth). We are not aware of any field evidence on such pattern formation, but bar geometries seem similar to the erosional Transverse Bar and Rip state observed along the Gold Coast, Australia (Price and Ruessink, 2011) or the skewed Transverse Bar and Rip state along the Aquitaine coast, France (Castelle et al., 2007). Note, however, that their formation mechanism is different, as they are more likely to be re-oriented pre-existing morphological patterns. Thiébot et al. (2012) furthermore demonstrated that up-current elongated features developed when increasing the wave angle beyond 31° at the outer bar crest, with alongshore wavelengths of ~ 70 m extending hundreds of meters offshore. Those so-called finger bars have been regularly observed in the field, i.e. Duck, U.S.A (Konicki and Holman, 2000), Noordwijk, The Netherlands (Ribas and Kroon, 2007), and the Gold Coast, Australia (Ribas et al., 2014). At the Sand Engine, both oblique bars and finger bars have been observed occasionally (Figure 3.12), especially at the northern side where the westerly mode was highly oblique (Figure 3.11). Patterns simulated by Ashton et al. (2001), also referred to as shoreline sand waves, are related to gradients in the alongshore sediment transport that destabilise the shoreline and adjacent bathymetric contours (Ashton and Murray, 2006). Ashton and Giosan (2011) showed that shoreline patterns developed along one of the two flanks of an arcuate-shaped river delta under highly oblique waves. Although patterns seem similar to the shoreline undulations at our site, length and formation timescales of these shoreline sand waves are typically larger, 1-10 km versus 200-500 m and $O(100)$ years versus several months. Moreover, Arriaga et al. (2017) showed that the Sand Engine is just below the instability threshold and thus, on the long-term, will not grow by itself or trigger instabilities at the adjacent straight coastline.

Although high-angle waves may have played a role at the Sand Engine in generating 3D patterns, given the occasional presence of oblique transverse bars and finger bars, we attribute the variability in $\sigma(X')$, representing the patterning in sandbar and shoreline, largely to low-angle waves. First, oblique bars and finger bars were relatively rarely observed and thus they hardly contributed to $\sigma(X')$. Oblique bars hardly affected the barline, but only the shoreline (see Figure 3.12). No variability due to finger bars is included in $\sigma(X')$, since extracted breaker lines were filtered for length scales shorter than 75 m. Second, shoreline patterns in our observations arose in particular when sandbar patterns were already pronounced, and thus seem, in contrast to shoreline sand waves, to be related to surf zone circulation with the sandbar acting as a morphologic template. This is confirmed by Figure 3.10, showing sig-

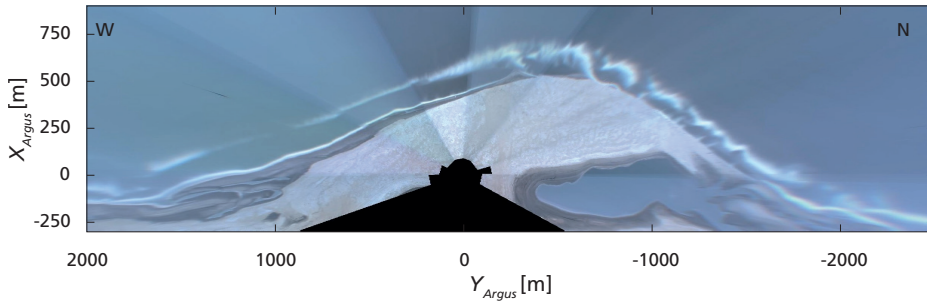


Figure 3.12: Argus time-exposure image from 4 April 2013, showing the presence of finger bars (white elongated features attached to the shoreline and pointing offshore) at $-1300 < Y_{Argus} < -1000$ m and oblique transverse bars at $-700 < Y_{Argus} < -300$ m.

nificant coupling between sandbar and shoreline patterns when the sandbar was 3D. Therefore, the mechanism on pattern formation along a curved coast, as proposed by Ashton and Giosan (2011), is not applicable here to the variability in $\sigma(X')$.

Although our data set covers 2.5 years only, which is relatively short with respect to the Sand Engine's expected lifetime of several decades (Arriaga et al., 2017), the duration is of sufficient length to raise the hypothesis that the wave height and angle are key to the observed alongshore differences in bar behaviour at daily to seasonal timescales. We expect that differences in bar behaviour between both sides may decrease in time, given the decrease in curvature under foreseen ongoing diffusion (Arriaga et al., 2017) with orientations of both sides becoming more similar. Herein, the sandbars may respond differently than expected given the previous history of both sides. For example, Tiessen et al. (2011) showed that differences in pre-existing bed forms may affect the wavelength of subsequently evolving crescentic patterns. Also, the northern and western sides may start to influence each other in time, and thus being no longer independent in their morphologic evolution. Our work implies that bar behaviour along curved coasts, e.g. shoreline sand waves, cusped forelands or embayed beaches, may show substantial alongshore variation wherein local wave forcing, i.e. wave height or wave angle, is important. To assess more closely how wave angle, wave height, or coastline curvature control bar behaviour along a curved coast, we will use a morphodynamic model in a future study. This will allow us to systematically test and analyse the individual effects of wave angle, wave height and curvature. In addition, by varying the coastline curvature, we can mimic the non-stationarity of curved coasts (e.g. the diffusion of the Sand Engine shown here). Also, the simulations will reveal the sediment transport patterns and underlying flow field that drive the distinct morphologic changes.

3.5 Conclusions

Along the man-made curved coast of the Sand Engine, both similarities and differences in sandbar and shoreline behaviour were observed. Similarities in 2D bar behaviour between the northern and western side include the onshore and offshore bar migration coinciding with the seasonally varying wave power, balancing to nearly zero migration on inter-annual timescales. Also, the distance between sandbar and shoreline increased in time at both sides, given the ongoing shoreline retreat related to the diffusion of the Sand Engine, and the rather

steady position of the sandbars on inter-annual timescales. The differences in bar geometry between both sides (3D length scales, distance from the shoreline, bar crest depth, and bar shape) suggest that the northern side was governed by lower energetic conditions than the western side, which was confirmed by H_b (1.0 m versus 1.2 m for the 90th percentile), locally different due to longshore differences in wave refraction.

Three-dimensional behaviour, i.e. growth, straightening, and coupling of 3D patterns in the sandbar and shoreline, differed between both sides, especially in timing. Whereas 3D patterns formed gradually in summer under prolonged periods of north-northwestern, moderate, shore-normal waves ($\theta_N = 0^\circ$, $H_b = 1-1.5$ m) at the northern side, they developed rapidly (days-weeks) under a series of southwestern-western autumn storms ($\theta_W = -30$ to 40° , $H_b = 1.5-2$ m) at the western side. The 3D patterns decayed under highly oblique waves when the eight-day averaged longshore wave power peaked ($P_y > 4$ kW/m). This happened more often on the northern than western side. A coupled sandbar and shoreline were mostly found in periods when 3D patterns were pronounced. Our findings on 3D behaviour suggest that the local difference in wave angle, imposed by the curved coast, explains the observed timing differences in 3D behaviour.

Although further study is needed to unravel the exact physical processes driving the intriguing differences in sandbar and shoreline behaviour along a curved coast, we conclude that such a coast imposes locally different wave conditions, in terms of wave height and wave angle, that, in turn, lead to substantial alongshore differences in subtidal sandbar dynamics.

Acknowledgements

J.R. and B.G.R. were funded by the Dutch Technology Foundation STW that is part of the Dutch Organisation for Scientific Research (NWO), and which is partly funded by the Ministry of Economic Affairs, under contract 12686 (Nature Coast: S1 Coastal Safety). T.D.P. was funded by the Dutch Organisation for Scientific Research (NWO), under contract 016.Veni.171.101. We acknowledge Deltares for the collection of the Argus imagery, and SHORE Monitoring & Research for the collection of the bathymetric data.

Chapter 4

Simulating crescentic sandbar behaviour along a curved coast

Based on: Rutten, J., B. Dubarbier, T.D. Price, B.G. Ruessink, and B. Castelle. Simulating crescentic sandbar behaviour along a curved coast. *Submitted to Journal of Geophysical Research: Earth Surface*.

Abstract

Sandbars, submerged ridges of sand parallel to the shoreline, tend to develop crescentic patterns while migrating onshore. At straight coasts, these patterns form preferably under near-normal waves through the generation of circulation cells in the flow field, whereas they decay under energetic oblique waves with associated intense alongshore currents. Recently, observations at a man-made convex curved coast showed an alongshore variability in patterning that seems related to a spatiotemporal variability of the local wave angle. Here, we aim to systematically explore how a curved coast, through local differences in wave angle and the resulting flow field, contributes to alongshore variability in crescentic pattern formation. A non-linear morphodynamic model was used to simulate the patterns in an initially alongshore uniform sandbar that migrates onshore along the imposed curved coast. Simulations show that the alongshore positioning and growth rate of patterns vary with the local breaker angle, depending on the schematisation of the offshore angle and the local coastline orientation. Growth rates decrease with increasing obliquity as both refraction-induced reductions of the wave height as well as alongshore currents increase. Furthermore, simulations of variations in coastline curvature show that patterns may develop faster at strongly curved coasts, given a wave climate with low obliquity. This implies that beaches where the coastline orientation changes substantially, e.g. due to km-scale nourishments, become potentially more dangerous to swimmers due to strong currents that develop with pronounced bar patterns.

4.1 Introduction

Sandbars, submerged ridges of sand parallel to the shoreline, often possess a pronounced alongshore variability in cross-shore position and depth (Sonu, 1973; Lippmann and Holman, 1989; Van Enckevort et al., 2004) that is related to the imposed wave energy, grain size and profile characteristics (Wright and Short, 1984; Calvete et al., 2007). These crescentic patterns are characterised by shallow landward protruding horns and deep seaward protruding bays with alongshore wavelengths of $O(100\text{ m})$ and cross-shore amplitudes of $O(10\text{ m})$ (Van Enckevort et al., 2004). Field observations show that crescentic patterns typically arise in a few days under low to moderately energetic conditions following a storm, and tend to disappear under high-energetic conditions (Wright and Short, 1984; Almar et al., 2010) or under oblique wave incidence (Price and Ruessink, 2011; Contardo and Symonds, 2015). In

some cases they may, however, persist for months or longer (Van Enckevort and Ruessink, 2003b). Pattern formation and destruction often coincides with overall onshore and offshore sandbar migration, respectively.

The mechanism behind crescentic pattern formation includes horizontal circulation cells in the flow field, which preferably develop under shore-normal or near-normal waves (e.g. Falqués et al., 2000; Calvete et al., 2005; Thiébot et al., 2012). Through a positive feedback between flow and morphology the characteristic crescentic patterning arises in the sandbar. Under increasing angles of incidence, circulation cells become skewed, growth rates decrease and wavelengths of the crescents increase (Calvete et al., 2005). In line with observations in the field, Thiébot et al. (2012) demonstrated with model simulations that crescentic patterns no longer arise when waves approach sufficiently oblique ($\theta > 11^\circ$ at their outer bar crest at ~ 3.5 m depth, where θ is the wave incidence angle with the shore-normal) and the breaking-induced alongshore current starts to dominate over cell circulation.

So far, the main focus has been on pattern formation under an alongshore uniform forcing. However, coasts that are concave, like embayed beaches, or convex, such as shoreline sandwaves and km-scale nourishments, impose an alongshore variation in forcing in the surf zone due to the refraction pattern over the curved depth contours (e.g. Castle and Coco 2012; Rutten et al. 2018). Similarly, offshore perturbations can create an alongshore variation in forcing (e.g. offshore bathymetric anomaly or offshore island; Castle et al., 2012; Bryan et al., 2013) and accordingly, in bar behaviour. For example, the breaker height may vary alongshore, which was suggested by Short (1978) to generate an alongshore variation in sandbar characteristics. Also, the wave angle may vary alongshore, and enforce an alongshore difference in crescentic patterning. Such a relation between angle and patterning was found on a seasonal scale along the man-made curved coast of the Sand Engine, located at the roughly southwest-northeast oriented coastline of the Delfland coast in the Netherlands (Figure 4.1). Prolonged low-energetic north-northwestern waves in the spring-summer season (Rutten et al., 2018) initiated the formation of patterns only at the northern side of the Sand Engine. Under these conditions no patterns formed along the western side, where the waves were presumably much more oblique. In the autumn-winter season, patterning at the northern side was erased, whereas patterns developed at the western side under storms passing from southwest to north-northwest. Thus, patterns developed at the western side when actual shore-normal wave exposure was limited due to the varying angle. Castle and Ruessink (2011) simulated the effect of a time-varying wave angle on crescentic patterns along a straight coast. Here, time-varying angles with low obliquity ($\theta < 6^\circ$, at 10.6 m water depth) resulted in crescents that were less pronounced than under time-invariant forcing, and moreover initiated an alongshore migration of the crescents that stimulated splitting and merging of the crescents. Time-varying angles including higher obliquity ($\theta > 6^\circ$), for at least 1 day, resulted in straightening of crescents by a strong alongshore current. Notwithstanding, how a spatiotemporal variation in wave angle, as occurring along a curved coast, contributes to pattern formation and destruction is yet unknown.

We hypothesise that a spatiotemporal variation in the local wave angle enforces an alongshore variation in the positioning and growth rate of crescentic patterns, depending on the strength of the alongshore current. In this chapter, we aim to systematically explore how a convex curved coast, loosely based on the Sand Engine, contributes to alongshore variability in the formation of crescentic bar patterns under time-varying forcing. We use the non-linear morphodynamic model of Dubarbarier et al. (2017), wherein cross-shore and alongshore processes are included such that an initially alongshore-uniform bar can move onshore and develop alongshore variabilities simultaneously. First, we outline the model, its setup and



Figure 4.1: Aerial picture of the Sand Engine in September 2014, looking in northeasterly direction. This km-scale nourishment, with 21.5 Mm³ larger than regular nourishments (1-2 Mm³), was constructed in July 2011 along the southwest-northeast oriented Delfland coast, The Netherlands, as sustainable and nature-based protection measure against coastal erosion (Stive et al., 2013). The nourished sand is aimed to gradually spread along the coast over several kilometers and into the dunes over a >20-year period, through the tides, waves and wind. Bathymetric measurements of the initial 1.5 years of the Sand Engine's evolution (De Schipper et al., 2016) are in line with numerical model predictions, showing erosion at the centre of the Sand Engine and accretion at its adjacent beaches. Courtesy: Rijkswaterstaat, Joop van der Hout.

the analysis of model results (Section 4.2). Then, we describe the effect of the offshore wave angle on pattern formation (Section 4.3). In Section 4.4, we discuss variations in wave characteristics and coastline curvature. Finally, we conclude our findings in Section 4.5.

4.2 Methodology

4.2.1 Model

The growth of crescentic patterns in sandbars and their evolution was simulated with a non-linear morphodynamic model consisting of four coupled modules (Dubarbier et al., 2017). In the first module, the statistical wave field was computed by the spectral wave model SWAN (version 41.10; Booij et al., 1999), wherein we chose the dissipation formulation of Ruessink et al. (2003) and switched off the triplet and quadruplet wave-interaction source terms. In the second module, the 2D flow field was computed via the phase-averaged and depth-averaged non-linear shallow water equations, assuming balance of momentum and conservation of water mass, giving (Phillips, 1977):

$$\frac{\partial Q_i}{\partial t} + \frac{\partial}{\partial x_j} \left(\frac{Q_i Q_j}{h} \right) = -gh \frac{\partial \eta}{\partial x_i} - \frac{1}{\rho} \frac{\partial S_{ij}}{\partial x_j} + \frac{1}{\rho} \frac{\partial T_{ij}}{\partial x_j} + \frac{\tau_i^b}{\rho} = 0, (i, j = 1, 2) \quad (4.1)$$

$$\frac{\partial \eta}{\partial t} = - \frac{\partial Q_j}{\partial x_j} \quad (4.2)$$

Using the Einstein convention, subscript i refers here to the two horizontal coordinates (X and Y). This implies that terms containing an index twice include a summation over all indices. In these equations, Q_i and Q_j are fluid volume transports, η is the mean free surface elevation, S_{ij} is the radiation stress tensor, T_{ij} is the lateral mixing term that describes the horizontal momentum exchange due to breaking-induced turbulence and the mean current, τ_i^b is bed shear stress, t is time, x is distance, h is water depth, g is gravitational acceleration, and $\rho = 1000 \text{ kg m}^{-3}$ water density. The wave return flow (undertow) was taken into account through the wave radiation stress formulation of Phillips (1977). In the third module, the total volumetric sediment transport \vec{q}_t was computed with an energetics-type transport model composed of three modes of transport, based on Hsu et al. (2006) and Dubarbier et al. (2015), as

$$\vec{q}_t = \vec{q}_w + \vec{q}_c + \vec{q}_g \quad (4.3)$$

with transport related to near-bed orbital velocity skewness \vec{q}_w , transport related to the mean current \vec{q}_c , and a diffusion term \vec{q}_g representing the downslope gravitational transport that prevents unrealistic bar growth and/or instable bar shapes. More specifically, \vec{q}_w accounts for wave non-linearity, but does not include infragravity or swash motions. Hereto, the intra-wave motion is reproduced using the robust parameterisation of Ruessink et al. (2012) that relates values of wave-skewness and asymmetry to the local Ursell number, all derived from field measurements of the statistical wave field and mean water level. The sediment transports \vec{q}_w , \vec{q}_c , and \vec{q}_g contain both bedload and suspended load, with scaling coefficients of 0.135 and 0.015, respectively. The contribution of the three individual transport components to \vec{q}_t is scaled with coefficients C_w , C_c , and C_g of 0.08, 0.08 and 0.24, respectively. For the specific definition of \vec{q}_w , \vec{q}_c , and \vec{q}_g , see Dubarbier et al. (2017). In the fourth module, bed level change was computed, assuming conservation of sediment mass, as

$$\frac{\partial z_b}{\partial t} = -\frac{1}{1-p} \vec{\nabla} \cdot \vec{q}_t \quad (4.4)$$

with bed level z_b and sediment porosity $p = 0.4$.

By looping through the four modules, small perturbations in the bathymetry can grow and self-organise into rhythmic patterns through positive feedback between the bed level and the flow field. For further details on the model, see Dubarbier et al. (2017).

4.2.2 Model Setup

A synthetic bathymetry was created based on *in situ* measurements of the Sand Engine in November 2014 (Figure 4.2). First, a curved coastline was generated using a Gaussian shape function

$$X = p_1 + p_2 e^{-\frac{(Y+p_3)^2}{2p_4^2}} \quad (4.5)$$

with alongshore distance Y , cross-shore distance X , and function coefficients $p_1 = 253.36 \text{ m}$, $p_2 = -698.37 \text{ m}$, $p_3 = -494.33 \text{ m}$, and $p_4 = -926.30 \text{ m}$ following from the best non-linear fit through the measured 0 m contour line (Mean Sea Level, MSL). Second, a barred cross-shore profile was generated using the double slope profile function of Yu and Slinn (2003)

$$z_{prof} = \left(x_s - \frac{x_s}{\gamma} \right) \tanh \frac{\tan \beta_1 X}{x_s} + \frac{\tan \beta_1 X}{\gamma} - b_h e^{-b_w \left(\frac{x-x_c}{x_c} \right)^2} \quad (4.6)$$

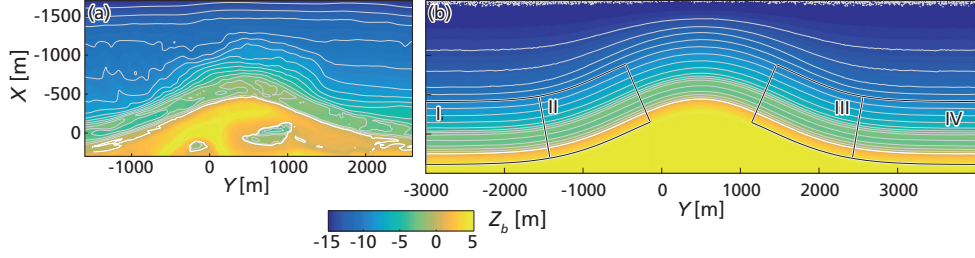


Figure 4.2: (a) Measured bathymetry in November 2014 at the Sand Engine (Rutten et al., 2018), and (b) synthetic bathymetry with a curved coastline and alongshore-uniform sandbar, based on measurements in (a). The black contours correspond to the boxes I-IV for the analysis of pattern growth rates.

with bed elevation z_{prof} , and function coefficients $\gamma = \tan\beta_1/\tan\beta_2$, $\beta_1 = 0.0372$, $\beta_2 = 0.0112$, $x_s = 3.63$ m, $x_c = -222.6$ m, $b_h = -2.39$ m, and $b_w = 11.07$ m which followed from the best non-linear fit with the measured alongshore-averaged profile (over a 500 m box) at the western side of the Sand Engine in November 2014. In this equation, the first term and second term on the right-hand side create a profile with slope β_1 in the upper part, changing at cross-shore position x_s into slope β_2 for the lower part of the profile. The last term creates a perturbation of amplitude b_h and width b_w at cross-shore position x_c , representing the sandbar. The profile extends up to +2 m MSL to anticipate for surged water levels. Third, the cross-shore profile was rotated along the Gaussian-shaped 0 m contour, resulting in a bathymetry with an alongshore-uniform subtidal bar located at equal distance from the curved shoreline. Fourth, the generated bathymetry was linearly interpolated on a Cartesian grid, as required by the model. The computational grid extended 2600 m in the cross-shore and 7000 m in the alongshore direction, with equal cross- and alongshore grid sizes of 10 m, and with the y -axis aligned with the regional coastline and the x -axis pointing into the dunes (negative values offshore). Fifth, depths beyond -15 m MSL were replaced by -15 m, and the bathymetry between the -12 m contour and the offshore boundary was recomputed to create a gradual fading of the Gaussian-shaped perturbation in these deep contour lines (see Figure 4.2b). Finally, random perturbations of <0.01 m were added to the bathymetry to trigger pattern formation in the nearshore zone.

Additional bathymetries were created with larger, smaller or zero coastline curvature to test the curvature effect on alongshore differences in crescentic bar patterns. The three additional bathymetries differed from the reference bathymetry in the cross-shore extension of the coastline perturbation, i.e. $p_2 = -698.37$ m in Eq. (4.5) was adjusted to $p_2 = -931.16$ m (initial extension Sand Engine, in 2011), $p_2 = -349.18$ m (1/2 of extension reference bathymetry), and $p_2 = 0$ m (straight coast).

The influence of significant wave height H_s and a time-varying wave angle θ on nearshore pattern formation were tested by running the model with sets of scenarios, providing information for examining our hypothesis on the importance of a spatiotemporal variation in local wave angle. Scenarios were based on wave conditions prevailing during the observed growth in crescentic patterns in the sandbar at the western side of the Sand Engine. As shown by Rutten et al. (2017) and Rutten et al. (2018), patterns developed at this side in autumn and winter with the passage of one or several storms. During such storms, the wave angle typically changed from southwest to north-northwest, which can be attributed to the southwest-northeast oriented storm track in the North Sea. To assess the effect of such a time-varying forcing on a barred curved coast, including the sensitivity to the wave angle itself (represent-

ing differently oriented storms), scenarios were generated with an alternating wave angle. Table 4.1 summarises the wave conditions for the different scenarios, applied at the offshore boundary. The scenario defined as reference (Run *Ref*) has a symmetric forcing, i.e. the wave angle alternated abruptly every day from shore-normal at the right flank ($\theta_1 = 25^\circ$) to shore-normal at the left flank ($\theta_2 = -25^\circ$) of the perturbation with $H_s = 2.0$ m and $T_p = 8.0$ s. Runs 1-11 are variations on the wave angle with θ_2 fixed at -25° , and $-55 \leq \theta_1 \leq 55^\circ$. Additional angle variations include the function of alternation (Runs 12-19) with gradual alternations from θ_1 to θ_2 following a sine and sawtooth function, and the period of angle alternation with a duration Dur_1 and/or Dur_2 of 0.5, 1.5 and 2.0 days (Runs 20-25). Sensitivity to wave height was tested for $1.6 \leq H_s \leq 2.4$ m (Runs 26-29). In all runs a directional spread of 30° was used. This value, assumed as typical for the North Sea, resulted in offshore leakage of wave energy at the offshore boundary under large wave angles (up to 9.3% for 55°). The ranges in wave angle θ , significant wave height H_s , and alternation period or function roughly typify the range in wave conditions observed at the Sand Engine (Rutten et al., 2017). Bathymetric variations (Runs 30-38) were applied to test the aforementioned effect of coastline curvature on pattern formation. On a strongly curved coast, a gently curved coast and a straight coast, three scenarios were tested that differed in θ_1 , with $\theta_1 = 25^\circ$ (Runs 30-32), $\theta_1 = -25^\circ$ (Runs 33-35), and $\theta_1 = 55^\circ$ (Runs 36-38).

Based on preliminary runs, scaling coefficients C_w , C_c and C_f , corresponding to the individual sediment transports, were adjusted from their default 0.08, 0.08, and 0.24 to 0.02, 0.04, and 0.05, respectively. This setting allowed a growth and evolution of crescentic bar patterns that resemble field observations at the Sand Engine (Rutten et al., 2018). In \vec{q}_w , \vec{q}_c , and \vec{q}_g a median grain diameter d_{50} of 290 μm was used. Here, morphological change was simulated for a 20-day period, updating the bed level every 30 minutes. For each updated bathymetry, the corresponding wave field and flow field were computed in stationary mode. Periodic lateral boundaries conditions were used.

4.2.3 Analysis of Model Results

To reveal insight in the evolution of sandbar patterns and the underlying flow field, stacks of a time-varying transect were created along the alongshore-averaged bar crest position. The definition of the alongshore transect is not trivial. First, the model allows cross-shore sandbar migration, and thus the position of the alongshore transect needs to be updated every time step, following the cross-shore migration of the sandbar crest. Second, the curved coast induces alongshore differences in cross-shore bar migration, and thus the alongshore-averaged profiles cannot simply be a global alongshore average but needs to be determined at a local scale. Here, we introduce a six-step approach to create time stacks along a curved coast. First, the bathymetry, z_b , was projected on local shore-normal transects, $z_{b,n}$, following the curved coastline. Second, alongshore-averaged profiles, $\overline{z_{b,n}}$, were computed by applying a moving average to the cross-shore profiles over an alongshore width of ~ 500 m. Third, the second derivatives corresponding to the profiles, $d^2 \overline{z_{b,n}} / dn^2$, were computed. Herein, smoothed profiles, using a 5-point Hanning window, were used, since the second derivative is rather sensitive to irregularities. Fourth, the bar crest positions were approximated by finding the minimum in $d^2 \overline{z_{b,n}} / dn^2$ that was nearest to the bar crest of the previous time step. Fifth, the bar crest location was determined at subgrid scale to allow for gradual onshore migration of the alongshore transect instead of discrete steps of 10 m corresponding to the grid resolution. Hereto a second order polynomial was fitted through $d^2 \overline{z_{b,n}} / dn^2$ at the bar crest approximation and its two neighbouring datapoints, giving a time-varying alongshore transect, $(X, Y)_t$. Sixth, bed elevation, the alongshore current and the total sediment transport,

Table 4.1: Overview of the runs. In the reference run *Ref*, a bimodal wave field was simulated by alternating the angle θ abruptly every day from θ_1 to θ_2 , for a total duration of 20 days. Variations on *Ref* include the forcing (Runs 1-29) and bathymetry (Runs 30-30). Red colours indicate the differences with *Ref*.

Run name	$H_{s,1}$	$T_{p,1}$	θ_1	Dur_1	$H_{s,2}$	$T_{p,2}$	θ_2	Dur_2	Other
<i>Ref</i>	2.0 m	8.0 s	25°	1 day	2.0 m	8.0 s	-25°	1 day	
1	2.0 m	8.0 s	-55°	1 day	2.0 m	8.0 s	-25°	1 day	
2	2.0 m	8.0 s	-45°	1 day	2.0 m	8.0 s	-25°	1 day	
3	2.0 m	8.0 s	-35°	1 day	2.0 m	8.0 s	-25°	1 day	
4	2.0 m	8.0 s	-25°	1 day	2.0 m	8.0 s	-25°	1 day	
5	2.0 m	8.0 s	-15°	1 day	2.0 m	8.0 s	-25°	1 day	
6	2.0 m	8.0 s	-5°	1 day	2.0 m	8.0 s	-25°	1 day	
7	2.0 m	8.0 s	5°	1 day	2.0 m	8.0 s	-25°	1 day	
8	2.0 m	8.0 s	15°	1 day	2.0 m	8.0 s	-25°	1 day	
9	2.0 m	8.0 s	35°	1 day	2.0 m	8.0 s	-25°	1 day	
10	2.0 m	8.0 s	45°	1 day	2.0 m	8.0 s	-25°	1 day	
11	2.0 m	8.0 s	55°	1 day	2.0 m	8.0 s	-25°	1 day	
12	2.0 m	8.0 s	25°	1 day	2.0 m	8.0 s	-25°	1 day	θ varies with sawtooth
13	2.0 m	8.0 s	35°	1 day	2.0 m	8.0 s	-25°	1 day	θ varies with sawtooth
14	2.0 m	8.0 s	45°	1 day	2.0 m	8.0 s	-25°	1 day	θ varies with sawtooth
15	2.0 m	8.0 s	55°	1 day	2.0 m	8.0 s	-25°	1 day	θ varies with sawtooth
16	2.0 m	8.0 s	25°	1 day	2.0 m	8.0 s	-25°	1 day	θ varies with cosine
17	2.0 m	8.0 s	35°	1 day	2.0 m	8.0 s	-25°	1 day	θ varies with cosine
18	2.0 m	8.0 s	45°	1 day	2.0 m	8.0 s	-25°	1 day	θ varies with cosine
19	2.0 m	8.0 s	55°	1 day	2.0 m	8.0 s	-25°	1 day	θ varies with cosine
20	2.0 m	8.0 s	25°	0.5 day	2.0 m	8.0 s	-25°	1 day	
21	2.0 m	8.0 s	25°	1.5 day	2.0 m	8.0 s	-25°	1 day	
22	2.0 m	8.0 s	25°	2 day	2.0 m	8.0 s	-25°	1 day	
23	2.0 m	8.0 s	25°	0.5 day	2.0 m	8.0 s	-25°	0.5 day	
24	2.0 m	8.0 s	25°	1.5 day	2.0 m	8.0 s	-25°	1.5 day	
25	2.0 m	8.0 s	25°	2 day	2.0 m	8.0 s	-25°	2 day	
26	1.6 m	8.0 s	25°	1 day	2.0 m	8.0 s	-25°	1 day	
27	1.8 m	8.0 s	25°	1 day	2.0 m	8.0 s	-25°	1 day	
28	2.2 m	8.0 s	25°	1 day	2.0 m	8.0 s	-25°	1 day	
29	2.4 m	8.0 s	25°	1 day	2.0 m	8.0 s	-25°	1 day	
30	2.0 m	8.0 s	25°	1 day	2.0 m	8.0 s	-25°	1 day	$4/3 * Amp_{Cross-shore}$
31	2.0 m	8.0 s	25°	1 day	2.0 m	8.0 s	-25°	1 day	$0.5 * Amp_{Cross-shore}$
32	2.0 m	8.0 s	25°	1 day	2.0 m	8.0 s	-25°	1 day	Straight coast
33	2.0 m	8.0 s	-25°	1 day	2.0 m	8.0 s	-25°	1 day	$4/3 * Amp_{Cross-shore}$
34	2.0 m	8.0 s	-25°	1 day	2.0 m	8.0 s	-25°	1 day	$0.5 * Amp_{Cross-shore}$
35	2.0 m	8.0 s	-25°	1 day	2.0 m	8.0 s	-25°	1 day	Straight coast
36	2.0 m	8.0 s	55°	1 day	2.0 m	8.0 s	-25°	1 day	$4/3 * Amp_{Cross-shore}$
37	2.0 m	8.0 s	55°	1 day	2.0 m	8.0 s	-25°	1 day	$0.5 * Amp_{Cross-shore}$
38	2.0 m	8.0 s	55°	1 day	2.0 m	8.0 s	-25°	1 day	Straight coast

i.e. the variables of interest, were linearly interpolated along $(X, Y)_t$, and will be referred to as $z_{b,c}$, $U_{ls,c}$, and $\vec{q}_{t,c}$, respectively.

To analyse the growth rate of crescentic patterns, a measure was computed for the amplitude of the patterns on every time step. Previous studies (Garnier et al., 2006; Garnier et al., 2010) computed the time-varying standard deviation of the bathymetry, this method is known as global analysis. More specifically, they computed the root-mean-square error of the deviation of the bathymetry from the time- and alongshore-averaged profile. Here, such a global approach is not sufficient, because the alongshore variability in pattern growth

rate is of interest. Therefore, we performed calculations at a local scale, in sections at the left straight coast, the left flank, the right flank, and the right straight coast (boxes I-IV in Figure 4.2b). Preliminary analysis showed that onshore bar migration at a curved coast introduces an alongshore variability related to migrational dynamics that contaminates the time- and intersectional average of the cross-shore profile and thereby the measure for pattern amplitude. Therefore, each section was divided into two subsections of about equal size. Then, the measure for pattern amplitude in each section followed from the weighted average of the standard deviation in the two corresponding subsections, also known as the pooled standard deviation. In equation-form, this measure for pattern amplitude $\|h\|$ in a section reads as

$$\|h\| = \sqrt{\frac{1}{N_1 + N_2 - 2} \left(\sum_{N_1} Z_{p,1}^2 + \sum_{N_2} Z_{p,2}^2 \right)} \quad (4.7)$$

and is proportional to the potential energy density of the bedforms ($0.5\|h\|^2$, Vis-Star et al., 2008). N_1 and N_2 are the number of elements in subsections 1 and 2, respectively. The deviation from the alongshore-averaged profile in a subsection reads as $Z_p(N, t) = z_{b,n}(N, t) - \overline{z_{b,n}}(t)$. Herein, bed elevations interpolated at the shore-normal transects $z_{b,n}$ were used.

The cross-shore and alongshore components of the flow vector field have often been found to be important variables to explain pattern formation (e.g. Garnier et al., 2013; Price et al., 2013). At a straight coast, the x - and y -component of a vector simply represent the cross- and alongshore component, respectively. Along a curved coast, however, the cross-shore and alongshore direction vary locally, and thus a local matrix rotation is needed to obtain a fair representation of both the cross- and alongshore component. The rotation angle φ in the rotation matrix was determined for every shore-normal transect, from the local gradient in the 10 m depth contour of the start bathymetry without perturbations. Then, the variable of interest, i.e. flow vector field, was linearly interpolated to shore-normal transects. Finally, the matrix rotation was applied to obtain the alongshore current U_{ls} . Similar to a vector field, a curved coast complicates interpretation of wave angles. The model gives the wave angle θ (we distinguish its time variation with θ_1 and θ_2) with respect to the global coastline orientation, while the wave angle with respect to the local coastline orientation may strongly differ along a curved coast. Here, the local wave angle θ_l was computed from the difference between the global wave angle θ and φ , where 0° denotes shore-normal incidence and positive values indicate waves propagating to the left.

4.3 Results

4.3.1 Reference Scenario

To interpret the results of the full set of scenarios, we first examine the reference scenario. Figure 4.3 shows that the onshore migrating sandbar develops crescentic patterns along the straight coast. On $t = 19$ days, several crescents have formed in the sandbar along the straight coast, while the flanks lack rhythmic morphology. Initiation of the first rip channels can be observed on $t = 10$ days at alongshore position $Y = -2600$ and $Y = 3450$ m. Along the flanks, onshore migration is negligible on the days when waves enter obliquely. Instead, the bar steepens due to erosion at its seaward flank and deposition at its crest (Figure 4.3). At the straight adjacent coast and the tip, the bar migrates onshore relatively rapidly. Here rates are up to 13 m/day on the first day, whereafter they decrease to 5 m/day at the straight coast and 7 m/day at the tip. Figure 4.4a-c shows the significant wave height H_s , the total sedi-

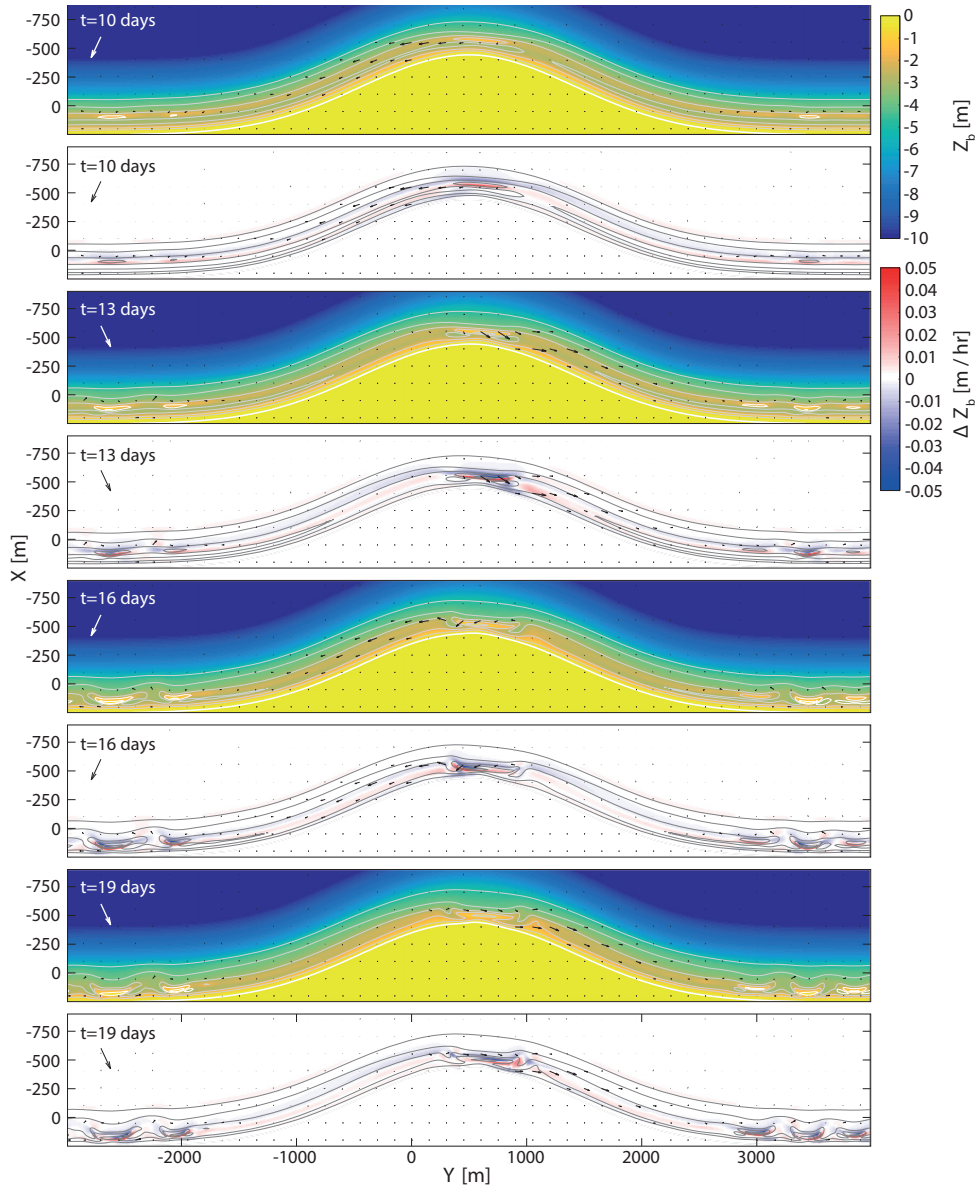


Figure 4.3: Bathymetric evolution (panel 1, 3, 5 and 7) and bed level change Δz_b (panel 2, 4, 6 and 8) of the reference scenario. Grey lines represent the depth contours, whereas the vectors indicate the total sediment transport. The arrows in the top left corner indicate the offshore wave angle.

ment transport \vec{q}_t , the resulting bed level changes Δz_b and the wave and current vectors at $t = 0$ days, when waves enter obliquely from the right side ($\theta_1 = 25^\circ$) and the sandbar is still alongshore uniform. For the same day, Figure 4.5 shows, for each cross-shore profile, the wave height at breaking H_b , the local angle at breaking $\theta_{l,b}$, the alongshore current at the bar crest $U_{l,c}$ and the total sediment transport at the bar crest $\vec{q}_{t,c}$. The abrupt drop in H_s ,

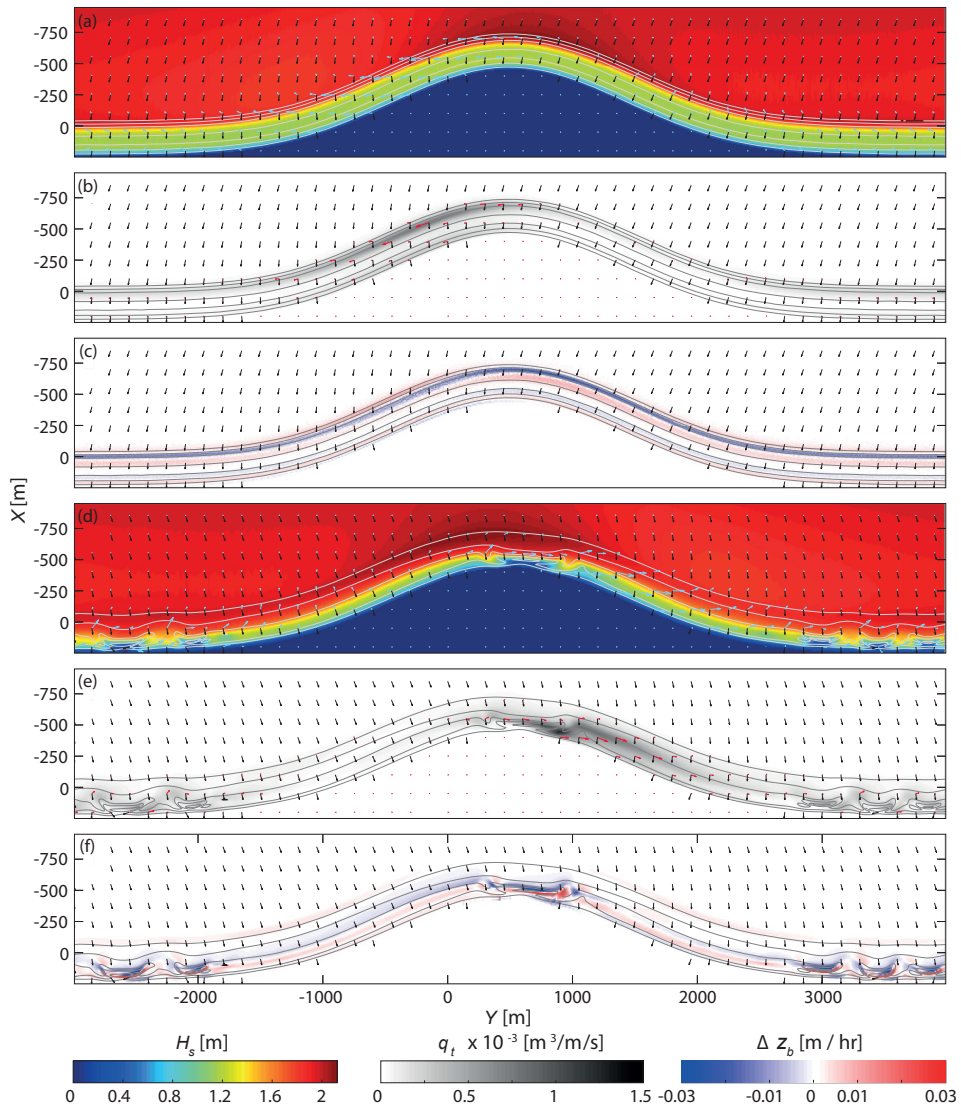


Figure 4.4: Patterns in (a,d) significant wave height H_s , (b,e) total sediment transport \vec{q}_t , and (c,f) bed level change Δz_b on $t = 0$ days (a-c) and $t = 19$ days (d-f) for the reference scenario. Vectors indicate the wave angle (black; a-f), current velocities (blue; a,d), and total sediment transport (red; b,e).

in Figure 4.4a, indicated by the change in colour shading (red to yellow), is caused by wave breaking at the bar crest. The alongshore variation in H_s and H_b can be explained by the refraction pattern. At the right flank (section III), waves propagate nearly normal to the depth contours (note the gradually increasing curvature in the deep (15 m to 12 m MSL) contour lines; Figure 4.2) and thus hardly refract. This results in limited divergence of the wave rays, limited redistribution of the wave energy, and thus a minor decrease in H_s and H_b . At the same time along the left flank (section II), waves approach the coast obliquely, thus refract

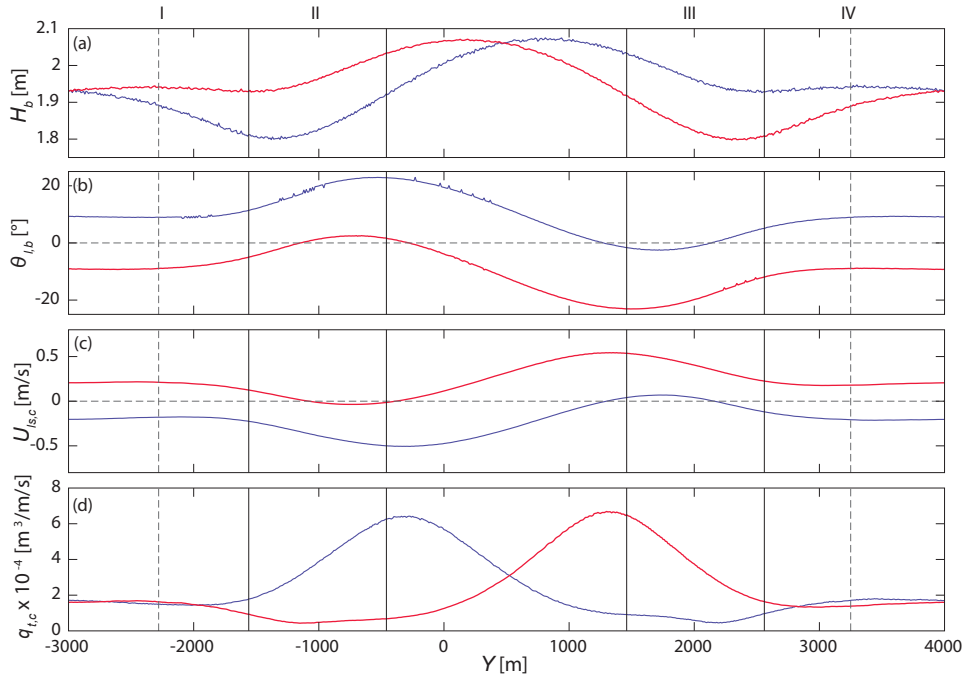


Figure 4.5: Alongshore variation in (a) breaker wave height H_b , (b) breaker angle $\theta_{l,b}$, (c) alongshore current at bar crest $U_{ls,c}$, and (d) total sediment transport at bar crest $\bar{q}_{t,c}$ on $t = 0$ days (blue) and $t = 1$ days (red). Vertical dashed lines indicate where the first crescentic patterns developed. Vertical solid lines indicate sections I-IV as shown in Figure 4.2b.

considerably and reduce in height when propagating onshore. Here, $\theta_{l,b}$ is still substantial ($\sim 25^\circ$). At the tip, the wave rays converge, resulting in a substantial increase in H_s and H_b . At the adjacent beaches (sections I and IV), where waves approach the coast under $\theta \sim 25^\circ$, refraction is limited and $\theta_{l,b}$ relatively small ($\sim 9^\circ$; Figure 4.5b). Consequently, the resulting alongshore current is of moderate strength (~ -0.21 m/s) and leftward directed along the straight coast, nearly zero at the right flank, and strongest (~ -0.5 m/s) at the left flank (Figure 4.4a, blue arrows; Figure 4.5c). The total sediment transport \bar{q}_t (Figure 4.4b, red arrows) is of small magnitude and slightly onshore directed along the straight coast, almost absent at the right flank, and relatively large ($\bar{q}_{t,c} \sim 6.4 \times 10^{-4}$ m³/m/s; Figure 4.5d) and directed along the sandbar crest at the left flank. Although the pattern in \bar{q}_t is largely in line with the flow vector field and thus dominated by sediment transport related to the mean-current (\bar{q}_c), also onshore directed sediment transport related to wave-skewness (\bar{q}_w) contributes to the total sediment transport and causes the cross-shore component of the total sediment transport to be zero (along left flank) or onshore directed (along straight coast and right flank). Consequently, bed level change (Figure 4.4c), where erosion relates to positive gradients in the total sediment transport in the landward direction and deposition to negative gradients, results in a ~ 10 m onshore bar migration along the entire coastline after the first day. Along the right flank and the straight coast the bar steepens, while it flattens along the left flank. By shifting θ at the offshore boundary, every day from 25° to -25° , the patterns in wave refraction, currents, sediment transport and bed level change are similar to the patterns de-

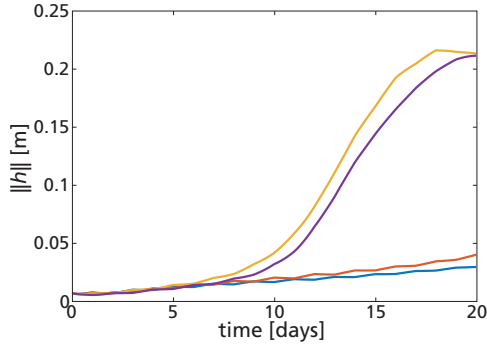


Figure 4.6: Time evolution of the measure for pattern amplitude $\|h\|$ showing the alongshore difference in growth rate of patterns in section I (yellow), section II (blue), section III (red), and section IV (purple; see Figure 4.2b) in the reference scenario.

scribed above for $t = 0, 2, 4, \dots, 18$ days but mirrored across the vertical in $Y = 500$ m for $t = 1, 3, 5, \dots, 19$ days (e.g. Figures 4.4d-f; Figure 4.3; Figure 4.5). Eventually, alongshore variability develops in the sandbar along the straight coast (visible from $t = 10$ days onwards, Figure 4.3). More specifically, alongshore variabilities in the 2D horizontal flow field, i.e. onshore directed flow over shallower parts of the bar and seaward directed flow over the deeper parts, force the development of horizontal circulation cells, stimulating crescentic pattern formation through positive feedbacks. Note that the first rip channels develop at the same location at the left and right flank ($Y = -2280$ and $Y = 3250$ m), which may be explained by the most preferential conditions for crescentic patterning over time, i.e. high waves at breaking, $H_b = 1.9$ m, which approach near-normally ($\theta_{l,b} \sim 9^\circ$). Consequently, the bar rapidly reaches small depths, where patterns could develop more easily through an increased cell circulation and limited alongshore currents ($U_{ls,c} \sim 0.21$ m/s; Figure 4.5). The absence of crescents along both flanks of the perturbation may be explained by the strong alongshore-directed currents (0.54 m/s) every other day when the waves approach one of these coasts obliquely, hindering the development of cell circulation. The time evolution of the measure for pattern amplitude $\|h\|$ is shown in Figure 4.6 for four sections of the coast, revealing the alongshore variability in growth rate of the crescentic patterns. Initially, $\|h\|$ increases slowly. After $t = 8$ days, $\|h\|$ rapidly increases for the sections with a straight coastline (sections I and IV; yellow and purple line). After $t = 16$ days, the growth rate slows down again. For both sections at the flanks (sections II and III; red and blue line), $\|h\|$ does not show a strong increase that is typical for pattern formation within the 20-day simulation period. Thus, $\|h\|$, estimated as pooled standard deviation, clearly describes the spatiotemporal variability in patterning as observed in Figure 4.3.

4.3.2 Effect of Wave Angle

Figure 4.7 shows the bathymetry at $t = 19$ days for the 11 variations in wave angle with respect to the reference scenario (Table 4.1). The occurrence and alongshore positioning of crescentic patterns along the curved coast vary with the scenario. All scenarios with forcing from the left side only (Runs 1-6) create crescentic patterns along the left flank (section II), but only Runs 4-6 create patterns along the straight coast (sections I and IV) as well. For the scenarios with forcing from both the left and right side, crescentic patterns develop along the straight coast (sections I and IV; Runs 7-9, *Ref*), except for Runs 10-11 that show minute

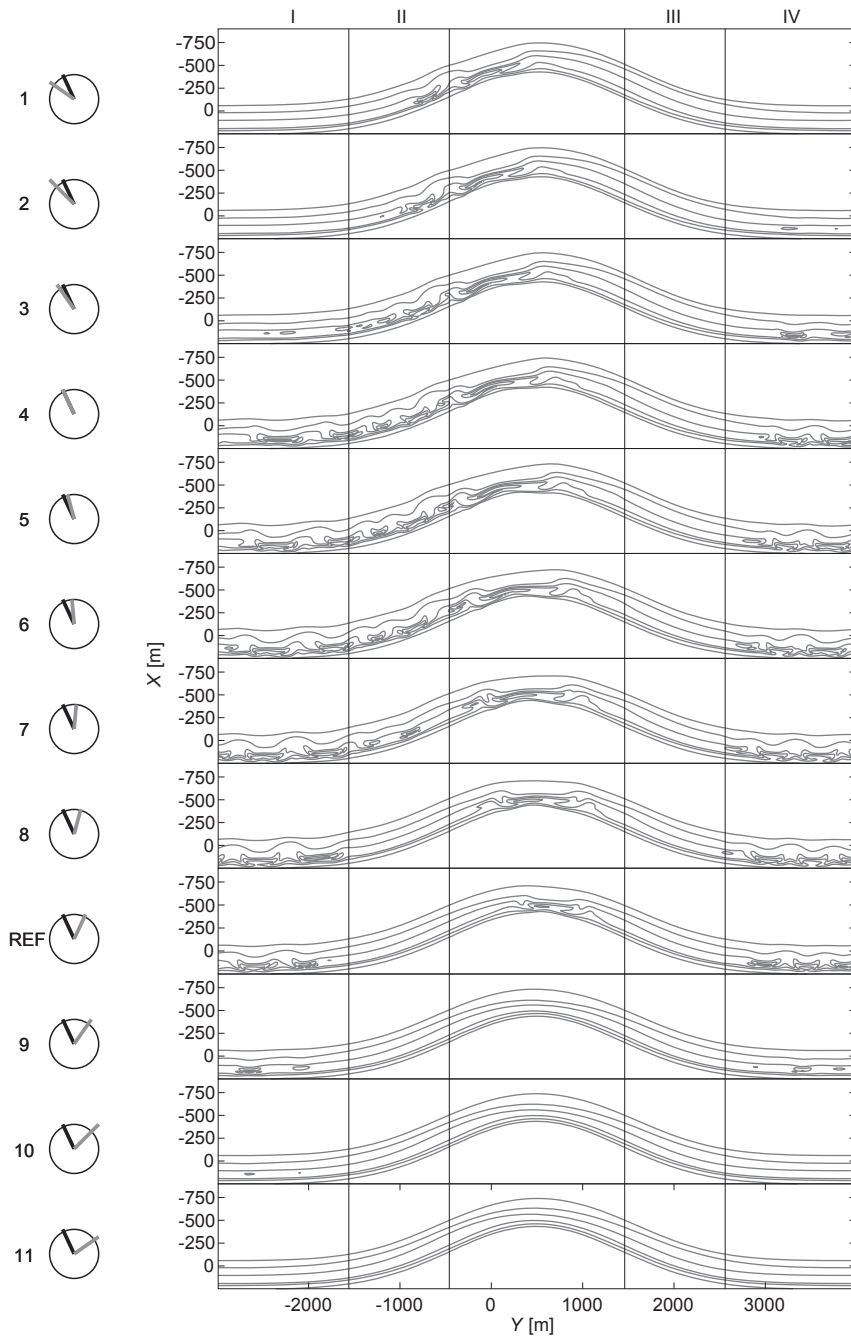


Figure 4.7: Bathymetric contours at $t = 19$ days for Runs 1-11, wherein θ_1 varies from -55° to 55° and θ_2 is constant at -25° . Angle variations are schematised by the circles on the left, wherein the grey and black radius indicate θ_1 and θ_2 , respectively. Vertical solid lines indicate sections I-IV as shown in Figure 4.2b.

alongshore variability. Hardly any patterns develop along the left flank (section II) in the two-sided scenarios. Figure 4.8 shows the temporal evolution of the depth in the bar zone for the different scenarios (first column), and illustrates that the growth rates of crescentic patterns vary strongly both within and between the different scenarios (second column). The time period at which the growth of alongshore variability in depth and position of the bar crest stabilises varies from several days to beyond the simulation period of 20 days. Generally, crescentic patterns start to develop within the simulation period where maximum $\theta_{l,b} < 13^\circ$, and they develop the fastest along stretches of the coast where locally wave obliquity was the smallest. For example, in Run 7 crescentic patterns develop first along the straight coast (sections I and IV), and subsequently start to form along the left flank (section II). This alongshore difference in growth rate can be clearly noted in the time evolution of $||h||$ corresponding to the four sections (I-IV; Figure 4.8). Here, waves approach rather obliquely half of the time ($t = 0, 2, \dots, 18$ days) along the left flank ($\theta_{l,b} \sim 15^\circ$), whereas the straight coast is exposed to smaller obliquity ($\theta_{l,b} \sim 9^\circ$ on $t = 1, 3, \dots, 19$ days). This confirms the preference of crescentic patterning for low obliquity. Furthermore, Figure 4.8 shows that crescents along the straight coast (sections I and IV) clearly migrated alongshore in rightward direction (rates up to ~ 20 m/day) in Runs 4-6 wherein waves approached from the left side only, whereas crescents in Runs 8-11 and *Ref* migrated alternately leftward and rightward, correlating with the alternating wave angle between the left side and right side.

In line with the reference scenario, local obliquity may prevent or slow down the growth of crescentic patterns because of reduced local wave heights, and strong alongshore currents that inhibit cell circulation. The third column in Figure 4.8 shows the alongshore current $U_{ls,c}$ for the different scenarios on $t = 0$ days (blue line) and $t = 1$ days (red line), wherein positive and negative values indicate a rightward and leftward directed current, respectively. All one-sided scenarios (Runs 1-6) generate an alongshore current that is alternately small (condition 1: $t = 0, 2, \dots, 18$ days) or near-zero (condition 2: $t = 1, 3, \dots, 19$ days) along the left flank (section II). Presumably, horizontal cell-circulation prevails during the full 20-day simulation period (both condition 1 and 2), stimulating crescentic pattern formation within this section. At the same time, large continuously rightward directed $U_{ls,c}$ along the right flank (section III) prevents circulation cells and crescentic patterns to develop here. In Runs 9-11 both the flanks and the straight coast are subjected to large incidence angles (under either θ_1 or θ_2), and thus large $U_{ls,c}$, inhibiting formation of distinct alongshore variability. Along the straight coast (sections I and IV), increased crescentic growth rates towards Runs 6-7 can be explained by the increase in shore-normal waves during condition 1 (θ_1), and thus decrease in the magnitude of $U_{ls,c}$. Similarly, the fastest growth rate of crescentic patterns along the left flank (section II) can be observed in Run 4, when $U_{ls,c} \sim 0$ under both θ_1 and θ_2 . Near-normal waves stimulate the development of crescentic patterns also because wave energy barely redistributes due to refraction, resulting in a relatively high H_b and consequently strong cell circulation. In addition, the curvature in the coastline imposes an alongshore variation in $U_{ls,c}$ that potentially contributes to pattern formation. The alongshore current converges (downward zero-crossing in right column of Figure 4.8) and diverges (upward zero-crossing) within all scenario variations (Runs 1-11, *Ref*) for at least one of the two conditions, as an alongshore gradient in the water level was created by defocusing and focusing of the waves near the tip of the curved coast, respectively. More specifically, positive feedback between the bed and an offshore directed flow, fed by the opposing rightward and leftward directed current at the convergence point, may have contributed to the formation of a rip channel (e.g. Run 4 at $Y = -1100$ m). However, this mechanism does not seem to have initiated the rips as patterns develop at nearly similar rate away from the convergence point in the flow field (e.g. sections I and IV). Run 6 crashed at $t = 10.9$ days, possibly due to the

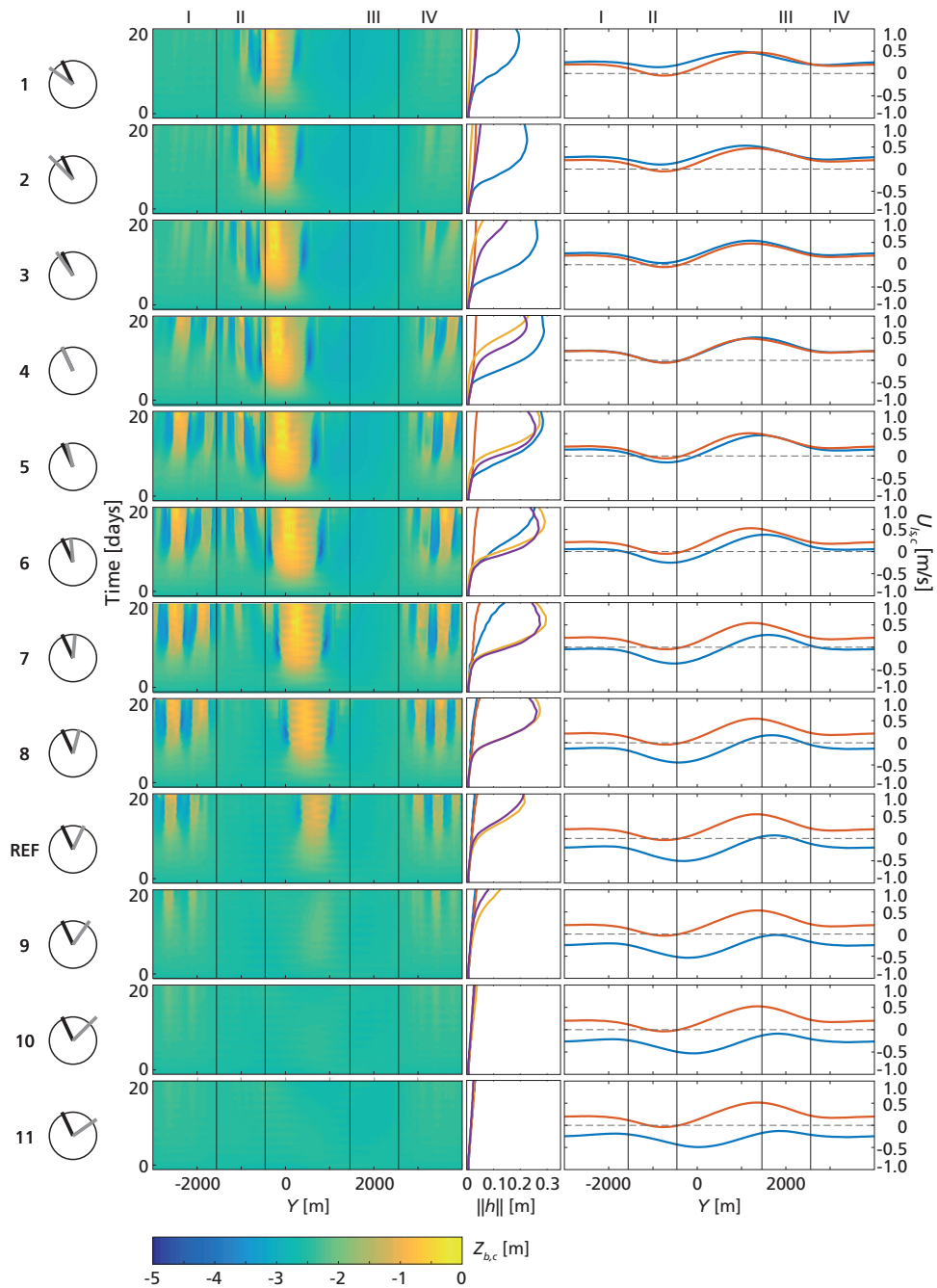


Figure 4.8: Simulated (left column) 20-day evolution of the bed at the bar crest $z_{b,c}$, and (right column) alongshore current at the bar crest $U_{ls,c}$ on $t = 0$ days (blue) and $t = 1$ days (red) versus alongshore position for Runs 1-11. Time evolution of the measure for pattern amplitude $||h||$ is shown in the middle column, for section I (yellow), section II (blue), section III (red), and section IV (purple). Angle variations are schematised by the circles on the left, wherein the grey and black radius indicate θ_1 and θ_2 , respectively. Positive and negative values of $U_{ls,c}$ indicate a rightward and leftward directed current, respectively. Vertical solid lines indicate sections I-IV as shown in Figure 4.2b.

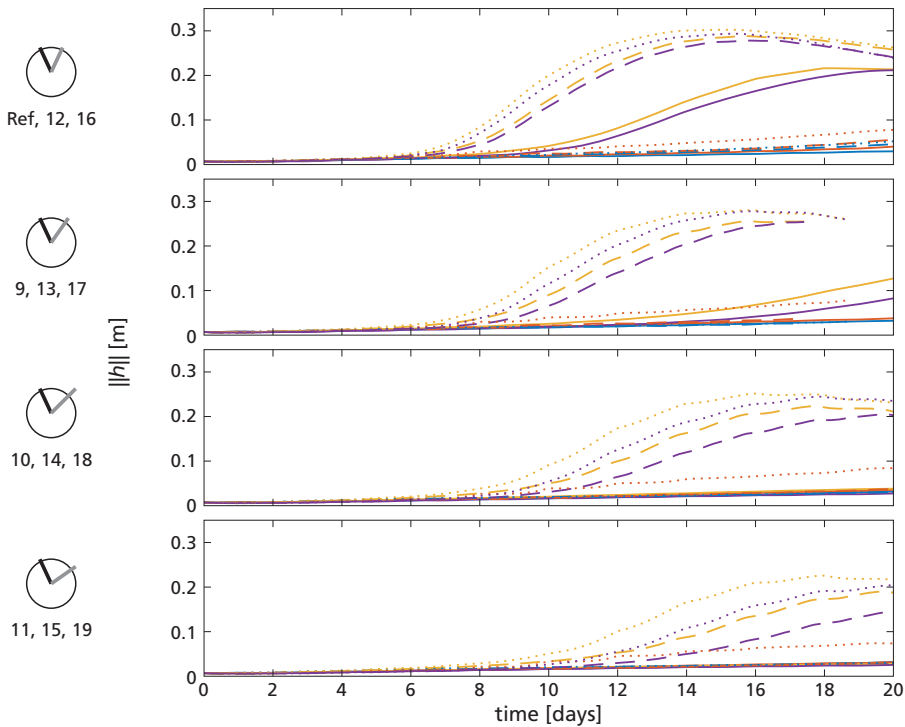


Figure 4.9: Time evolution of the measure for pattern amplitude $\|h\|$ for section I (yellow), section II (blue), section III (red), and section IV (purple). Differences in growth rate follow from varying the angle from θ_1 to θ_2 abruptly (solid lines), through a sawtooth function (dotted) and a cosine function (dashed). Herein, θ_1 was changed from 25° (top panel), to 55° (bottom panel).

fast onshore bar migration near the curved coast's tip, which resulted in a flow field too complex to be solved by the model. Run 6 with a smaller morphological time step of 15 minutes prevented crashing of the simulation, which results are included above.

The importance of low obliquity on the positioning and growth rates of crescentic patterns is corroborated by simulations with gradually varying θ , following either a sawtooth curve (Runs 12-15) or a cosine function (Runs 16-19). Figure 4.9 shows that $\|h\|$ increases more rapidly at the straight coast (sections I and IV) for both sawtooth (dotted line) and cosine variations (dashed line). For example, $\|h\|$ in section I increases beyond 0.05 m after 7.2 days in Run 12 (sawtooth) and after 7.9 days in Run 16 (cosine), while it takes 10.6 days in Run *Ref* having the same θ_1 and θ_2 but with an abrupt alternation. In addition, the sawtooth variations (red dotted line) have a relatively large $\|h\|$ for the right flank (section III), which related to the cascading of patterns in section IV into section III. Higher $\|h\|$ can be explained by the locally increased exposure time of near-normal waves, especially in the sawtooth variations, and thus shorter exposure to large $U_{ls,c}$ under a gradually varying θ . Although Run 13 crashed at $t = 17.4$ days and Run 17 at $t = 18.7$ days, the trends in $\|h\|$ are clear. Therefore, no additional simulations were run to cover the full 20-day period. The influence of exposure to low obliquity on the pattern formation is additionally reflected in Runs 20-22, indicating that longer exposure (up to 2 days) of shore-normal waves at the right flank results in increased

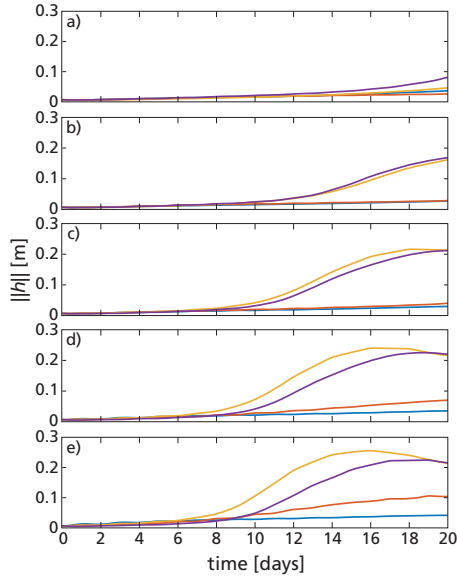


Figure 4.10: Time evolution of the measure for pattern amplitude $||h||$ in section I (yellow), section II (blue), section III (red), and section IV (purple; Figure 4.2b), for time-varying wave height H_s . Herein, $H_{s,1}$ increased from (a) 1.6 m (Run 26), to (e) 2.4 m (Run 29), while $H_{s,2} = 2.0$ m.

growth rates (not shown). The chronology in the time-varying forcing has no substantial effect on pattern formation for exposure times between 0.5 day (Run 23) and 2 days (Run 25; not shown). To summarise, the overall picture that arises from our simulations is that the positioning and growth rate of crescentic patterns along a curved coast vary with the local wave angle. Low obliquity stimulates pattern formation through increased cell circulation because of a limited alongshore current and limited refraction-induced energy reduction (and thus high H_b). Potentially, convergence and divergence in the flow field contribute to pattern formation as well.

4.4 Discussion

4.4.1 Variations on the Wave Characteristics

We have investigated how the local wave angle affects alongshore differences in patterning for a given offshore wave height. Below, we explore the effects of changes herein (Runs 26-29) on the findings of the reference run. Figure 4.10 shows how the growth of crescentic patterns depends on the incoming wave height. Generally, an increase in the wave height results in increased growth rates, consistent with Calvete et al. (2005) and Castelle and Ruessink (2011). Figure 4.10 also shows that a time-varying H_s affects the pattern growth rate differently within the four sections. The alongshore positioning of the patterns, however, is not substantially affected, as patterns start to develop along the straight coast (sections I and IV, yellow and purple line in Figure 4.10) and slowly extend along the flanks (sections II and III, blue and red line in Figure 4.10) within all runs. To summarise, a time-varying wave height influences the pattern growth rate and its alongshore variability, but to a relatively small extent in comparison to a time-varying wave angle (compare Figure 4.8 and 4.10).

4.4.2 Variations on Coastline Curvature

Runs 1-29 illustrate that a curved coast imposes alongshore differences in the local wave angle, the resulting flow field, and consequently pattern formation. Below, we discuss how variations on the curvature of the coastline (Runs 30-38) affect pattern formation, which is relevant in the design of km-scale nourishments and the anticipated alongshore diffusion of such coastline perturbations in perspective of swimmer safety (e.g. modified large-scale flow pattern due to km-scale nourishments, Radermacher et al., 2017). In fact, the coastline curvature is expected to affect crescentic pattern formation in a similar way as the offshore wave angle, i.e. variation in alongshore positioning and growth rate, since for both scenario variations the local wave angles change as they are a function of the offshore wave angle and the coastline orientation. Figure 4.11 shows that the alongshore positioning of crescentic patterns does not change substantially for the selected range of coastline curvatures, in contrast to the growth rate of $||h||$. In Runs 30-38 the growth rate decreases for a smaller curvature, in particular for the straight coast scenarios (Runs 32 and 35). The decrease in growth rate in sections I and IV (Runs 30-32) relates to an increasing magnitude of $U_{ls,c}$ with decreasing coastline curvature, from a range of 0.15-0.22 m/s at the strongly curved coast (Run 30) to 0.24 m/s (Run 32) at the straight coast in these sections. Note that the range values are based on the condition with the largest $U_{ls,c}$. The increase in $U_{ls,c}$ and resulting decrease in growth rate cannot simply be explained by the difference between the offshore wave angle and the coastline orientation, since both do not change within sections I and IV. However, sections I and IV are exposed to waves that refracted increasingly under both θ_1 and θ_2 for coasts with stronger curvature, resulting in lower $\theta_{l,b}$, H_b , and thus lower $U_{ls,c}$. In section II, the growth rate variation between Runs 33-35 also relates to $U_{ls,c}$, which varies from 0.003-0.13 m/s (Run 4) to 0.25 m/s (Run 35). Here, the varying magnitude of $U_{ls,c}$ depends mainly on the coastline orientation in section II. Besides, the left flank in these runs is not as strongly subjected to refraction as in Runs 30-32 since waves do not approach as strongly obliquely here. In Figure 4.11, information of Run 33 is partly missing, because the run crashed at $t = 10.7$ days. Attempts to simulate the full 20-day period using a smaller morphological timestep of 15 or 10 minutes were unsuccessful. No patterns arise within the 20-day simulation period in Runs 36-38, which can be explained by the relatively large $U_{ls,c}$ of 0.15-0.57 m/s along the entire coastline under either θ_1 or θ_2 , irrespective of a curved coastline.

Overall, our simulations demonstrate that rip channels, located between the lunate-shaped shoals of the crescentic bar, develop at faster rate and become deeper with increasing curvature of the coastline in wave climates with low obliquity. Under such conditions, curved coasts impact rip channel dynamics along their flanks as well as their adjacent straight coastlines, because of the alongshore varying coastline orientation and the global refraction pattern. Increased rip channel presence at the straight coasts adjacent to the curved coast can enforce localised beach and dune erosion (Thornton et al., 2007). Moreover, rip channels are associated with narrow and approximately offshore-directed flows (rip currents) which are the leading deadly hazard to recreational beach users worldwide (Castelle et al., 2016). Accordingly, both the design and location of km-scale nourishments must be carefully examined in perspective of the prevailing wave climate and the primary beach entries at the foreseen site.

4.5 Conclusions

The formation of crescentic patterns was numerically simulated for an initially alongshore-uniform sandbar along a curved coast under time-varying wave angle θ . We found that

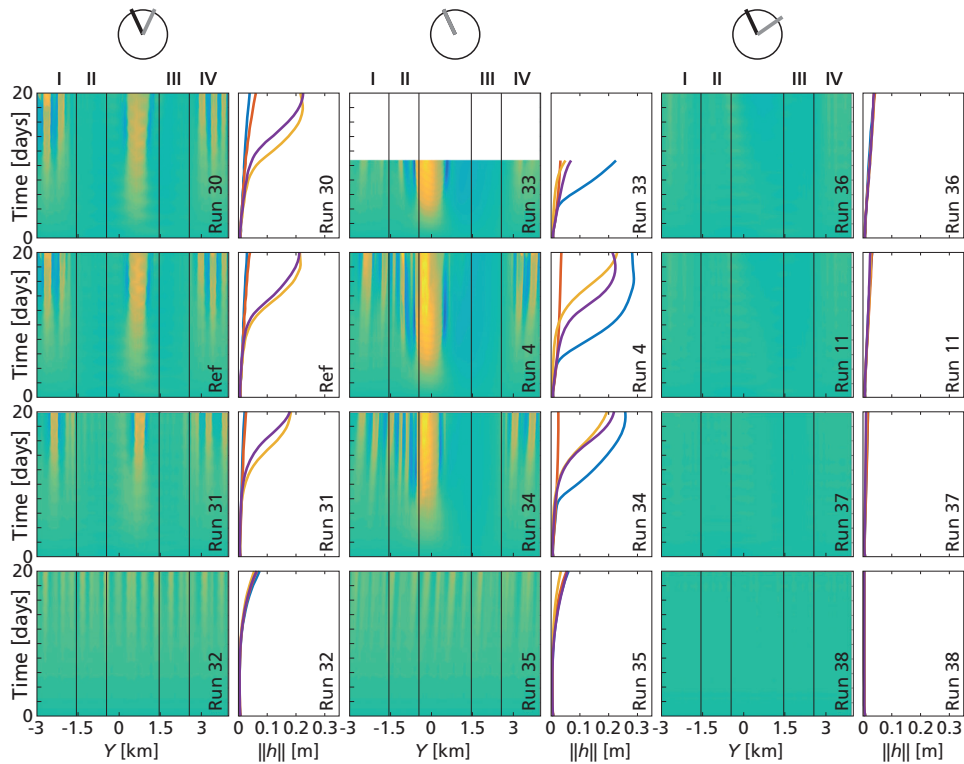


Figure 4.11: Simulated (column 1, 3 and 5) 20-day evolution of the bed at the bar crest $z_{b,c}$ versus alongshore position, and (column 2, 4 and 6) the measure for pattern amplitude $||h||$, for variations on the coastline curvature from strongly curved (top row) to straight (bottom row). Here, $||h||$ was computed for section I (yellow), section II (blue), section III (red), and section IV (purple), which positions are indicated in the panels with timestacks and in Figure 4.2b). Angle variations are schematised by the circles on the top, wherein the grey and black radius indicate θ_1 and θ_2 , respectively.

the occurrence and growth rate of patterns varied alongshore with the local breaker angle, $\theta_{l,b}$. Patterns arose within the 20-day simulation period where local obliquity was limited to $\theta_{l,b} < 13^\circ$. Variations of θ , i.e. its value and the shape or period of its time-varying function, affected $\theta_{l,b}$ and thereby the alongshore positioning and growth rate of the patterns. The preference of low obliquity for crescentic pattern formation can be attributed to the limited strength of alongshore currents and limited refraction-induced wave height reduction. Both positively affect the generation of horizontal circulation cells in the flow field that initiate crescentic pattern formation through positive feedbacks between the flow field and the bed. Simulations in which the coastline curvature was varied, from strongly curved to straight, confirm the important negative effect of the alongshore current on pattern formation. The occurrence and growth rate of crescentic bar patterns and associated rip channels increased with coastline curvature, given a wave climate with low obliquity. Consequently, km-scale nourishments with a curved coast may enforce rip dynamics and associated flows that threaten swimmer safety.

Acknowledgements

J.R. and B.G.R. were supported by the Dutch Technology Foundation STW that is part of the Dutch Organisation for Scientific Research (NWO), and which is partly funded by the Ministry of Economic Affairs, under contract 12686 (Nature Coast: S1 Coastal Safety). T.D.P. was funded by the Dutch Organisation for Scientific Research (NWO), under contract 016.Veni.171.101. B.D. and B.C. were funded through projects CHIPO (ANR-14-ASTR-0004-01) and SONO (ANR-17-CE01-0014), respectively, from Agence National de la Recherche (ANR). Computer time for this study was provided by the computing facilities MCIA (Mésocentre de Calcul Intensif Aquitain) of the University of Bordeaux and the University of Pau and Pays de l'Adour. Field data used to create the synthetic bathymetry are from Rutten et al. (2018). The model is a research code under continuous development and is not released publicly at this stage, but can be provided on demand.

Chapter 5

Synthesis

This thesis aimed to improve the understanding of sandbar behaviour along the curved coast of the dynamic, km-scale Sand Engine nourishment at daily to seasonal timescales. Hereto, the accuracy of bed elevations derived from X-band radar and optical video data was assessed to determine the applicability of such data in sandbar analyses (Chapter 2). Subsequently, sandbar dynamics along the curved Sand Engine coast were analysed from time-averaged video data (Chapter 3), and mechanisms underlying the observed alongshore variability in these dynamics were explored using a numerical model (Chapter 4). Below, the findings in Chapter 2-4 are summarised, discussed, and directions for future work are outlined.

5.1 Main findings

1. *How can morphologic behaviour accurately be monitored in a dynamic, km-scale nearshore setting?*

Large nearshore regions (km^2) can be morphologically monitored with a small sampling interval (hours) at relatively low cost, using shore-based remote sensing platforms. Since many years, the elevation of the seabed z_b has been estimated by retrieving the frequency Ω and wave number k of the waves from image data, and subsequently, using a model that relates Ω and k to water depth. Herein, the focus has been on improving accuracies of z_b . Several approaches to derive z_b have emerged, which mainly differed in their models and methods of Ω - k retrieval, and whereof some are specific to a platform or environmental and physical boundary conditions. So far, it is yet unclear when and where different approaches may actually complement each other.

Chapter 2 assessed the accuracy of z_b , based on image data collected at the Sand Engine by two commonly used platforms with their own method of Ω - k retrieval. Data collected by an X-band radar were processed with a fast Fourier transform (FFT) method, whereas optical video data were processed with a cross-spectral (CS) method. In both approaches z_b had a systematic bias, being too shallow at larger depth and too deep at small depth. Intermediate depths had negligible bias. At larger depth, the bias may originate from waves that were insensitive to the bed. At small depths, non-linearity of the waves may have contributed to the bias, since this effect is not included in the model although potentially important in shallow water. Besides, the large bias in the radar-FFT approach (2.3 m for $z_b > -6$ m), compared to the video-CS approach (0.92 m for $z_b > -1$ m), may be explained by the inhomogeneity of the wave field in the 960 by 960 m analysis windows. Large-scale morphologic change over a 1-year period was determined by the computation of the volume of sand in a certain domain. The volumetric accuracy, however, was found to strongly depend on the domain considered in the computations and to be highly variable at daily timescales. Therefore I decided z_b derived by the two approaches to be cur-

rently insufficiently accurate to quantify sandbar behaviour at this site at daily to monthly timescales. Instead, I continued in Chapter 3 with morphometric parameters, such as sandbar position, extracted from time-averaged video imagery. This technique, proven at many sites (e.g. Lippmann and Holman, 1989; Van Enckevort et al., 2004; Pape et al., 2010), approximated the bar crest location with sufficient accuracy of $O(10\text{ m})$ at the Sand Engine study site in the Netherlands (Appendix A).

2. *What is the spatiotemporal variability in sandbar behaviour along the convex curved coast of the Sand Engine at daily to seasonal scales?*

A km-scale perturbation creates an alongshore varying orientation of the coastline, which potentially imposes alongshore differences in the local wave field and consequently in sandbar behaviour. At embayed beaches and cusped deltas, both characterised by a curved coastline, an alongshore variation has been observed in the cross-shore migration and the geometry of sandbars. So far, it remains unclear whether such alongshore variability in bar behaviour is also introduced by the curved coastline of a man-made km-scale perturbation.

Chapter 3 analysed sandbar behaviour at the convex curved coastline of the Sand Engine, and determined its governing boundary conditions. Hereto, morphologic change was quantified in boxes north and west of the Sand Engine's tip, using a 2.4-year dataset of daily low-tide, time-averaged video images and bathymetric measurements at a 2-monthly basis. No large differences were observed in cross-shore sandbar migration at the northern and western side. Both sides were characterised by a clear seasonal onshore and offshore migration, which was associated with the seasonally varying wave power. Distinct differences between both sides were, however, observed in sandbar geometry and its change (3D behaviour). More specifically, the depth of the bar crest and its distance from the shoreline differed, as well as the crescentic patterns in the bar. At the western side, crescents with length scales of 400-500 m formed in the energetic autumn months and these coupled to patterns in the shoreline. At the northern side, crescents of $\sim 200\text{ m}$ formed typically in the spring season. At both sides, the bar straightened when energetic waves approached locally oblique, which was not necessarily at the same moment at the northern and western side. Based on the data I hypothesised that the alongshore differences in geometry related to local differences in breaker height, whereas the timing differences in pattern formation and bar straightening related to the local wave angle.

3. *What are the underlying mechanisms behind alongshore variability in the formation of crescentic sandbar patterns along a convex curved coast under time-varying wave forcing?*

Chapter 3 showed that crescentic patterns formed at the western side of the Sand Engine under storms passing from southwest to northwest, and at the northern side under prolonged periods of moderately energetic waves with near-normal incidence angles. Generally, pattern formation has been associated with near-normal waves, driving a horizontal circulation in the flow field that stimulates patterning. Increasing wave obliquity is understood to intensify the alongshore current and weaken the cross-shore current, resulting in a weaker cell circulation and decreased growth rates of patterns. However, this general understanding is solely based on studies at straight coasts. Yet, it is unknown whether the mechanism behind pattern formation is similar at a curved coast.

Chapter 4 explored systematically how a convex curved coast contributes to alongshore variability in crescentic pattern formation, using a non-linear morphodynamic model. Patterns were simulated in an initially alongshore-uniform bar under a time-varying angle, with environmental and hydrodynamic boundary conditions based on measurements

at the Sand Engine. Simulations show that the alongshore positioning and growth rate of the patterns varied with the local breaker angle $\theta_{l,b}$, which depends on the offshore wave angle and the coastline curvature. Consistent with observations in Chapter 3 and earlier studies, patterns developed faster under near-normal wave angles. Under such conditions, both refraction-induced reduction of the wave height and the strength of the alongshore current were limited. With increasing coastline curvature, the pattern growth rate increased, given that the wave climate was low oblique. This implies that rip currents, associated with crescentic patterns and known as deadly hazards to swimmers, may intensify and become more abundant by the implementation of a concentrated, km-scale nourishment.

5.2 Discussion and perspectives

5.2.1 Future directions in nearshore monitoring

The relatively low costs, high temporal and spatial resolutions and large spatial coverage inherent to remote sensing, together with promising information of the seabed or flow field retrieved from image data (Holman and Haller, 2013), have created high expectations of such information as input into numerical models, model-data integration schemes, and coastal safety studies. Ideally, image-retrieved information will ultimately replace *in situ* data, which collection is time-consuming, relatively expensive, and limited to low-energetic seas. In Chapter 2, the accuracy assessment of bed elevation derived from X-band radar data and optical video data showed that bed estimates had a systematic bias and did not yet reach the $O(0.1 \text{ m})$ accuracy of *in situ* bed elevations. Depending on the goal of study and the spatial and temporal scales involved, the bias needs to be reduced. To benefit morphodynamic studies of meso-scale patterns $O(100 \text{ m})$ on daily to seasonal timescales, $\sim 0.1 \text{ m}$ accuracies are required at shallow depths, where part of these patterns emerge. It was suggested (Chapter 2; Grilli, 1998; Holland, 2001; Bell et al., 2004; Catálan and Haller, 2008; Yoo et al., 2011) that a model accounting for the wave amplitude can reduce the bias of bed estimates in shallow water. Using the model of Kirby and Dalrymple (1986), Catálan and Haller (2008) found that the errors at shallow depths reduced to $O(10\%)$ in a laboratory setting with regular waves. Herein, phase speeds were retrieved from optical data via trajectory tracking. In the field, phase speeds (or $\Omega-k$, where wave phase speed $c = \Omega/k$) is often retrieved with FFT- (Fast Fourier Transform) and CS- (cross-spectral) methods. Chapter 2 showed that a CS-method is preferred above a FFT-method where morphological scales decrease. When combining the CS-method with the model of Kirby and Dalrymple (1986), Figure 5.1 shows that bias indeed decreased in shallow water, from 31% to 6%, using a laboratory data set with detailed bed and water level measurements (De Bakker et al., 2015; Tissier et al., 2015). These percentages were computed as $(z_{b,est} - z_{b,true})/z_{b,true} \cdot 100$. Application of the same model on a field data set is less trivial, because it requires the cross-shore evolution of the wave height whereas often only an offshore value is available, as buoy measurement or node in a regional or global wave model (e.g. WaveWatch III). Potentially, the cross-shore evolution of the wave height can be predicted with a wave model. A set-up such as Yoo et al. (2011), using a model train to account for wave amplitude effects, is not feasible at km-scale field sites or for operational use because of high computational cost. Instead, a simple wave evolution model, such as Battjes-Janssen (Battjes and Janssen, 1978) can be used. The drawback is that such wave models require the bed profile. A possible solution is to first estimate the bed profile with the standard linear dispersion model, then use the estimates to predict the cross-shore evo-

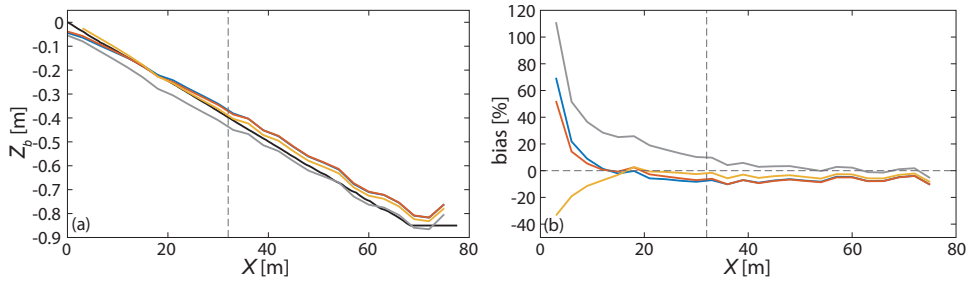


Figure 5.1: Bed elevation z_b (a) derived with the CS-method, using the linear dispersion model (grey) and the Kirby and Dalrymple (1986) model (blue, red, yellow) on a laboratory data set with detailed measurements of the bed (black) and the water surface. In the Kirby and Dalrymple (1986) model the wave height is included from lab measurements (blue), from predictions by the Battjes-Janssen wave model (red) and as an empirical constant representing the breaker wave height (yellow). In (b) the bias of estimated z_b from ground truth measurements is shown. The vertical dashed lines indicate the shallow water boundary.

lution of the wave height, and finally estimate the bed elevation again but more accurately with the model of Kirby and Dalrymple (1986). An alternative, simpler but probably less accurate, includes the application of a constant wave height in the model of Kirby and Dalrymple (1986), instead of its full cross-shore evolution. Hereto, the breaker wave height can be used, estimated from an offshore value H_{rms0} as $H_b = \gamma H_{rms0}$, wherein γ is an empirical coefficient that depends on the wave steepness. The latter approach is in line with Bell et al. (2004), who reduced the bias at shallow depth to -0.1 m by using the model of Booij (1981) (with $Z = 0.4H_s$). Using the laboratory data set of Figure 5.1, I tested whether bed elevation accuracies improve with the model of Kirby and Dalrymple (1986) using either wave information from the Battjes-Janssen model or a constant breaker wave height (wherein $\gamma = 0.72$, following Battjes and Stive (1985): $\gamma = 0.5 + 0.4 \tanh(16.5 H_{rms0} k_0 / \pi)$; Figure 5.1b). As a result, bias decreased from 31% (linear dispersion model) to 4% and -7% in shallow water. The constant breaker wave height gives rather accurate z_b , despite that the wave height was underestimated at large depths. This can be explained by the decreasing sensitivity of the model of Kirby and Dalrymple (1986) to the wave height with increasing depth.

A rather different approach comprises data assimilation methods. Those estimate bed elevation by minimising the misfit between an assimilation of observational data and the corresponding output of a numerical model, while recognising that both the observations and the model introduce errors. Van Dongeren et al. (2008) introduced a data assimilation routine using image-derived information on wave dissipation, wave phase speed and intertidal bed elevation. Wilson et al. (2014) used wave numbers, but also information on the shorelines and circulation patterns. Such a combination of image-derived information is beneficial to complex settings where waves and currents are both important, illustrated by Moghimi et al. (2016) who derived bed elevation in a tidal inlet through a data assimilation framework that used both the flow field and wave field. The strength of data assimilation methods is that both the numerical model and observational data do not have to be perfect. Also, inaccuracies introduced by a model that relates image-retrieved information to bed elevation can be avoided by assimilating on the image-retrieved information directly (e.g. wave numbers and currents, Wilson et al., 2014; Moghimi et al., 2016). However, data assimilation is computationally demanding compared to phase-speed methods, and the design of the math-

emational scheme remains a challenge (e.g. definition of the prior estimate, definition of the cost function and its solution).

Overall, further development of both the algorithms on phase-speed derived bed elevation as well as data assimilation schemes is crucial before they might replace *in situ* measurements. Meanwhile, collection of *in situ* data remains necessary to accurately monitor morphodynamics, and to validate the outcomes of the above-mentioned algorithms and data assimilation schemes.

5.2.2 Morphologic behaviour at different scales and their interaction

The surf zone possesses a variety of patterns at a range of scales. The meso-scale patterns focused on in this thesis are referred to as crescentic, based on the observed morphologic behaviour in the 2.4-year data set of daily video images. Chapter 3 showed that bar patterns mainly arose under near-normal angles, and shoreline patterns developed when bar patterns were pronounced. A distinct timing difference in the formation of patterns was found between the westerly and northerly oriented coastline of the Sand Engine, which related to the seasonal signal in the wave angle. In spring and summer, weeks of moderately energetic, northerly waves drove pattern formation at the northern side, while they had no substantial effect at the western side. In autumn and winter, energetic waves from southwestern to northwestern direction drove pattern formation at the western side, while they destructed patterns at the northern side.

Preliminary image analysis of 2015-2016 reveals rather different behaviour, with a larger complexity of patterns operating at multiple scales. Patterns in the shoreline at the northern side and the tip were no longer clearly related to a similar crescentic patterning in the sandbar. Instead, shoreline undulations arose from ridges of sand that propagated through the surf zone towards the beach and that finally welded ashore (Figure 5.2). The shoreward propagating ridges originated from the bar, whereon bent, finger-like features developed that lengthened with time. In Figure 5.2a-c, such a feature developed, detached and propagated onshore autonomously in several weeks time. These features have been observed before (Wijnberg and Holman, 2007; Almar et al., 2010; Price et al., 2017), and are also known as a Shoreward Propagating Accretionary Waves (SPAWs). In Figure 5.2d, a SPAW merged with the beach, creating a small undulation in the shoreline. The next day, a small bar emerged from the bar and attached to the beach with one of its ends, resulting in an obliquely-oriented bar (Figure 5.2f). In several days, the small bar detached, migrated onshore and welded to the beach (Figure 5.2g). The resulting shoreline undulation, grew and migrated down-drift (Figure 5.2h). The clearly different behaviour in 2015-2016 may be caused by changes in the wave conditions and the large-scale geometry of the Sand Engine. Wave conditions were extraordinary in terms of the angles, 53% came from the west-southwest compared to 46% in the period 2013-2015 (and 10-year wave climate). The large-scale geometry was distinctly different in planshape, i.e. the asymmetry A_s of the -1 m contour became rather large again (-0.41) whereas it had a decreasing trend towards a more symmetric planshape since construction of the Sand Engine (A_s -0.5 to -0.3). As a result, the local wave angles were distinctly different in the 2015-2016 time frame, with longer exposure to highly oblique waves at the northern side. Thus, the large-scale morphologic change (asymmetry) may have importantly affected the meso-scale morphologic change.

Although interaction between different scales can be expected at such complex sites, it is usually not acknowledged. In this thesis, for example, the impact of larger scale changes on meso-scale patterns was assumed small. The few characteristics (asymmetry, coastline orientation, cross-shore width Sand Engine; Figure 3.5) that were computed in Chapter 3 to

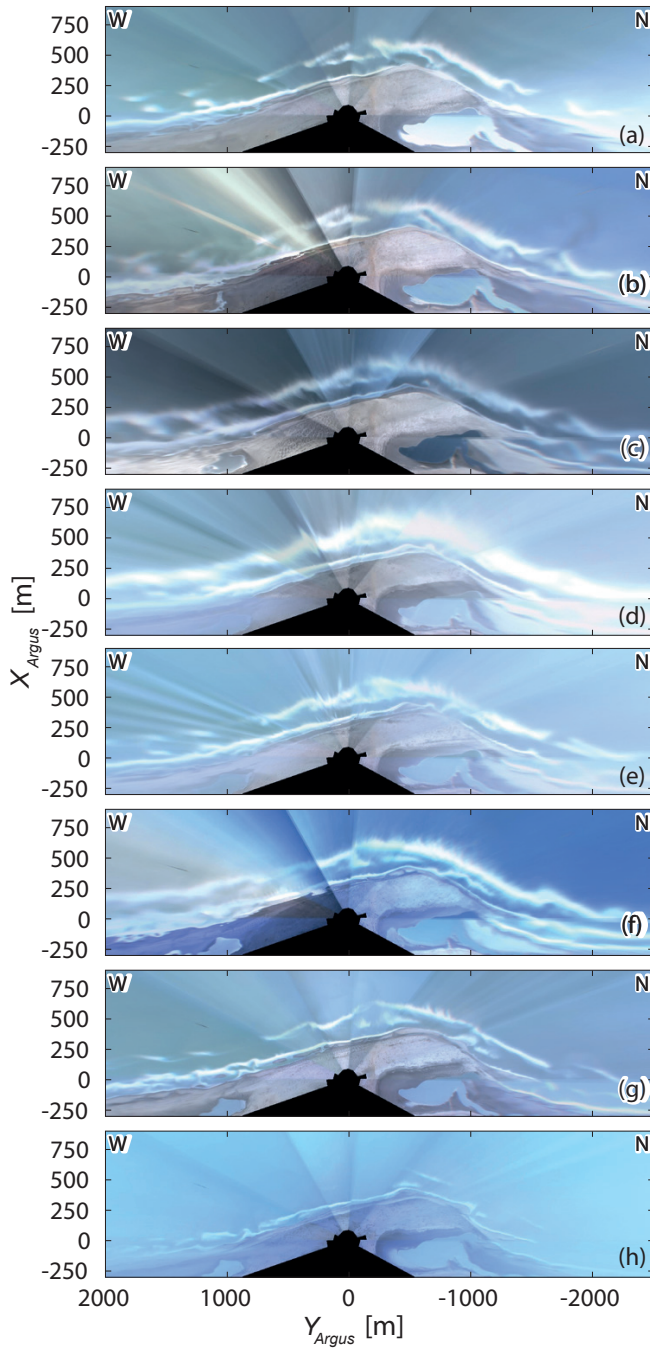


Figure 5.2: Time-averaged video images of the Sand Engine in 2015 on (a) 15 September, (b) 23 September, (c) 13 November, (d) 15 November, (e) 16 November, (f) 22 November, (g) 2 December, and (h) 7 December. The elongated white lines indicate the preferential location of wave breaking and approximate the location of the sandbar (outer line) and the shoreline (inner line). At $Y_{Argus} = -1000 \dots -500$ m an undulation developed in the shoreline.

quantify the large-scale, diffusive behaviour, illustrated that the large-scale change could be treated as a gradual background trend for the meso-scale behaviour. Chapter 3 suggested that alongshore differences in bar behaviour would gradually decrease with time, given that the alongshore variation in coastline orientation decreases with ongoing diffusion. However, this is contradicted by the observations in the 2015-2016 time frame, despite that the coastline orientations at the northern and western side converged. The Sand Engine seems rather sensitive to extraordinary wave conditions, acting on both large and meso scales. Another example where potential interaction between different scales was largely ignored, is provided by the studies on the large-scale diffusive behaviour of the Sand Engine (Stive et al., 2013; Luijendijk et al., 2017b). They assumed meso-scale behaviour to be unimportant (noise) and thus cross-shore processes, such as included in Chapter 4, were largely neglected in their modelling exercises. Such assumptions are valid if spatial or temporal scales of the different behaviours do not partly overlap or if additional functions of the site (recreation, nature development) are not at stake. If not, the features of interest can no longer be treated as being independent, and thus a multi-scale approach becomes essential. At the Sand Engine, its coastal protection function can be evaluated by modelling the large-scale diffusive behaviour of the nourishment on decadal timescales, but its recreational function demands a meso-scale approach to investigate whether sandbar patterns and their associated flows develop that are potentially hazardous to swimmers.

On the whole, I expect an increasing trend in coastal science towards multi-scale approaches, given the increasing interests to understand and manage complex coastal sites (e.g. km-scale nourishments, tidal inlets, estuaries) for multiple purposes. This once again highlights the need for multi-scale, and sufficiently accurate data sets (Section 6.2.1). In addition, numerical models are needed that can simulate dynamics at different scales and their interaction. Although this may currently seem infeasible, recent advances in model development (Dubarbier et al., 2017; Luijendijk et al., 2017a) demonstrate the potential. Whether this demands a model that can work accurately on all scales or a framework of models, each for a specific scale, is part of ongoing debate.

Appendix A

Accuracy of sandbar and shoreline positions

This is part of the publication: Rutten, J., B.G. Ruessink, and T.D. Price (2018), Observations on sandbar behaviour along a man-made curved coast. Earth Surface Processes and Landforms 43, 134-149.

In Chapter 3 we relied on the variability in the position and planshape of breaker lines in Argus imagery to quantify sandbar and shoreline behaviour. However, these breaker lines are only an indirect measure of the underlying sandbars. How accurate they approximate the position of the sandbar crest and the shoreline is unknown for our site. In this appendix we assess the accuracy of the breaker line method by comparison with *in situ* measurements.

Barline

Firstly, we determined the variability in cross-shore position of the barline from the *in situ* measured bar crest, under tide-induced water level fluctuations. We used a 31-day data set (March 2013) of 799 Argus images, sampled every 30 min during daylight, wherein 483 barlines were extracted at the western side and actual bar migration was limited (observed in *in situ* measurements). Bar crests were extracted from *in situ* measurements as the maximum perturbation in each shore-normal profile. With this technique, based on the method in Grunnet and Ruessink (2005), we can also evaluate characteristics of the platform-shaped sandbars at the northern side of the Sand Engine. Perturbation profiles were generated by subtracting a featureless profile, created for each profile using a loess filter (Plant et al., 2002) with a smoothing length $Lx = 125$ m, from the barred profile that was filtered for small-scale noise ($Lx = 50$ m). From all perturbations with a minimum height of 0.4 m and separated by at least 20 m, the most offshore perturbation (for $-5.5 \text{ m} < z < -1 \text{ m}$) was selected as the bar crest. Bar crest positions were checked visually, and were extracted manually when necessary. Then, the bias in mean cross-shore sandbar position was computed, $\Delta\mu(X_b) = \mu(X_{b,Argus}) - \mu(X_{b,in situ})$. For the 31-day study period, $\mu(X_{b,in situ})$ (2 surveys) was linearly interpolated over 799 time steps corresponding to the image sampling times. Figure A.1a shows a clear tidal dependency for the mean cross-shore barline position, consistent with Van Enckevort and Ruessink (2001). The barline shifted 9 m offshore during a 1 m decline in water level. This tide-induced variability in barline position can be removed by considering a selection of images during a single tidal level, following Van Enckevort and Ruessink (2001) and Ruessink et al. (2002). Here, we chose for low-tide images during which breaking is most pronounced, leaving us a data set of 778 images over the total 2.4-year period. An additional variability in barline position due to a water level fluctuation caused by the spring-neap cycle was smoothed by a Hanning filter with a window of 14.77 days (similar to Ruessink et al., 2002). No correction was performed for a potential wave-induced variability on X_b (Ribas et al., 2010; Pape et al., 2010), because local wave height and angle were not available. As

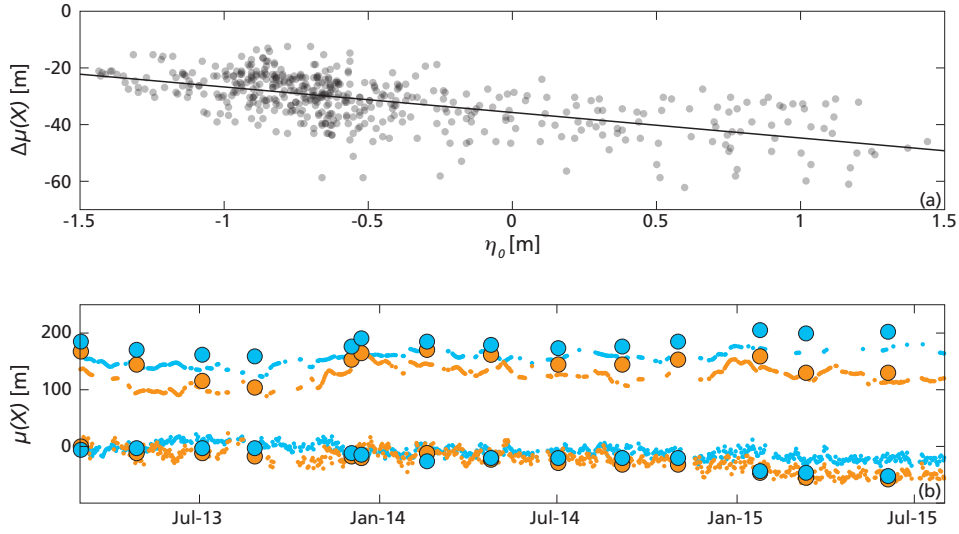


Figure A.1: Difference in mean cross-shore sandbar position (a), defined as $\Delta\mu(X) = \mu(X_{Argus}) - \mu(X_{in\ situ})$, during 31 days as a function of the offshore measured water level η_o . Mean position $\mu(X)$ (b) of the sandbar ($100 < \mu(X) < 200$ m) and Mean Low Water line ($-100 < \mu(X) < 0$ m) extracted from the video images (small dots) and compared with *in situ* measurements (large dots). Zero $\mu(X)$ represents the MLW line in March 2013, whereas orange indicates the northern side and blue the western side.

a result, the remaining variability in X_b on daily timescales may be wave-induced, whereas changes in X_b that persist for weeks to months are assumed to reflect behavioural dynamics of the sandbar itself.

Secondly, we determined the remaining bias, $\Delta\mu(X_b)$, and the root-mean-square error, ε_{RMS} , after removing the tide-induced variability in cross-shore barline position within the 2.4-year data set. *In situ* bar crests were extracted from 14 surveys. We found that the barline was generally located shoreward (negative $\Delta\mu(X_b)$) of the measured bar crest at $O(10$ m) (Table A.1; Figure A.1b), in line with the findings of Van Enckevort and Ruessink (2001). Slightly higher $\Delta\mu(X_b)$ and ε_{RMS} can be observed at the western side compared to the northern side, which can possibly be explained by different bar crest depth and bar shape at either side (see Van Enckevort and Ruessink, 2001; Ribas et al., 2010). Similarly, the temporal variability in $\Delta\mu(X_b)$ (Figure A.1b) may be explained by time variations in bar crest depth and bar shape.

To conclude, at our site the outer breaker line in video imagery approaches the sandbar crest position with an $O(10$ m) accuracy, when accounting for tide-induced variability, and thus, given the larger actual variability in sandbar position (see Figure A.1b), we reason that we may safely use the breaker line method to quantify sandbar behaviour here.

Shoreline

Prior to assessing the accuracy of the mean cross-shore position of the shoreline with *in situ* measurements, two methodological steps were needed to limit tide- and wave-induced shifting of the shoreline. Firstly, the water level elevation was estimated corresponding to each extracted shoreline, using the correction model of Aarninkhof et al. (2003). Accordingly,

water level elevation was computed for each extracted shoreline, z_s , as

$$z_s = z_o + \eta_s + 0.5K_{osc}\eta_{osc}, \quad (\text{A.1})$$

with offshore water level z_o , wave-setup η_s , a constant empirical coefficient K_{osc} , and swash-height η_{osc} . Model input terms were computed from measured tide and wave statistics (see Section 3.2.2). For further details on the model we refer to Aarninkhof et al. (2003). Following Plant et al. (2007), K_{osc} was adjusted from 1.2 (default) to -0.48 , to optimise the fit for shorelines based on breaker lines instead of colour differences (hue, saturation, value) as in Aarninkhof et al. (2003). Secondly, shorelines were translated to the Mean Low Water line, at -0.68 m MSL, given the elevation and cross-shore position of each shoreline, and assuming an alongshore-uniform beach slope of 0.03. From the *in situ* measurements, the MLW line was simply extracted as the corresponding elevation contour. We found that the shoreline showed generally a small seaward offset (Table A.1; Figure A.1b). Shorelines at the western side had a slightly larger $\Delta\mu(X_s)$ and ε_{RMS} compared to the northern side. Possibly, the offset of X_s can be explained by deviations in the beach face slope from the assumed 0.03 (Figure A.1b), as used in the model, or by uncertainty in the value of K_{osc} .

Altogether, given the ~ 10 m accuracy of video-derived shorelines at our site, we may rely on the breaker line method to quantify and describe shoreline behaviour.

Table A.1: Bias, defined as $\Delta\mu(X) = \mu(X_{Argus}) - \mu(X_{in\ situ})$, and root-mean-square error, ε_{RMS} , in mean position of the sandbar X_b and the shoreline X_s derived from Argus video and *in situ* measurements at the Sand Engine

	North side	West side
$\Delta\mu(X_b)$	-21 m	-25 m
$\varepsilon_{RMS} X_b$	26 m	39 m
$\Delta\mu(X_s)$	4 m	13 m
$\varepsilon_{RMS} X_s$	10 m	18 m

References

- Aagaard, T., J. Nielsen, S. G. Jensen, and J. Friderichsen (2004). Longshore sediment transport and coastal erosion at Skallingen, Denmark. *Geografisk Tidsskrift-Danish Journal of Geography* 104(1), pp. 5–14.
- Aagaard, T. and A. Kroon (2007). Mesoscale behaviour of longshore bars — Net Onshore or Net Offshore Migration. In: *Proceedings of Coastal Sediments 2007*, pp. 2124–2136.
- Aarninkhof, S. G. J., I. L. Turner, T. D. T. Dronkers, M. Caljouw, and L. Nipius (2003). A video-based technique for mapping intertidal beach bathymetry. *Coastal Engineering* 49(4), pp. 275–289.
- Almar, R., B. Castelle, B. G. Ruessink, N. Sénéchal, P. Bonneton, and V. Marieu (2010). Two- and three-dimensional double-sandbar system behaviour under intense wave forcing and a meso-macro tidal range. *Continental Shelf Research* 30(7), pp. 781–792.
- Arriaga, J., J. Rutten, F. Ribas, A. Falqués, and B. G. Ruessink (2017). Modeling the long-term diffusion and feeding capability of a mega-nourishment. *Coastal Engineering* 121, pp. 1–13.
- Ashton, A. D., A. B. Murray, and O. Arnault (2001). Formation of coastline features by large-scale instabilities induced by high-angle waves. *Nature* 414, pp. 296–300.
- Ashton, A. D. and A. B. Murray (2006). High-angle wave instability and emergent shoreline shapes: 1. Modeling of sand waves, flying spits, and capes. *Journal of Geophysical Research* 111(F04011). DOI:10.1029/2005JF000422.
- Ashton, A. D. and L. Giosan (2011). Wave-angle control of delta evolution. *Geophysical Research Letters* 38(L13405). DOI:10.1029/2011GL047630.
- Backstrom, J. T., D. W. T. Jackson, J. A. G. Cooper, and G. C. Malvárez (2008). Storm-driven shoreface morphodynamics on a low-wave energy delta: the role of nearshore topography and shoreline orientation. *Journal of Coastal Research* 24(6), pp. 1379–1387.
- Bakker, J. P., A. C. W. Baas, J. Bartholdy, L. Jones, B. G. Ruessink, S. Temmerman, and M. Van de Pol (2016). Environmental impacts-Coastal ecosystems. In: *North Sea Region Climate Change Assessment. Regional Climate Studies*. Ed. by M Quante and F Colijn. Cham: Springer, pp. 275–314.
- Battjes, J. A. and J. P. F. M. Janssen (1978). Energy loss and set-up due to breaking of random waves. In: *Proceedings of Coastal Engineering*, pp. 569–587.
- Battjes, J. A. and M. J. F. Stive (1985). Calibration and verification of a dissipation model for random breaking waves. *Journal of Geophysical Research: Oceans* 90(C5), pp. 9159–9167.
- Bell, P. S. (1999). Shallow water bathymetry derived from an analysis of X-band marine radar images of waves. *Coastal Engineering* 37(3-4), pp. 513–527.
- Bell, P. S. (2001). Determination of Bathymetry Using Marine Radar Images of Waves. In: *Fourth international symposium on Ocean Wave Measurement and Analysis*. Reston, VA: American Society of Civil Engineers, pp. 251–257.
- Bell, P. S. (2002). The use of X-band marine radar at Egmond. In: *Coast 3D-Egmond*. Ed. by L. C. Van Rijn, B. G. Ruessink, and J. P. M. Mulder. Aqua Publications, Q1–Q13.
- Bell, P. S., J. J. Williams, S. Clark, B. D. Morris, and A. Vila-Concejo (2004). Nested radar systems for remote coastal observations. *Journal of Coastal Research* SI 39 (Proceedings of the 8th International Coastal Symposium), pp. 438–387.
- Bell, P., C. Bird, and A. Plater (2016). A temporal waterline approach to mapping intertidal areas using X-band marine radar. *Coastal Engineering* 107, pp. 84–101.

- Bergsma, E., D. Conley, M. Davidson, and T. O'Hare (2016). Video-based nearshore bathymetry estimation in macro-tidal environments. *Marine Geology* 374, pp. 31–41.
- Bird, E. (2000). Beaches. In: *Coastal Geomorphology: an introduction*. Chichester, UK and Hoboken, NJ, USA: John Wiley & Sons. Chap. Beaches, p. 411.
- Birkemeier, W. A. and C. Mason (1984). The CRAB: a unique nearshore surveying vehicle. *Journal of Surveying Engineering* 110.1, pp. 1–7.
- Blossier, B., K. R. Bryan, C. J. Daly, and C. Winter (2016). Nearshore sandbar rotation at single-barred embayed beaches. *Journal of Geophysical Research: Oceans* 121. DOI:10.1002/2015JC011031.
- Booij, N. (1981). Gravity waves on water with non-uniform depth and current. PhD thesis. TU Delft, p. 139.
- Booij, N., R. C. Ris, and L. H. Holthuijsen (1999). A third-generation wave model for coastal regions 1. Model description and validation. *Journal of Geophysical Research* 104(C4), pp. 7649–7666.
- Brière, C., S. K. Janssen, A. P. Oost, M. Taal, and P. K. Tonnon (2017). Usability of the climate-resilient nature-based sand motor pilot, The Netherlands. *Journal of Coastal Conservation*, pp. 1–12.
- Bryan, K. R., R. Foster, and I. MacDonald (2013). Beach rotation at two adjacent headland-enclosed beaches. *Journal of Coastal Research* SI 65, pp. 2095–2100.
- Calvete, D., N. Dodd, A. Falqués, and S. M. van Leeuwen (2005). Morphological development of rip channel systems: Normal and near-normal wave incidence. *Journal of Geophysical Research: Oceans* 110(C10006. DOI:10.1029/2004JC002803.
- Calvete, D., G. Coco, A. Falqués, and N. Dodd (2007). (Un)predictability in rip channel systems. *Geophysical Research Letters* 34(L05605). DOI:10.1029/2006GL028162.
- Castelle, B., P. Bonneton, H. Dupuis, and N. Sénéchal (2007). Double bar beach dynamics on the high-energy meso-macrotidal French Aquitanian Coast : A review. *Marine Geology* 245, pp. 141–159.
- Castelle, B., B. G. Ruessink, P. Bonneton, V. Marieu, N. Bruneau, and T. D. Price (2010). Coupling mechanisms in double sandbar systems. Part 1: Patterns and physical explanation. *Earth Surface Processes and Landforms* 35(4), pp. 476–486.
- Castelle, B. and B. G. Ruessink (2011). Modeling formation and subsequent nonlinear evolution of rip channels : Time-varying versus time-invariant wave forcing. *Journal of Geophysical Research* 116(F04008). DOI:10.1029/2011JF001997.
- Castelle, B. and G. Coco (2012). The morphodynamics of rip channels on embayed beaches. *Continental Shelf Research* 43, pp. 10–23.
- Castelle, B., V. Marieu, G. Coco, P. Bonneton, N. Bruneau, and B. G. Ruessink (2012). On the impact of an offshore bathymetric anomaly on surf zone rip channels. *Journal of Geophysical Research: Earth Surface* 117(F01038. DOI:10.1029/2011JF002141.
- Castelle, B., V. Marieu, S. Bujan, K. D. Splinter, A. Robinet, N. Sénéchal, and S. Ferreira (2015). Impact of the winter 2013–2014 series of severe Western Europe storms on a double-barred sandy coast: beach and dune erosion and megacusp embayments. *Geomorphology* 238, pp. 135–148.
- Castelle, B., T. Scott, R. W. Brander, and R. J. McCarroll (2016). Rip current types, circulation and hazard. *Earth-Science Reviews* 163, pp. 1–21.
- Catalán, P. A. and M. C. Haller (2008). Remote sensing of breaking wave phase speeds with application to non-linear depth inversions. *Coastal Engineering* 55(1), pp. 93–111.
- Chatzistratis, D. (2014). Estimation of nearshore bathymetry using Argus images: Improving cBathy in shallow water. Internship report. Deltares, p. 53.
- Chong, T. Y. (2014). Assessment of beach states at the Sand Motor on the basis of alongshore variability in bathymetry data. MSc Thesis. TU Delft, p. 103.
- Coco, G. and A. B. Murray (2007). Patterns in the sand: From forcing templates to self-organization. *Geomorphology* 91(3–4), pp. 271–290.
- Contardo, S. and G. Symonds (2015). Sandbar straightening under wind-sea and swell forcing. *Marine Geology* 368, pp. 25–41.
- Davidson-Arnott, R. G. D. and A. G. Van Heyningen (2003). Migration and sedimentology of longshore sandwaves, Long Point, Lake Erie, Canada. *Sedimentology* 50(6), pp. 1123–1137.

- De Bakker, A. T. M., T. H. C. Herbers, P. B. Smit, M. F. S. Tissier, and B. G. Ruessink (2015). Non-linear Infragravity–Wave Interactions on a Gently Sloping Laboratory Beach. *Journal of Physical Oceanography* 45(2), pp. 589–605.
- De Schipper, M. A., S. De Vries, R. Ranasinghe, A. J.H. M. Reniers, and M. J. F. Stive (2013). Along-shore topographic variability at a nourished beach. In: *Proceedings 7th International Conference on Coastal Dynamics*, pp. 499–510.
- De Schipper, M. A., S. De Vries, B. G. Ruessink, R. C. De Zeeuw, J. Rutten, C. Van Gelder-Maas, and M. J. F. Stive (2016). Initial spreading of a mega feeder nourishment: observations of the Sand Engine pilot project. *Coastal Engineering* 111, pp. 23–38.
- De Vriend, H. J. and M. Van Koningsveld (2012). *Building with Nature: Thinking, acting and interacting differently*. Dordrecht, The Netherlands: Ecoshape, Building with Nature, p. 39.
- De Winter, R. C. and B. G. Ruessink (2017). Sensitivity analysis of climate change impacts on dune erosion: case study for the Dutch Holland coast. *Climatic Change* 141(4), pp. 685–701.
- Doody, P., M. Ferreira, S. Lombardo, I. Lucius, R. Misdorp, H. Niesing, A. Salman, and M. Smallegange (2004). *Living with coastal erosion in Europe*. Tech. rep. Schiedam: European Commission, p. 21.
- Drønen, N. and R. Deigaard (2007). Quasi-three-dimensional modelling of the morphology of long-shore bars. *Coastal Engineering* 54(3), pp. 197–215.
- Dubarbier, B., B. Castelle, V. Marieu, and B. G. Ruessink (2015). Process-based modeling of cross-shore sandbar behavior. *Coastal Engineering* 95, pp. 35–50.
- Dubarbier, B., B. Castelle, B. G. Ruessink, and V. Marieu (2017). Mechanisms controlling the complete accretionary beach state sequence. *Geophysical Research Letters* 44, pp. 5645–5654.
- Dugan, J. P., C. C. Piotrowski, and J. Z. Williams (2001). Water depth and surface current retrievals from airborne optical measurements of surface gravity wave dispersion. *Journal of Geophysical Research* 106, pp. 16903–16915.
- Dugan, J. P. and C. C. Piotrowski (2003). Surface current measurements using airborne visible image time series. *Remote Sensing of Environment* 84(2), pp. 309–319.
- Elgar, S., E. L. Gallagher, and R. T. Guza (2001). Nearshore sandbar migration. *Journal of Geophysical Research* 106(C6), pp. 11623–11627.
- Falqués, A., G. Coco, and D. A. Huntley (2000). A mechanism for the generation of wave-driven rhythmic patterns in the surf zone. *Journal of Geophysical Research* 105(C10), pp. 24087–24971.
- Gallagher, E. L., S. Elgar, and R. T. Guza (1998). Observations of sand bar evolution on a natural beach. *Journal of Geophysical Research* 103(C2), pp. 3203–3215.
- Gallop, S. L., K. R. Bryan, G. Coco, and S. A. Stephens (2011). Storm-driven changes in rip channel patterns on an embayed beach. *Geomorphology* 127(3), pp. 179–188.
- Garcia, I., G. Serafy, A. Heemink, and H. Schuttelaars (2013). Towards a data assimilation system for morphodynamic modeling: bathymetric data assimilation for wave property estimation. *Ocean Dynamics* 63(5), pp. 489–505.
- Garnier, R., D. Calvete, A. Falques, and M. Caballeria (2006). Generation and nonlinear evolution of shore oblique / transverse sand bars. *Journal of Fluid Mechanics* 567, pp. 327–360.
- Garnier, R., N. Dodd, A. Falqués, and D. Calvete (2010). Mechanisms controlling crescentic bar amplitude. *Journal of Geophysical Research* 115(F02007). DOI:10.1029/2009JF001407.
- Garnier, R., A. Falqués, D. Calvete, J. Thiébot, and F. Ribas (2013). A mechanism for sandbar straightening by oblique wave incidence. *Geophysical Research Letters* 40, pp. 2726–2730.
- Garrett, C. and C. Toulany (1981). Variability of the flow through the Strait of Belle Isle. *Journal of Marine Research* 39(1), pp. 163–189.
- Grilli, S. T. (1998). Depth inversion in shallow water based on nonlinear properties of shoaling periodic waves. *Coastal Engineering* 35(3), pp. 185–209.
- Grunnet, N. M. and P. Hoekstra (2004). Alongshore variability of the multiple barred coast of Ter-schelling, The Netherlands. *Marine Geology* 203, pp. 23–41.
- Grunnet, N. M. and B. G. Ruessink (2005). Morphodynamic response of nearshore bars to a shoreface nourishment. *Coastal Engineering* 52(2), pp. 119–137.

- Hamm, L., M. Capobianco, H. H. Dette, A. Lechuga, R. Spanhoff, and M. J. F. Stive (2002). A summary of European experience with shore nourishment. *Coastal Engineering* 47(2), pp. 237–264.
- Harley, M. D., I. L. Turner, and A. D. Short (2015). New insights into embayed beach rotation: The importance of wave exposure and cross-shore processes. *Journal of Geophysical Research: Earth Surface* 120, pp. 1470–1484.
- Hino, M. (1974). Theory on formation of rip-current and cuspidal coast. In: *14th Conference on Coastal Engineering*. New York: Am. Soc. of Civ. Eng., pp. 901–919.
- Hoefel, F. and S. Elgar (2003). Wave-Induced Sediment Transport and Sandbar Migration. *Science* 299(5614), pp. 1885–1887.
- Holland, T. K., R. A. Holman, T. C. Lippmann, J. Stanley, and N. G. Plant (1997). Practical use of video imagery in nearshore oceanographic field studies. *IEEE Journal of Oceanic Engineering* 22(1), pp. 81–92.
- Holland, T. K. (2001). Application of the linear dispersion relation with respect to depth inversion and remotely sensed imagery. *IEEE Transactions on Geoscience and Remote Sensing* 39(9), pp. 2060–2071.
- Holman, R. A. (2001). Pattern formation in the nearshore. In: *River, Coastal and Estuarine Morphodynamics*. Springer Berlin Heidelberg, pp. 141–162.
- Holman, R. A., G. Symonds, E. B. Thornton, and R. Ranasinghe (2006). Rip spacing and persistence on an embayed beach. *Journal of Geophysical Research: Oceans* 111. DOI:10.1029/2005JC002965.
- Holman, R. A. and J. Stanley (2007). The history and technical capabilities of Argus. *Coastal Engineering* 54, pp. 477–491.
- Holman, R. A. and M. C. Haller (2013). Remote sensing of the nearshore. *Annual Review of Marine Science* 5, pp. 95–113.
- Holman, R. A., N. G. Plant, and T. Holland (2013). cBathy: A robust algorithm for estimating nearshore bathymetry. *Journal of Geophysical Research: Oceans* 118(5), pp. 2595–2609.
- Hsu, T., S. Elgar, and R. T. Guza (2006). Wave-induced sediment transport and onshore sandbar migration. *Coastal Engineering* 53, pp. 817–824.
- Hsu, T., T. Lin, and I. Tseng (2007). Human Impact on Coastal Erosion in Taiwan. *Journal of Coastal Research* 23(4), pp. 961–973.
- Jimenez, J. A., V. Gracia, H. I. Valdemoro, E. T. Mendoza, and A. Sanchez-Arcilla (2011). Managing erosion-induced problems in NW Mediterranean urban beaches. *Ocean and Coastal Management* 54(12), pp. 907–918.
- Kabat, P., L. O. Fresco, M. J. F. Stive, C. P. Veerman, J. S.L. J. van Alphen, B. W.A. H. Parmet, W. Hazeleger, and C. A. Katsman (2009). Dutch coasts in transition. *Nature Geoscience* 2(7), pp. 450–452.
- Kalman, R. E. (1960). A new approach to linear filtering and prediction problems. *Journal of Basic Engineering* 82(1), pp. 35–45.
- King, C. A. M. and W. W. Williams (1949). The Formation and Movement of Sand Bars by Wave Action. *The Geographical Journal* 113, pp. 70–85.
- Kirby, J. and R. Dalrymple (1986). An approximate model for nonlinear dispersion in monochromatic wave propagation models. *Coastal Engineering* 9, pp. 545–561.
- Komar, P. D. (1976). *Beach processes and sedimentation*. New York: Prentice Hall, p. 429.
- Konicki, K. M. and R. A. Holman (2000). The statistics and kinematics of transverse sand bars on an open coast. *Marine Geology* 169, pp. 69–101.
- Kroon, A. et al. (2007). Application of remote sensing video systems to coastline management problems. *Coastal Engineering* 54(6-7), pp. 493–505.
- Lippmann, T. C. and R. A. Holman (1989). Quantification of sand bar morphology: A video technique based on wave dissipation. *Journal of Geophysical Research* 94(C1), pp. 995–1011.
- Lippmann, T. C. and R. A. Holman (1990). The spatial and temporal variability of sand bar morphology. *Journal of Geophysical Research* 95(C7), pp. 11575–11590.

- Luijendijk, A. P., R. Velhorst, B. Hoonhout, S. De Vries, and R. Ranasinghe (2017a). Integrated modelling of the morphological evolution of the Sand Engine mega-nourishment. In: *Proceedings of Coastal Dynamics 2017*, pp. 1874–1885.
- Luijendijk, A. P., R. Ranasinghe, M. A. De Schipper, B. A. Huisman, C. M. Swinkels, D. J. R. Walstra, and M. J. F. Stive (2017b). The initial morphological response of the Sand Engine: A process-based modelling study. *Coastal Engineering* 119, pp. 1–14.
- Lushine, J. B. (1991). A study of rip current drownings and related weather factors. *National Weather Digest Beach* 16, pp. 13–19.
- MacMahan, J. H. (2001). Hydrographic surveying from personal watercraft. *Journal of Surveying Engineering* 127(1), pp. 12–24.
- McCarrroll, R. J., R. W. Brander, I. L. Turner, and B. Van Leeuwen (2016). Shoreface storm morphodynamics and mega-rip evolution at an embayed beach: Bondi Beach, NSW, Australia. *Continental Shelf Research* 116, pp. 74–88.
- Merrifield, M. A. and R. T. Guza (1990). Detecting propagating signals with complex empirical orthogonal functions: A cautionary note. *Journal of Physical Oceanography* 20, pp. 1628–1633.
- Moghimi, S., H. T. Özkan-Haller, G. W. Wilson, and A. Kurapov (2016). Data assimilation for bathymetry estimation at a tidal inlet. *Journal of Atmospheric and Oceanic Technology* 33(10), pp. 2145–2163.
- Morris, J. (2013). Estimation of the Nearshore Bathymetry using Remote Sensing Techniques. MSc thesis. TU Delft, p. 132.
- Morton, R. A. and A. H. J. Sallenger (2003). Morphological Impacts of Extreme Storms on Sandy Beaches and Barriers. *Journal of Coastal Research* 19(3), pp. 560–573.
- Mosterdijk, G. and H. Miller (2008). *SeaDarQ Validation Report*. Tech. rep. November. Dutch Ministry of Water and Traffic Management, p. 11.
- Nieto Borge, J. C., G. R. Rodríguez Rodríguez, K. Hessner, and P. Izquierdo González (2004). Inversion of marine radar images for surface wave analysis. *Journal of Atmospheric and Oceanic Technology* 21, pp. 1291–1300.
- Ojeda, E., B. G. Ruessink, and J. Guillen (2008). Morphodynamic response of a two-barred beach to a shoreface nourishment. *Coastal Engineering* 55(12), pp. 1185–1196.
- Ojeda, E., J. Guillén, and F. Ribas (2011). Dynamics of single-barred embayed beaches. *Marine Geology* 280(1-4), pp. 76–90.
- Pape, L., N. G. Plant, and B. G. Ruessink (2010). On cross-shore migration and equilibrium states of nearshore sandbars. *Journal of Geophysical Research* 115. DOI:10.1029/2009JF001501.
- Phillips, O. M. (1977). *The dynamics of the upper ocean*. Cambridge: Cambridge University Press.
- Pianca, C., R. A. Holman, and E. Siegle (2015). Shoreline variability from days to decades: Results of long-term video imaging. *Journal of Geophysical Research: Oceans* 120, pp. 2159–2178.
- Piotrowski, C. C. and J. P. Dugan (2002). Accuracy of bathymetry and current retrievals from airborne optical time-series imaging of shoaling waves. *IEEE Transactions on Geoscience and Remote Sensing* 40(12), pp. 2606–2618.
- Plant, N. G., R. A. Holman, M. H. Freilich, and W. A. Birkemeier (1999). A simple model for interannual sandbar behavior. *Journal of Geophysical Research* 104(C7), pp. 15755–15776.
- Plant, N. G., K. T. Holland, and J. A. Puleo (2002). Analysis of the scale of errors in nearshore bathymetric data. *Marine Geology* 191, pp. 71–86.
- Plant, N. G., K. T. Holland, and R. A. Holman (2006). A dynamical attractor governs beach response to storms. *Geophysical Research Letters* 33(L17607). DOI:10.1029/2006GL027105.
- Plant, N. G., S. G. J. Aarninkhof, I. L. Turner, and K. S. Kingston (2007). The performance of shoreline detection models applied to video imagery. *Journal of Coastal Research* 23(2), pp. 658–670.
- Plant, N. G., K. T. Holland, and M. C. Haller (2008). Ocean Wavenumber Estimation From Wave-Resolving Time Series Imagery. *IEEE Transactions on Geoscience and Remote Sensing* 46(9), pp. 2644–2658.

- Pope, J. (1997). Responding to Coastal Erosion and Flooding Damages. *Journal of Coastal Research* 13(3), pp. 704–710.
- Price, T. D. and B. G. Ruessink (2011). State dynamics of a double sandbar system. *Continental Shelf Research* 31, pp. 659–674.
- Price, T. D. and B. G. Ruessink (2013). Observations and conceptual modelling of morphological coupling in a double sandbar system. *Earth Surface Processes and Landforms* 38(5), pp. 477–489.
- Price, T. D., B. Castelle, R. Ranasinghe, and B. G. Ruessink (2013). Coupled sandbar patterns and obliquely incident waves. *Journal of Geophysical Research: Earth Surface* 118(3), pp. 1677–1692.
- Price, T. D., N. van Kuik, L. de Wit, S. Ant3nia, and B. Ruessink (2017). Shoreward propagating accretionary waves (SPAWs): observations from a multiple sandbar system. In: *Proceedings of Coastal Dynamics 2017*, pp. 1081–1089.
- Quartel, S., A. Kroon, and B. G. Ruessink (2008). Seasonal accretion and erosion patterns of a microtidal sandy beach. *Marine Geology* 250(1-2), pp. 19–33.
- Radermacher, M., M. A. de Schipper, C. Swinkels, J. H. Macmahan, and A. J.H. M. Reniers (2017). Tidal flow separation at protruding beach nourishments. *Journal of Geophysical Research: Oceans* 122. DOI:10.1002/2016JC011942.
- Ranasinghe, R. (2016). Assessing climate change impacts on open sandy coasts: A review. *Earth-Science Reviews* 160, pp. 320–332.
- Ranasinghe, R., G. Symonds, K. Black, and R. A. Holman (2004a). Morphodynamics of intermediate beaches: A video imaging and numerical modelling study. *Coastal Engineering* 51(7), pp. 629–655.
- Ranasinghe, R., R. McLoughlin, A. Short, and G. Symonds (2004b). The Southern Oscillation Index, wave climate, and beach rotation. *Marine Geology* 204(3-4), pp. 273–287.
- Ribas, F. and A. Kroon (2007). Characteristics and dynamics of surfzone transverse finger bars. *Journal of Geophysical Research* 112(F03028. DOI:10.1029/2006JF000685.
- Ribas, F., E. Ojeda, T. D. Price, and J. Guill3n (2010). Assessing the Suitability of Video Imaging for Studying the Dynamics of Nearshore Sandbars in Tideless Beaches. *IEEE Transactions on Geoscience and Remote Sensing* 48(6), pp. 2482–2497.
- Ribas, F., A. Doeschate, H. E. de Swart, B. G. Ruessink, and D. Calvete (2014). Observations and modeling of surf zone transverse finger bars at the Gold Coast, Australia. *Ocean Dynamics* 64, pp. 1193–1207.
- Roelvink, J. A., A. J.H. M. Reniers, A. van Dongeren, J. S. M. van Thiel de Vries, R. T. McCall, and J. M. Lescinski (2009). Modelling storm impacts on beaches, dunes and barrier islands. *Coastal Engineering* 56(11-12), pp. 1133–1152.
- Ruessink, B. G., I. M. J. van Enckevort, K. S. Kingston, and M. A. Davidson (2000). Analysis of observed two- and three-dimensional nearshore bar behaviour. *Marine Geology* 169(1-2), pp. 161–183.
- Ruessink, B. G., P. S. Bell, I. M. J. Van Enckevort, and S. G. J. Aarninkhof (2002). Nearshore bar crest location quantified from time-averaged X-band radar images. *Coastal Engineering* 45(1), pp. 19–32.
- Ruessink, B. G., D. J. Walstra, and H. N. Southgate (2003). Calibration and verification of a parametric wave model on barred beaches. *Coastal Engineering* 48(3), pp. 139–149.
- Ruessink, B. G., G. Coco, R. Ranasinghe, and I. L. Turner (2007). Coupled and noncoupled behavior of three-dimensional morphological patterns in a double sandbar system. *Journal of Geophysical Research: Oceans* 112. DOI:10.1029/2006JC003799.
- Ruessink, B. G., L. Pape, and I. L. Turner (2009). Daily to interannual cross-shore sandbar migration: Observations from a multiple sandbar system. *Continental Shelf Research* 29(14), pp. 1663–1677.
- Ruessink, B. G., G. Ramaekers, and L. C. Van Rijn (2012). On the parameterization of the free-stream non-linear wave orbital motion in nearshore morphodynamic models. *Coastal Engineering* 65, pp. 56–63.
- Ruggiero, P., G. M. Kaminsky, G. Gelfenbaum, and B. Voigt (2005). Seasonal to Interannual Morphodynamics along a High-Energy Dissipative Littoral Cell. *Journal of Coastal Research* 21(3), pp. 553–578.

- Rutten, J., B. Dubarbier, T. D. Price, B. Castelle, and B. G. Ruessink (2017). Crescentic bar patterns along curved coasts: observations and modelling. In: *Proceedings of Coastal Dynamics 2017*, pp. 1832–1842.
- Rutten, J., B. G. Ruessink, and T. D. Price (2018). Observations on sandbar behaviour along a man-made curved coast. *Earth Surface Processes and Landforms* 43, pp. 134–149.
- Sallenger, A. H. J. (2000). Storm impact scale for barrier islands. *Journal of Coastal Research* 16(3), pp. 890–895.
- Sallenger, A. H. J., R. A. Holman, and W. A. Birkemeier (1985). Storm-induced response of a nearshore-bar system. *Marine Geology* 64, pp. 237–257.
- Senet, C. M., J. Seemann, S. Flampouris, and F. Ziemer (2008). Determination of bathymetric and current maps by the method DiSC based on the analysis of nautical X-band radar image sequences of the sea surface (November 2007). *IEEE Transactions on Geoscience and Remote Sensing* 46(8), pp. 2267–2279.
- Short, A. D. (1978). Wave power and beach stages: a global model. In: *Proceedings of Coastal Engineering*, pp. 1145–1162.
- Short, A. D. and C. L. Hogan (1994). Rip currents and beach hazards: their impact on public safety and implications for coastal management. *Journal of Coastal Research* SI 12, pp. 197–209.
- Silva, F. G., P. H. Gomes de Oliveira Sousa, and E. Siegle (2016). Longshore transport gradients and erosion processes along the Ilha Comprida (Brazil) beach system. *Ocean Dynamics* 66, pp. 853–865.
- Sonu, C. J. (1973). Three-dimensional beach changes. *The Journal of Geology* 81, pp. 42–64.
- Splinter, K. D., R. A. Holman, and N. G. Plant (2011). A behavior-oriented dynamic model for sandbar migration and 2DH evolution. *Journal of Geophysical Research: Oceans* 116(1). DOI:10.1029/2010JC006382.
- Stewart, C. J. and R. G. D. Davidson-Arnott (1988). Morphology, formation and migration of longshore sandwaves; Long Point, Lake Erie, Canada. *Marine Geology* 81(1-4), pp. 63–77.
- Stive, M. J. F. (1984). Energy dissipation in waves breaking on gentle slopes. *Coastal Engineering* 8, pp. 99–127.
- Stive, M. J. F. et al. (2013). A New Alternative to Saving Our Beaches from Sea-Level Rise: The Sand Engine. *Journal of Coastal Research* 290, pp. 1001–1008.
- Stockdon, H. F. and R. A. Holman (2000). Estimation of wave phase speed and nearshore bathymetry from video imagery. *Journal of Geophysical Research* 105, pp. 15–22.
- Swinkels, C., H. Peters, and J. Van Heesen (2012). Analysis of current patterns in coastal areas using X-band radar images. *Proceedings of Coastal Engineering*, pp. 1–10.
- Taal, M. D., M. A. M. Löffler, C. T. M. Vertegaal, J. W. M. Wijsman, L. Van der Valk, and P. K. Tonnon (2016). *Development of the Sand Motor. Concise report describing the first four years of the monitoring and evaluation Programme (MEP)*. Tech. rep. Deltares, p. 62.
- Temmerman, S., P. Meire, T. J. Bouma, P. M. J. Herman, T. Ysebaert, and H. J. De vried (2013). Ecosystem-based coastal defence in the face of global change. *Nature* 504, pp. 79–83.
- Thiébot, J., D. Idier, R. Garnier, A. Falqués, and B. G. Ruessink (2012). The influence of wave direction on the morphological response of a double sandbar system. *Continental Shelf Research* 32, pp. 71–85.
- Thornton, E. B. and R. T. Humiston (1996). Bar / trough generation on a natural beach. *Journal of Geophysical Research* 101(96), pp. 12097–12110.
- Thornton, E. B., J. MacMahan, and A. H. J. Sallenger (2007). Rip currents, mega-cusps, and eroding dunes. *Marine Geology* 240, pp. 151–167.
- Tiessen, M. C. H., N. Dodd, and R. Garnier (2011). Development of crescentic bars for a periodically perturbed initial bathymetry. *Journal of Geophysical Research* 116(F04016). DOI:10.1029/2011JF002069.

- Tissier, M. F. S., P. Bonneton, R. Almar, B. Castelle, N. Bonneton, and A. Nahon (2011). Field measurements and non-linear prediction of wave celerity in the surf zone. *European Journal of Mechanics - B/Fluids* 30(6), pp. 635–641.
- Tissier, M. S., P. Bonneton, H. Michallet, and B. G. Ruessink (2015). Infragravity-wave modulation of short-wave celerity in the surf zone. *Journal of Geophysical Research: Oceans*. DOI:10.1002/2015JC010708.
- Trizna, D. B. (2001). Errors in bathymetric retrievals using linear dispersion in 3-D FFT analysis of marine radar ocean wave imagery. *IEEE Transactions on Geoscience and Remote Sensing* 39, pp. 2465–2469.
- Valenzuela, G. (1978). Theories for the interaction of electromagnetic and oceanic waves: A review. *Boundary-Layer Meteorology* 13, pp. 61–85.
- Van de Lageweg, W. I., K. R. Bryan, G. Coco, and B. G. Ruessink (2013). Observations of shoreline-sandbar coupling on an embayed beach. *Marine Geology* 344, pp. 101–114.
- Van der Grinten, R. M. and B. G. Ruessink (2012). *Evaluatie van de kustversterking bij Noordwijk aan Zee*. Tech. rep. Departement Fysische Geografie, Universiteit Utrecht, p. 53.
- Van Dongeren, A., N. G. Plant, A. Cohen, D. Roelvink, M. C. Haller, and P. Catalán (2008). Beach Wizard: Nearshore bathymetry estimation through assimilation of model computations and remote observations. *Coastal Engineering* 55(12), pp. 1016–1027.
- Van Duin, M., N. Wiersma, D. Walstra, L. van Rijn, and M. Stive (2004). Nourishing the shoreface: observations and hindcasting of the Egmond case, The Netherlands. *Coastal Engineering* 51(8-9), pp. 813–837.
- Van Enckevort, I. M. J. and K. M. Wijnberg (1999). Intra-annual changes in bar plan shape in a triple bar system. In: *Proceedings of Coastal Sediments*, pp. 1094–1108.
- Van Enckevort, I. M. J. and B. G. Ruessink (2001). Effect of hydrodynamics and bathymetry on video estimates of nearshore sandbar position. *Journal of Geophysical Research* 106(C8), pp. 16969–16979.
- Van Enckevort, I. M. J. and B. G. Ruessink (2003a). Video observations of nearshore bar behaviour. Part 1: alongshore uniform variability. *Continental Shelf Research* 23(5), pp. 501–512.
- Van Enckevort, I. M. J. and B. G. Ruessink (2003b). Video observations of nearshore bar behaviour. Part 2: alongshore non-uniform variability. *Continental Shelf Research* 23(5), pp. 513–532.
- Van Enckevort, I. M. J., B. G. Ruessink, G. Coco, K. Suzuki, I. L. Turner, N. G. Plant, and R. A. Holman (2004). Observations of nearshore crescentic sandbars. *Journal of Geophysical Research: Oceans* 109(C6). DOI:10.1029/2003JC002214.
- Van Rijn, L. C. (2011). Coastal erosion and control. *Ocean and Coastal Management* 54(12), pp. 867–887.
- Van Rijn, L. C., D. J. R. Walstra, B. Grasmeyer, J. Sutherland, S. Pan, and J. P. Sierra (2003). The predictability of cross-shore bed evolution of sandy beaches at the time scale of storms and seasons using process-based Profile models. *Coastal Engineering* 47, pp. 295–327.
- Van Son, S. T. J., R. C. Lindenbergh, M. A. de Schipper, S. de Vries, and K. Duijnmayr (2010). Application Monitoring bathymetric changes at storm scale technical. *PositionIT*, pp. 59–65.
- Vermaas, T., E. Elias, A. Van der Spek, and R. Hoogland (2017). Time-dependent effects of nourishments on shoreface bar behaviour. In: *Proceedings of Coastal Dynamics 2017*, pp. 862–869.
- Vis-Star, N. C., H. E. De Swart, and D. Calvete (2008). Patch behaviour and predictability properties of modelled finite-amplitude sand ridges on the inner shelf. *Nonlinear Processes in Geophysics* 15.6, pp. 943–955.
- Wijnberg, K. M. (2002). Environmental controls on decadal morphologic behaviour of the Holland coast. *Marine Geology* 189(3-4), pp. 227–247.
- Wijnberg, K. M. and J. H. J. Terwindt (1995). Extracting decadal morphological behaviour from high-resolution, long-term bathymetric surveys along the Holland coast using eigenfunction analysis. *Marine Geology* 126, pp. 301–330.
- Wijnberg, K. M. and R. A. Holman (2007). Video-observations of shoreward propagating accretionary waves. *Proceedings of the River, Coastal and Estuarine Morphodynamics*, pp. 737–744.

- Williams, W. W. (1947). The Determination of Gradients on Enemy-Held Beaches. *The Geographical Journal* 109(1), pp. 76–90.
- Wilson, G. W., H. T. Özkan-Haller, R. A. Holman, M. C. Haller, D. A. Honegger, and C. C. Chickadel (2014). Surf zone bathymetry and circulation predictions via data assimilation of remote sensing observations. *Journal of Geophysical Research: Oceans* 119, pp. 1993–2016.
- Wong, P. P., I. J. Losada, J. P. Gattuso, J. Hinkel, A. Khattabi, K. L. McInnes, Y. Saito, and A. Sallenger (2014). Coastal systems and low-lying areas. In: *Climate Change 2014: Impacts, Adaptation and Vulnerability. Part A: Global and Sectoral Aspects Contribution of Working Group II to the Fifth Assessment Report of the Intergovernmental Panel on Climate Change*. Ed. by L. Field, C.B. Barros, V.R., Dokken, D.J., Mach, K.J., Mastrandrea, M.D., Bilir, T.E., Chatterjee, M., Ebi, K.L., Estrada, Y.O., Genova, R.C., Girma, B., Kissel, E.S., Levy, A.N., MacCracken, S., Mastrandrea, P.R., White. Cambridge, United Kingdom and New York: Cambridge University Press, pp. 361–409.
- Wright, L. D. and A. D. Short (1984). Morphodynamic variability of surf zones and beaches: a synthesis. *Marine Geology* 56, pp. 93–118.
- Yoo, J., H. M. Fritz, K. A. Haas, P. A. Work, and C. F. Barnes (2011). Depth inversion in the surf zone with inclusion of wave nonlinearity using video-derived celerity. *Journal of Waterway, Port, Coastal, Ocean Engineering* 137(2), pp. 95–106.
- Young, I. R., W. Rosenthal, and F. Ziemer (1985). A three-dimensional analysis of marine radar images for the determination of ocean wave directionality and surface currents. *Journal of Geophysical Research* 90, pp. 1049–1059.
- Yu, J. and D. N. Slinn (2003). Effects of wave-current interaction on rip currents. *Journal of Geophysical Research* 108(C3). DOI:10.1029/2001JC001105.

Dankwoord/Acknowledgements

Velen zijn belangrijk geweest tijdens mijn promotietraject en zonder hen was dit boekje er niet gekomen. Hieronder noem en bedank ik graag een aantal mensen in het bijzonder.

Gerben, het was ontzettend fijn om je als promotor te mogen hebben. Je kennis over kustprocessen onder water, boven water, op zowel kilometer- als centimeterschaal is indrukwekkend. Ik ben je erg dankbaar voor je uitgebreide feedback op elk artikel, presentatie of review, dit heeft me veel geleerd. De uurtjes in kamer 213 of 204 of al wandelend in Amelisweerd vond ik altijd motiverend en bovenal leuk; brainstormend welke analysemethode nou wel werkt als die kustlijn krom is, puzzelend hoe een vergelijking op te schrijven, maar ook pratend over toekomstplannen. Fijn dat hier tijd voor was! Bovenal waardeer ik enorm je geduld, vertrouwen en persoonlijke aandacht, om me te laten groeien als wetenschapper maar ook als persoon. Je bent een voorbeeld. En missen ga ik je zeker. Timothy, co-promotor en overbuurman, met jou kan ik het enthousiasme delen voor banken en andere features in Argusbeelden. Je las aandachtig mijn drafts, en had engelse-taaladviezen die ik altijd erg heb gewaardeerd! Daarnaast ben ik je erg dankbaar voor de rol die je op je nam om mij als BSc student bij het schrijven van mijn scriptie in te wijden in het kustonderzoek. Behalve het leren detecteren van banklijnen in Argus en programmeren in Matlab hield dit ook het bezoeken van de NCK-dagen in om daar kennis te maken met kustwetenschappers uit de rest van Nederland en om een frisbee over te gooien.

Steven, ons artikel was niet 1-2-3 gepubliceerd, daarom was je altijd positieve kijk op ons werk erg fijn. Jouw blik van grotere afstand zorgde voor een gestructureerd verhaal en je kon goed aangeven waar meer uitleg nodig was. Bruno, thank you for hosting me in Bordeaux. Your energy and very enthusiastic response on colourful graphs or text, in person or by email, have always been very motivating. I especially learned from you by the questions you asked, making me look at bars from a different perspective. Benjamin, EPOCzerocinquanteneuf, runCouplage.py, synthetic bathymetries without or with perturbations, stories about the best waves to surf; thank you for all your extensive explanations about the model or other stuff and making the stay a good stay. I hope to continue working with you in future, who knows where. Rob, Cesca, Huib, Dano en Stefan, I am grateful for your input, it is an honour having you in the committee. Special thanks to Rob for always wanting to hear what is new.

Nature Coast and Nemo colleagues Max, Lianne, Isaac, Corjan, Marinka, Emily, Simeon, Marjolein, Iris, Sebastian, Ewert, Lotte, Arjen, Vera, Alexander, Bas, Bas, Saulo, Matthieu, Sierd and Martijn I always enjoyed seeing you and discussing the Zandmotor. You learned me a lot about eddies, sediment sorting, grasses, fish, benthos, dunes and aeolian transport, minerals, saltwater intrusion and decision making. I am grateful that we had the Nature Coast meetings with the end-users regularly to keep in touch with the applied side of coastal research, special thanks to Anna, Matthieu, Sicco, Mark and Carola for their input.

Juul, Marjan and Inge, dank jullie wel voor de departementale ondersteuning de afgelopen vijf jaar. Marcel, Henk, Chris, Bas, Hans en Arjen, hartelijk bedankt voor de technische ondersteuning tijdens het MegaPEX veldwerk en voor de inwinning van de Argusbeelden. Dear colleagues of the Physical Geography department, thank you for the good time we shared in the coffee corner, at the Gutenberg or during the lunch walks. Especially I want to men-

tion Joost, Anouk, Timothy, Marion, Gerben, Anita, Daan, Renske, Winnie, Jasper, Nynke, Yvonne, Pam, Klaas, Laura, Christian, Sepehr, Maarten van der Vegt, Piet, Yoshi, Sebastian, Mijke, Wietse, Philip, Harm-Jan, Niko and Maarten Kleinhans for inspiring, sharing passions, bringing laughter and lightness, listening, going out for a run or iceskating and spending evenings in the ACU, Gys or one of Amsterdam's Japanese restaurants. It was always nice to have new faces around from abroad; Jaime, Bastien, Drude and Eleonora, thank you for coming to Utrecht and bringing something new to the coastal group. Joost, dat jij daar 4.5 jaar achter het scherm tegenover me zat was altijd motiverend en je vrolijkheid en enthousiasme aanstekelijk. En na een dag Matlab, schrijven of congrespresentaties begon het ook bij jou te kriebelen om te gaan rennen, wat we dan ook deden op de Uithof, of op het strand van Skallingen, Renesse, Camperduin en de Brouwersdam. Ik ben je ontzettend dankbaar voor je onvoorwaardelijke steun. De kamer-204 tijd is over nu maar wat heeft het een bijzondere vriendschap gebracht. Jij en Aafke zijn van harte welkom aan de andere kant van de grote plas. Wietse, ik ben je erg dankbaar dat je voor die paar herfstmaanden mijn kantoorgenoot was. Het maakte het beter. Anouk, die goede Utrecht-tijd, het was fijn om dagelijks even onze belevenissen en plannen uit te wisselen, zittende op de tafel in een van onze kantoortjes. Ik bewonder dat je gewoon naar La Rochelle bent verhuisd en ben erg benieuwd wat je volgende woonplaats wordt. Katixa, I enjoyed our lunches at the stairs, runs along the Garonne and the Bordeaux nights, happy I got to know you! Benoit, it was a pleasure to share the office with you, talk about dunes, grèves, and surfing with or without kite. I have very good memories of going to Lacanau, seeing the kites and testing the waves. Next time at the Sand Engine? Dimitris and Roel, I am grateful that I could co-supervise you while writing your theses, the discussions we had about cBathy and sandbars were very inspiring. Bart, it feels strange we never met, but I want you to know that Section 5.2.2 was partly inspired by your BSc thesis, thanks!

Els, het was altijd fijn om thuis te komen. We hebben wat afgepraat in ons soms erg koude keukentje. Dank je voor je interesse, de ruimte die je me biedt en je wijze inzichten. Het maakt me erg blij dat we op hetzelfde moment een grote stap zetten. Hieke, het is ontzettend fijn om ervaringen en gedachten met je te delen en daarnaast kan ik met jou dingen doen die anderen maar raar vinden. Bijzonder dat we nu naast goede vriendinnen ook nog even huisgenoten zijn. Nathalie, wat ben je een lief en loyaal persoon. Ik ben blij dat we samen gingen boren in Joppe en omstreken en we sindsdien bevriend zijn. Sterke, stoere Mirke, jij bent er altijd voor in om wat leuks te doen, van zwemmen tot naar het Hartlooper. Jedidja, dank je voor je warmte en hartelijkheid. En de band niet te vergeten, Robbert en Roland, onze repetities kijk ik elke week weer naar uit! Samen iets onder elkaar zetten wat goed klinkt is genieten en doet alle andere dingen even vergeten. Het zal wel lastig zijn zonder jullie, maar het biedt mogelijkheden tot een gig abroad ;) Tisja, leuk dat we in hetzelfde werkveld zijn beland en daar nu als vrienden dingen over kunnen delen. Marjolein, dank je voor je vrolijkheid. Milou, jij bent er en dat blijft, wat is dat bijzonder. Jan, met je oprechte interesse in (aardwetenschappelijk) onderzoek maak je het me makkelijk om te vertellen over ons vak, fijn zo'n neef. Francien, er is altijd zoveel te delen, onze band betekent veel voor me! Jaap, Bram en Margreet, dank jullie voor het geduld met jullie zus(je) en dat wat we met elkaar hebben. Jaap, we zijn nog steeds de groten. Bram, samen even uitzoomen en relaxen. En grote, kleine zus Margreet, ik bewonder je. Fijn dat je naast me staat vandaag. Elvin, Elis, Ruben en Eren, dank jullie voor het nieuwe en andere dat jullie brengen in de familie. Papa en mama, dank jullie voor jullie oneindige en onvoorwaardelijke steun en het hechte gezin dat we zijn. Jullie betekenen veel voor me. Jaime, gracias por la tranquilidad que traes, happy to be together, soon also geographically speaking.

Utrecht, May 2018

About the author

Jantien Rutten was born on the 21st of April 1989 in Delft, where she grew up and attended secondary school at Grotius College Delft. In 2008, she started her bachelors in Earth Sciences at Utrecht University. Jantien got intrigued by beaches, waves and remote sensing when she discovered how series of time-averaged images could be used to detect changes of the seabed over time. Within her bachelor thesis, she used such imagery to investigate whether patterns in the outer and inner sandbar at the Gold Coast (Australia) were related to each other. Within her masters in Physical Geography she gained more research experience by taking part in several short projects on morpho- and hydrodynamics in both riverine and tidal environments. Thereafter, she wrote her thesis on wave information derived from X-band radar images and went for a six-month research stay to Seattle and Corvallis (USA) to study how sandbars migrate, split and merge at the ocean-exposed Benson Beach (USA). The good experiences abroad, her natural curiosity and her eagerness to learn convinced her to continue in research and find a PhD position. In April 2013, Jantien started as PhD candidate within the Nature Coast project at Utrecht University. In 2017, she stayed for 2.5 months at Université de Bordeaux (France) to collaborate with the developers of the numerical model presented in Chapter 4 of this thesis.

Publications

Journal papers

- RUTTEN, J., B. DUBARBIER, T.D. PRICE, B.G. RUESSINK & B. CASTELLE. (under review), Simulating crescentic sandbar behaviour along a curved coast. *Journal of Geophysical Research: Earth Surface*.
- SPLINTER, K.D., M.V.G. GONZALEZ, J. OLTMAN-SHAY, J. RUTTEN & R.A. HOLMAN (2018), Observations and modelling of shoreline and multiple sandbar behaviour on a high-energy meso-tidal beach. *Continental Shelf Research* 159, 33-45.
- RUTTEN, J., B.G. RUESSINK & T.D. PRICE (2018), Observations on sandbar behaviour along a man-made curved coast. *Earth Surface Processes and Landforms* 43, 134-149.
- RUTTEN, J., S.M. DE JONG & B.G. RUESSINK (2017), Accuracy of nearshore bathymetry inverted from X-band radar and optical video data. *IEEE Transactions on Geoscience and Remote Sensing* 55, 2, 1106-1116.
- ARRIAGA, J.A., J. RUTTEN, F. RIBAS, A. FALQUÈS & B.G. RUESSINK (2017), Modeling the long-term diffusion and feeding capability of a mega-nourishment. *Coastal Engineering* 121, 1-13.
- DE SCHIPPER, M.A., S. DE VRIES, B.G. RUESSINK, R.C. DE ZEEUW, J. RUTTEN, C. VAN GELDERMAAS & M.J.F. STIVE (2016), Initial spreading of a mega feeder nourishment: Observations of the Sand Engine pilot project. *Coastal Engineering* 111, 23-38.

VAN DE LAGEWEG, W.I., W.M. VAN DIJK, A.W. BAAR, J. RUTTEN & M.G. KLEINHANS (2014), Bank pull or bar push: what drives scroll-bar formation in meandering rivers? *Geology* 42, 4, 319-322.

Conference abstracts and proceedings

RUTTEN, J., B. DUBARBIER, T.D. PRICE, B. CASTELLE & B.G. RUESSINK. (2017), Crescentic bar patterns along curved coasts: observations and modelling. Proceedings of the 8th International Conference on Coastal Dynamics, Helsingør, Denmark, 1832-1842 (oral).

RUTTEN, J., B. DUBARBIER, T.D. PRICE, B. CASTELLE & B.G. RUESSINK. (2017), Crescentic bar patterns along curved coasts in a bimodal wave climate. NCK days 2017 (oral).

RUTTEN, J., T.D. PRICE & B.G. RUESSINK (2016), Sandbar behaviour along a man-made curved coast. 12th Argus Workshop, Duck, USA (oral).

RUTTEN, J., T.D. PRICE & B.G. RUESSINK (2016), Sandbar behaviour along a man-made curved coast. NCK days 2016 (poster).

RUTTEN, J. & B.G. RUESSINK. (2015), Sandbar behaviour along the Sand Motor. NCK days 2015 (oral).

RUTTEN, J., T.D. PRICE & B.G. RUESSINK (2014), Monitoring morphological evolution in a large and dynamic coastal environment. AGU fall meeting, San Francisco, USA (poster).

DE SCHIPPER, M.A., S. DE VRIES, R.C. DE ZEEUW, J. RUTTEN, B.G. RUESSINK, S.G.J. AARNINKHOF & C. VAN GELDER-MAAS (2014), Morphological development of a mega-nourishment: first observations at the Sand Engine. Proceedings of the 34th International Conference on Coastal Engineering, 73, 1-6.

RUTTEN, J. & B.G. RUESSINK (2014), Comparison between Argus, X-band and traditional monitoring in a rapidly changing environment. 11th Argus Workshop, Delft, The Netherlands (oral).

RUTTEN, J., D. CHATZISTRATIS, M.T.F. TISSIER & B.G. RUESSINK (2014), cBathy in shallow water. 11th Argus Workshop, Delft, The Netherlands (oral).

RUTTEN, J. & B.G. RUESSINK. (2014), How to measure morphological evolution of a mega-nourishment? NCK days 2014 (poster).

RUTTEN, J., J.J.A. DONKER, M. VAN DER VEGT, P. HOEKSTRA. (2011), Wave dissipation over a mussel bed. NCK days 2011 (poster).

PRICE, T.D., J. RUTTEN & B.G. RUESSINK (2011). Coupled behaviour within a double sandbar system. *Journal of Coastal Research*, SI 64 (Proceedings of the 11th International Coastal Symposium), 125-129.

PRICE, T.D., J. RUTTEN & B.G. RUESSINK (2010). Coupled behaviour within a double sandbar system. NCK days 2010 (poster).